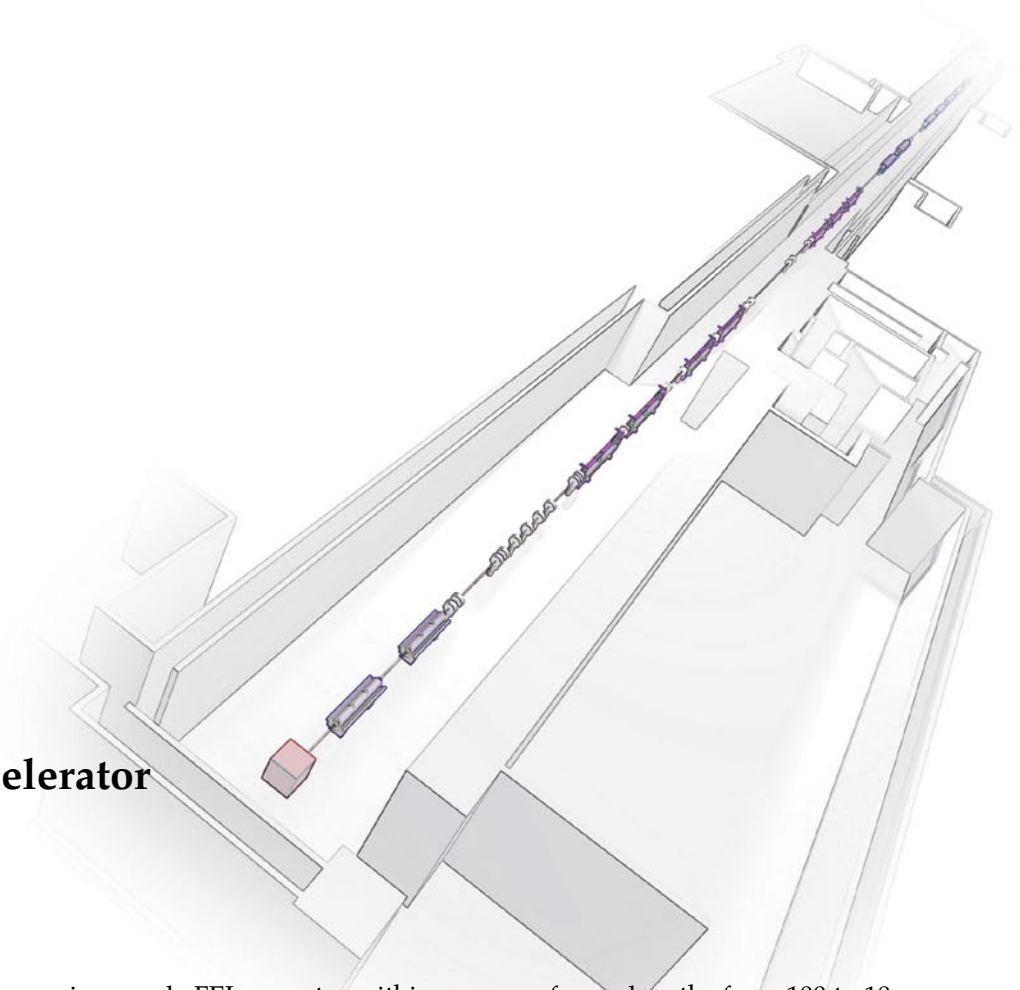

6 Accelerator

Synopsis

The FERMI harmonic cascade FEL operates within a range of wavelengths from 100 to 10 nm, covered by two distinct undulator chains at the fixed energy of ~1.2 GeV. Two electron beam scenarios have been developed: the medium length bunch (MLB) mode with a bunch length of ~ 700 fs and the long bunch (LB) mode with a bunch length of ~1.4 ps. The electron peak current is 800 or 500 A, respectively. The accelerator was designed with sufficient flexibility to accommodate such variations in bunch parameters. Other important electron beam parameters include the normalized slice electron beam emittance and the slice energy spread, which are about 1.5 μm rad and 150 keV, respectively. A challenging aspect was the demand to produce an electron beam with as uniform as possible peak current and energy distributions along the bunch. For this reason, a new parameter, the "flatness", defines the value of the quadratic component of energy variation along the bunch for which the increase in bandwidth of the x-ray signal due to this variation becomes equal to the Fourier transform limited bandwidth defined by the bunch length. Tracking results predict flatness of 0.8 MeV / ps^2 for the MLB mode and of 0.2 MeV / ps^2 for the LB mode.

Since the RF photocathode gun produces 0.8 nC and 1 nC for the two options distributed over bunch length of 9 ps and 11 ps respectively, the bunch has to be compressed by a total factor of about 9 before it enters the undulator. The acceleration and compression is done in the main S-band linac. The two bunch compressors (BCs) consist of symmetric magnetic chicanes, each 8.0 m long. They include trim quadrupoles for a fine tuning of the dispersion bump. The locations and compression

factor of the two chicanes were fixed in order to minimize the 6-dimensional emittance dilution of the electron bunch in presence of space charge forces and wake fields. The electron energy at BC1 is ~230 MeV in order to avoid space charge effects, while compressing the bunch early enough in the linac to reduce the effects of transverse wake fields. The energy of the second compressor is about 580 MeV, which balances the conflicting requirements of minimizing the transverse and longitudinal emittance dilution by coherent synchrotron radiation (CSR) and that of canceling the final correlated energy spread by means of the downstream longitudinal wake field. By using a weak chicane with a bending angle smaller than 0.07 rad per dipole and a large initial correlated energy spread within the range of 1.0% - 2.5%, the CSR effects can be reduced, but the chromatic aberrations make the tolerances on the magnets field quality tighter.

A short X-band RF structure is used prior to the first compressor in order to linearize the longitudinal phase space. It operates in the deceleration mode with a peak voltage of 18 MV; its contribution to the transverse and longitudinal wake fields is negligible compared to that of the main linac.

Since the whole beam delivery system acts like a huge amplifier of energy and density modulations, a laser heater is foreseen at 100 MeV just after the photoinjector to Landau damp the microbunching instability. The uncorrelated energy spread induced by this tool is able to suppress the modulation in the energy and density distributions at a scale small with respect to the bunch length; but, at the same time, the bunch compression brings the induced slice energy spread closer to the FEL threshold. It is important for the FEL process to provide slice energy spread not much larger than 150 keV (rms value). Simulations have been made which calculate the emittance dilution in the linac due to transverse wakefields and anomalous momentum dispersion, each of which arises with component misalignments. These simulations include realistic correction techniques and successfully demonstrate that the required level of transverse emittance preservation is achievable. Jitter studies implemented in full start-to-end simulations have been performed and a tolerance budget of the linac stability has been defined according to the FEL specifications.

The beam delivery system ends with a transfer line located between the end of the linac and the entrance of the FEL. This part includes the emittance diagnostic section, the electron beam switchyard for the two FELs, called “spreader”, and the matching sections. The design meets the constrains imposed by the existing and planned building boundaries, by the desire to utilize existing equipment and by the demands for various diagnostic instruments.

6.1 Introduction and Overview

This chapter describes the accelerator physics aspects, the engineering considerations and the choice of parameters that led to the design of the FERMI Free-Electron-Laser accelerator. The accelerator covers the region from the exit of the injector to the entrance of the first FEL undulator and its layout is described in paragraph 6.2. The tracking results of the electron beam dynamics from the photocathode to the linac end are shown in paragraph 6.3.

Paragraph 6.4 includes the technical aspects of the accelerating structures, modulators and low level RF (LLRF) system; it also contains some considerations about the upgrade needed to improve the linac stability.

When the intense electron bunch propagates down the accelerator, it is subject to various collective effects [1]. It was found that the longitudinal wakefields are responsible for the nonlinear variation of

the energy along the bunch. Paragraph 6.5 shows the geometric wakefields of the accelerating structures used in the tracking study. Paragraph 6.6 discusses the longitudinal dynamics during compression and acceleration. The emission of coherent synchrotron radiation (CSR) [3 and refs in 4] in the bunch compressors and the spreader is a relevant topic, since it may contribute to the emittance dilution. The microbunching instability is driven by a combination of longitudinal space charge (LSC) [5 and refs in 4], bunch compression and CSR; they continue to play a visible role in the formation of the microstructures on the electron bunch even at high energies and, if unaccounted for, can increase the energy spread in the electron beam beyond the tolerance for proper FEL operation. The design and the implementation of a laser heater [5] for energy Landau damping is presented, together with an estimate of its effect on the particles distribution. Nonlinear components in the RF waveform and in the time-of-flight characteristics of the bunch compressor are taken into account as they are often responsible for the appearance of high spikes in the peak current at the edges of the electron bunch [6]. The leading spike may induce resistive wall wakefields that modulate the energy of the electron bunch during its motion through the spreader and the undulator.

The transverse dynamics is studied in paragraph 6.7. Single particle dynamics considerations led to the evaluation of the magnets field quality needed in order to minimize aberrations. The collective effect of the beam break up (BBU) instability is also discussed. The impact of the transverse wakefields is enhanced by the trajectory distortion if the tolerance budget for field quality and accelerator alignment is not satisfied. Trajectory bumps were proposed to cancel the transverse-longitudinal position correlation created by the wakefields [2]. Finally, the transverse acceptance and tolerance budget required for a total emittance blow up smaller than 10% are listed.

The jitter studies of paragraph 6.8 focus mainly on the longitudinal dynamics, since the FEL process is more sensitive to the longitudinal than to the transverse planes. Both MLB and LB modes have been analyzed in time dependent, full start-to-end simulations that include errors within the specified tolerance budget. Jitter studies of the slice parameters have been also performed. Paragraph 6.9 describes the beam collimation to be located in the Spreader and the beam dump. It is followed by the last paragraph 6.10 which contains some general considerations about instrumentation, diagnostic and feedback, directing the reader to the specific chapter for more details of the hardware involved.

6.1.1 Overview of Design Specifications

The FERMI accelerator is schematically shown in Figure 6.1.1. It consists of four linacs L1 – L4, two bunch compressors (BC1 and BC2), a laser heater and a spreader. The latter switches the electron beam into one of the undulator lines (not shown). The laser heater is the first component of the accelerator. At its output the energy of the electron beam is ~100 MeV and the peak current is 60-70 A. At the end of acceleration the electron beam energy is approximately 1.2 GeV and the electron peak current is either 500 A or 800 A, depending on the bunch length needed for the FEL operating modes. The latter envisage two options for the electron bunch length: the medium length bunch (MLB) mode with a bunch length of the order of 700 fs and the long bunch (LB) mode with a bunch length of the order of 1.4 ps. The electron beam delivery system was designed with sufficient flexibility to accommodate both. Other important electron beam parameters include the normalized slice emittance and the slice energy spread, which are 1.5 μm rad and 150 keV respectively for both bunch lengths.

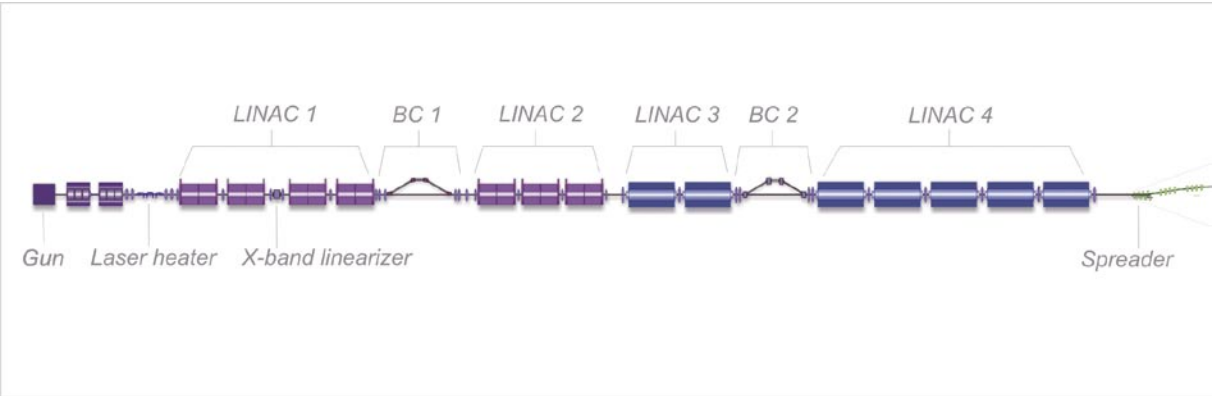

Figure 6.1.1:
A schematic of the FERMI accelerator.

The list of the beam specifications is shown in Table 6.1.1. A new parameter, the "flatness", is also quoted. It defines that value of the quadratic component of the average energy variation along the bunch for which the increase in bandwidth of the x-ray signal becomes equal to the Fourier transform limited bandwidth defined by the bunch length.

Table 6.1.1: Main electron beam specifications.

	MEDIUM	*LONG*	*Units*
Bunch Charge	0.80	1.00	nC
Bunch Length, FWHM	700	1400	fs
Peak Current	800	500	A
Slice Norm. Emittance	<1.5	<1.5	μm
Flatness, $\lvert d^2E/dt^2 \rvert$	<0.8	<0.2	MeV/ps^2

Table 6.1.2 lists the major machine parameters for the medium length and long bunches.

Table 6.1.2: Basic linac and compressors parameters.

Configuration		*MLB*	*LB*	*Units*
Charge		0.8	1	nC
Linac-1: voltage		47 x 4	47 x 4	MV
Linac-1: phase		54	62	deg
X-band: voltage		18	18	MV
X-band: phase		-90	-90	deg
Linac-2: voltage		47 x 3	47 x 3	MV
Linac-2: phase		70	72	deg
Linac-3: voltage		120 x 2	120 x 2	MV
Linac-3: phase		70	72	deg
Linac-4: voltage		120 x 5	120 x 5	MV
Linac-4: phase		109	105	deg
BC1	E	230	244	MeV
	R_{56}	-0.0280	-0.0280	m
	σ_δ	2.7	2.0	%
	C.F.	4.5	2.5	
BC2	E	584	602	MeV
	R_{56}	-0.0162	-0.0315	m
	σ_δ	1.1	1.2	%
	C.F.	2.5	3.5	

The compression factors are determined by the need to reduce the CSR instability and the CSR induced growth of the projected emittance. The energy of the first magnetic chicane (BC1) avoids a beam dynamics dominated by space charge forces, while that of the second (BC2) is limited by CSR that might arise with a high momentum compaction lattice

As for the linac, phases and voltages of the accelerating structures were chosen in order to achieve the desired compression and, at the same time, to manage the longitudinal wake for best cancellation of the final energy chirp.

The location of the different types of accelerating structures in the linac layout was mainly guided by the minimization of the transverse wake fields by putting the structures with the highest impedance at the linac end, where a shorter bunch is accelerated.

6.2 Accelerator Lattice and Components

Figure 6.2.1 shows the Twiss functions of the entire accelerator, together with a description of the locations of the major components. The parameters of each component are presented in the following sections.

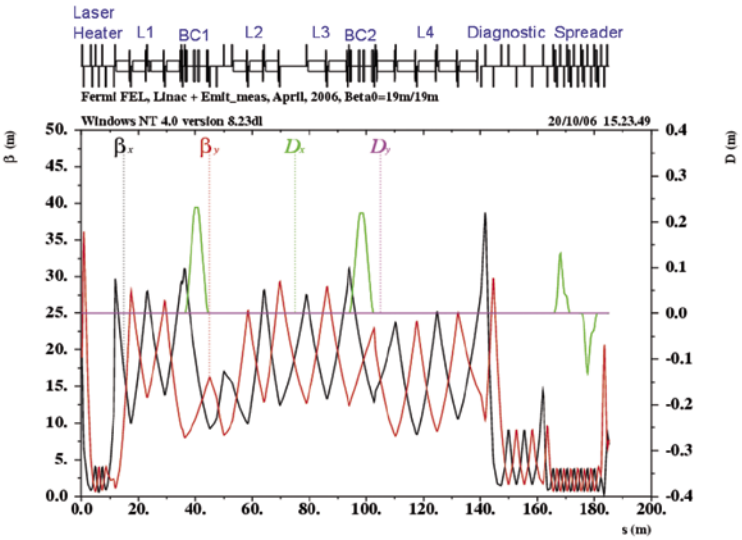

Figure 6.2.1:
Twiss functions of the accelerator.

6.2.1 Laser Heater

The plot of the Twiss functions in this area is shown in Figure 6.2.2. The lattice was designed to be flexible enough to accommodate variations in the input beta-functions in the range of 3 – 40 m.

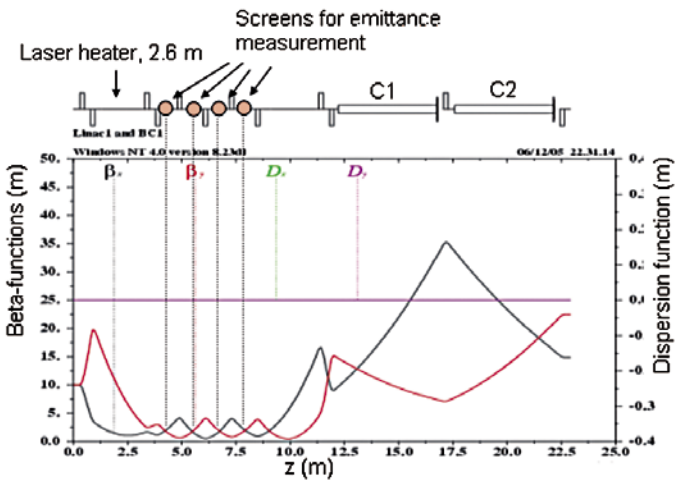

Figure 6.2.2:
Twiss functions of the laser heater and adjacent diagnostic section.

6.2.2 First Bunch Compressor

A schematic of the bunch compressor is shown in Figure 6.2.3. It consists of a chicane built from four rectangular bending magnets [7]. Because of its symmetry, this bunch compressor is a perfect achromat. Nevertheless, leakage of the dispersion function after the last bend may occur due to errors; for this reason, trim quadrupoles (shown in Figure 6.2.3 between the first and second bends and the third and fourth bends) are added for a fine tuning of the dispersion function.

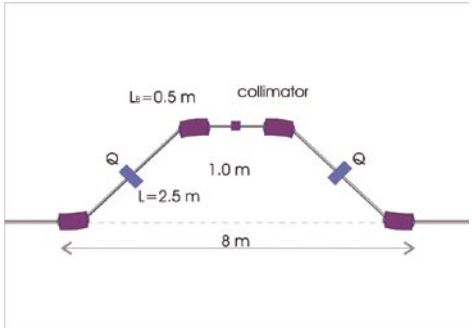

Figure 6.2.3:
A schematic of the bunch compressor.

It is important for the design of the bunch compressor to take CSR into account. Although transverse microbunching radiative fields affect the emittance directly, an indirect emittance excitation via longitudinal-to-transverse coupling:

$$\delta\varepsilon_x \approx H\left(\delta E / E\right)^2 \qquad 6.2.1$$

typically dominates. ΔE/E is the energy spread caused by CSR and H is the optical function defined in [8].

According to Eq. 6.2.1, the BC1 lattice was designed in such a way that the magnitude of H in the last bend of the chicane can be varied by up to a factor of four. This will give some flexibility to maneuver

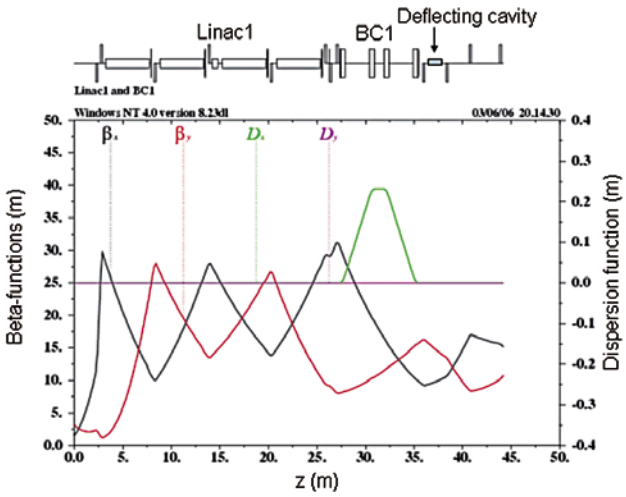

Figure 6.2.4:
Twiss functions of the first bunch compressor and adjacent L1.

between such tasks as containing the emittance excitation due to CSR, which benefits from a smaller H, and containing the energy spread growth due to the microbunching instability, which benefits from a larger H. Four quadrupole magnets after the chicane are used to match the Twiss functions into the downstream L2 (see, Figure 6.2.4). Between these magnets space has been reserved for a deflecting cavity to be used for emittance measurements and for a beam dump to be used during commissioning.

6.2.3 Second Bunch Compressor

The Twiss functions of this compressor are shown in Figure 6.2.5. The lattice of BC2 is exactly the same as that of BC1, shown in Figure 6.2.3, and designed so that the magnitude of H in the last bend of the chicane can vary by up to a factor of four. The physics considerations are also the same as those discussed for BC1.

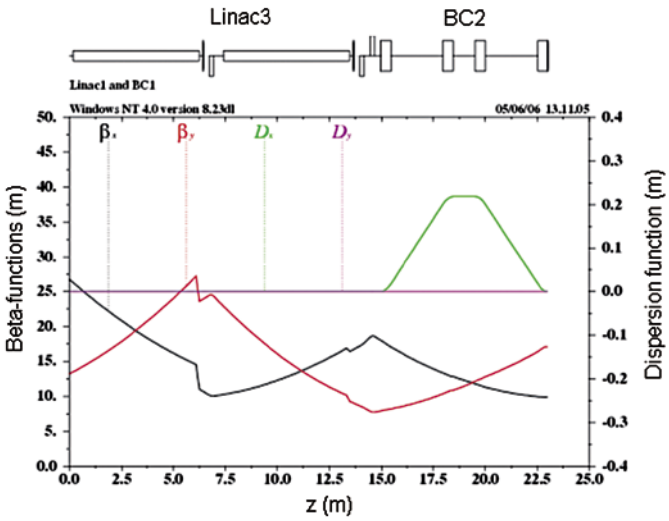

Figure 6.2.5:
Twiss functions of the first bunch compressor and adjacent L3.

6.2.4 Linac End Section and Spreader

6.2.4.1 Layout

A detailed description of the transfer line connecting the accelerator to the undulator chains may be found in [44]; this reference includes considerations on some technical aspects of the design.

A simplified schematic of the spreader is shown in Figure 6.2.6. One of the design goals is to minimize its length for two main reasons: the cost of the building housing the line and the fact that the position of the start of the experimental area is fixed and delimited by the existing building. For this reason, strong quadrupoles and short drifts are used. The bending angle of the spreader's bending magnets is also predetermined as a design requirement of the experimental area is to shift FEL-2 line by 1 m and FEL-1 line by 3 m from the linac line [45].

The spreader starts with two 3 degrees bending magnets of that deflect the electron beam away from the linac. Two more 3 degrees bending magnets with of opposite polarity turn the electron beam back into the straight line of FEL-2. Alternatively, the third magnet is switched off and the electron beam proceeds to the second pair of magnets that deflect electron beam back into the straight line of FEL-1 (see Figure 6.2.6).

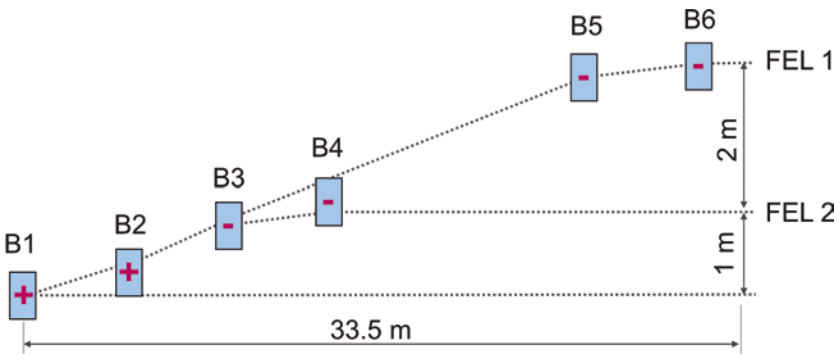

Figure 6.2.6:
A schematic of the spreader.

It is important that the spreader lattice preserves the electron beam emittance. This is done by two means: i) by using a lattice with small *H* function in the magnets; ii) by employing a scheme of emittance self-compensation. Besides four bending magnets, the lattice includes twelve quadrupoles that are arranged like a FODO lattice with $\pi/2$ betatron phase advance in x and y planes per unit cell. The latter is comprised of two quadrupoles and two drift lengths. Two cells are used between two adjacent bending magnets to produce $-I$ transfer matrix in each plane. This arrangement in the horizontal plane provides a basis for a compensation of the emittance excitation due to coherent synchrotron radiation (CSR) in the spreader's bending magnets.

6.2.4.2 Emittance Diagnostic Section

The emittance diagnostic section is located between the linac and the spreader and is designed for measuring the emittance using optical transition radiation from the screens that can be inserted into the electron beam path. Vertical and horizontal beam emittances will be derived from the measurements of the electron beam sizes at several locations with various betatron phase advances. Two variants of the lattice are proposed, corresponding to an invasive and a non-invasive modes of operation: i) a production lattice designed for normal operation during x-ray beam delivery and ii) a diagnostic lattice designed for emittance measurements when the photon beam is not delivered and the electron beam can be intercepted

In the latter case a periodic lattice is used with a betatron phase advancing from one screen to the next by approximately $\pi/4$ in both planes and with almost equal horizontal and vertical beta functions at all the screens' locations. A RF deflecting cavity is located upstream of the screens and is used for slice emittance measurements. A more detailed schematic of the part of the spreader leading to FEL-2 and the associated Twiss functions are shown in Figure 6.2.7.

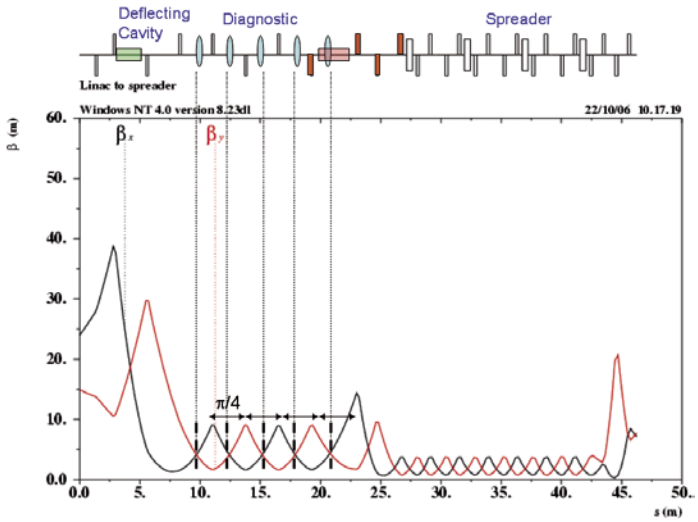

Figure 6.2.7:
Twiss functions of the transfer line for diagnostic purposes beginning from L4 and ending at the entrance of the FEL-2.

6.2.4.3 Production Lattice

The lattice configuration during photon beam delivery is shown in Figure 6.2.8. It is less favorable for emittance diagnostics because of the less periodic behaviour of the Twiss functions within the screen area and less regular advance of the betatron phases. In spite of this shortcoming, all the screens can still be used for quick beam characterization albeit less accurate than that of the dedicated line.

A distinctive feature of the production lattice is the presence of the two local peaks of the beta functions in the diagnostic section just upstream of the spreader. The lattice is tuned such as to have 3/2 π betatron phase advance between the local peaks of the beta functions where adjustable x and y collimators will be used. The energy collimator will be used near the peak of the dispersion function inside the spreader, as shown in Figure 6.2.9 for FEL-2.

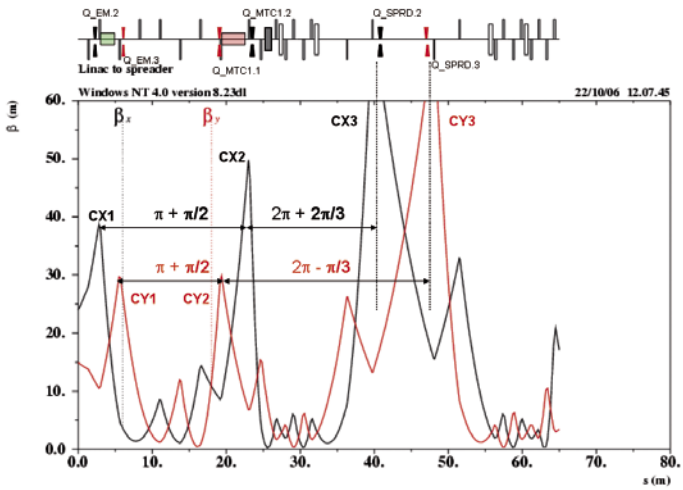

Figure 6.2.8:
Twiss functions of the transfer line in the configuration suitable FEL operation beginning from L4 and ending at the entrance of the FEL-1. The locations of the betatron collimators are shown.

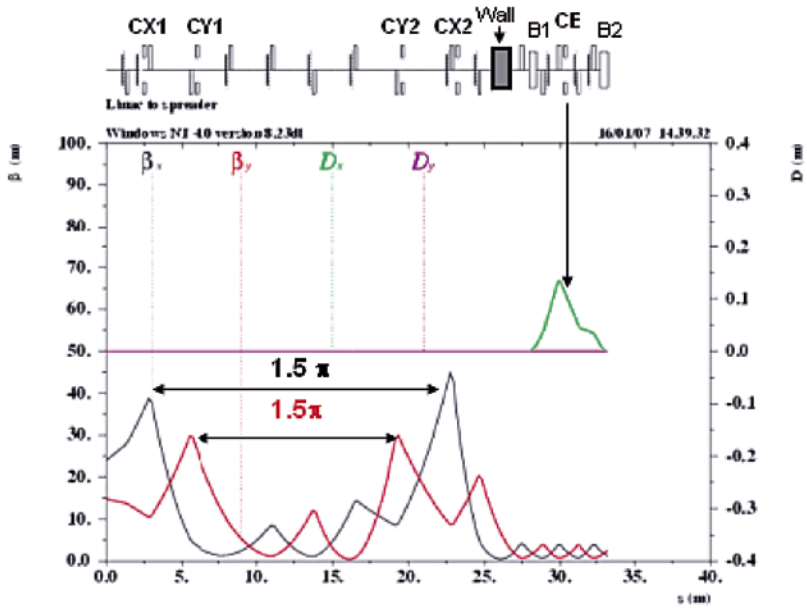

Figure 6.2.9:
Schematic and lattice functions of the FEL-2 production lattice from the end of the linac and through the first two bending magnets of the spreader. The top line indicates the location of the collimators.

Matching sections after the spreader are very similar for FEL-2 and FEL-1. Four matching quadrupoles provide enough flexibility to adjust the Twiss functions at the FEL input. A 5 m long drift is reserved after the last quadrupole and precision cavity BPMs will be placed on both sides of this drift. The electro-optical monitor for measuring the electron bunch arrival time will also be placed inside this drift.

6.2.4.4 Time-of-flight Adjustment

The two quadrupoles placed between each pair of dipoles are separated by a unit transfer matrix and located close to the positive and negative peaks of the dispersion function. Thus, one can simultaneously change their gradients and produce a dispersion bump localized between the quadrupoles. By controlling this bump one would be able to regulate the R_{56} of the spreader making it to be exactly zero or any other reasonable value. In fact, it is proposed to keep it slightly positive in some cases in order to disperse the electrons in the spikes of the peak current.

The time-of-flight parameter R_{56} of the spreader shown in Figure 6.2.8 can be adjusted within a relatively large range of values. In order to do this one needs to synchronously tune two quadrupoles, one of which is located near the peak of the dispersion function. With this arrangement the dispersion function gets a kick at the first quadrupole, oscillates between B2 and B3 magnets and gets a compensating kick at the second quadrupole.

Figure 6.2.10 shows the spreader part of FEL-2 when the strength of the Q2 and Q10 quadrupoles is lowered by 10% with the goal to increase R_{56} from 0.9 to 5.5 mm. Figure 6.2.10 shows that this adjustment causes some beating of the beta-functions at the end of the lattice that must be corrected in the matching lattice downstream. Tweaking the same quadrupoles in the opposite directions, i.*e.* reducing the gradient in one quadrupole and increasing in the another quadrupole by the same amount, allows a fine

adjustments of the dispersion function thus enabling the correction of any dispersion leak that might be caused by errors (magnetic or alignment) without affecting the beta-functions and R_{56}.

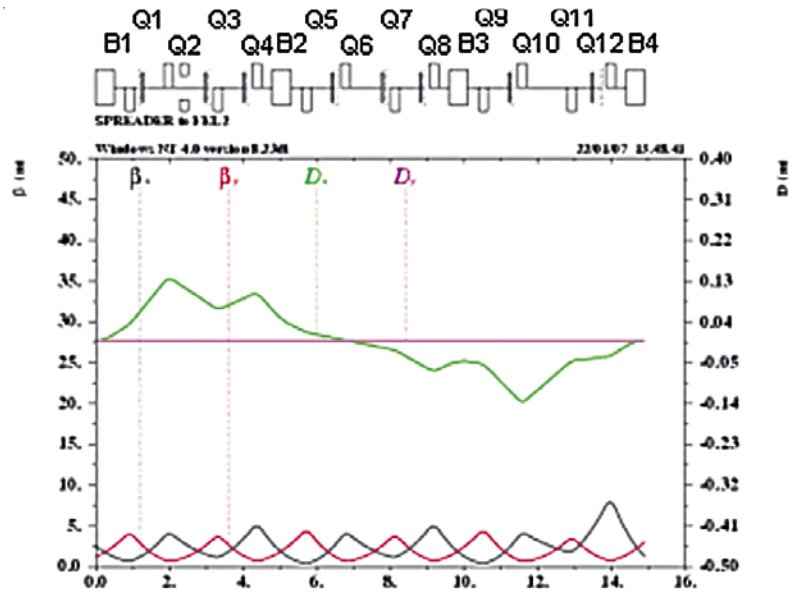

Figure 6.2.10:
Schematic and lattice functions for a spreader part leading to FEL-2. A reduction of the Q2 and Q10 quadrupole gradients by 10% changed R56 from 0.9 mm to 5.5 mm.

6.2.4.5 Technical Aspects

This paragraph shows the solutions adopted for the hardware of two difficult areas of the spreader in terms of high congestion of components occupancy. Figure 6.2.11 shows the layout of the area downstream of the B3 bending magnet where two beam lines split.

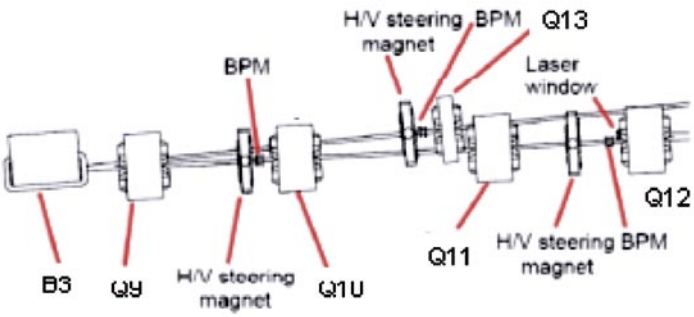

Figure 6.2.11:
The layout of the area downstream of the B3 bending magnet where two beam lines split.

The electron beam following the FEL-2 line goes through the centers of the Q9, Q10, Q11 and Q12 quadrupoles, while the FEL-1 beam goes through the center of the Q13 quadrupole and in a chamber that penetrates the iron of Q10. In Q9 the beam trajectory is off-axis (see, Figure 6.2.12) which means that this quadrupole must accommodate the vacuum chamber for both beams. The location of this quadrupole is appropriately chosen; its conceptual design is shown in Figure 6.2.12.

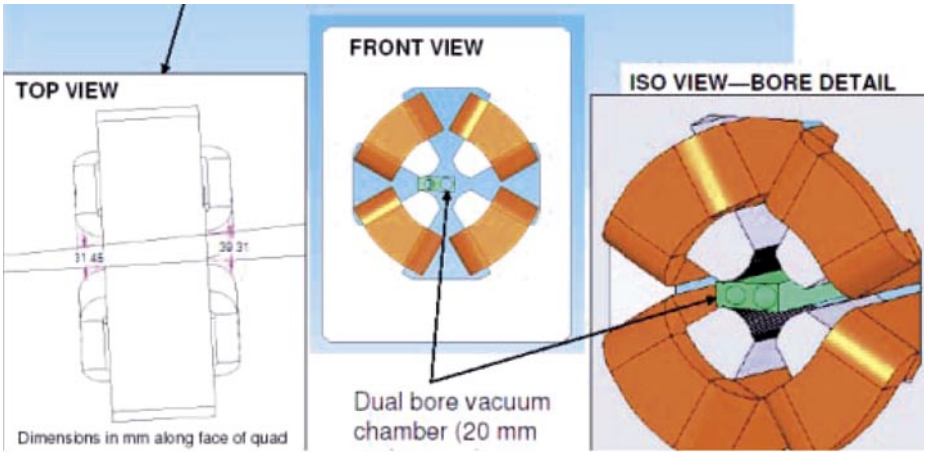

Figure 6.2.12:
Top, front and isometric view of the quadrupole Q9 showing also electron beam trajectories and a sketch of the vacuum chambers for the central and periphery beams.

Figure 6.2.13 shows the seed laser port and the surrounding apparatus. The location for this port just upstream of the last bending magnet B4 is the closest to FEL-2 and it is still more than 11 m away from it.

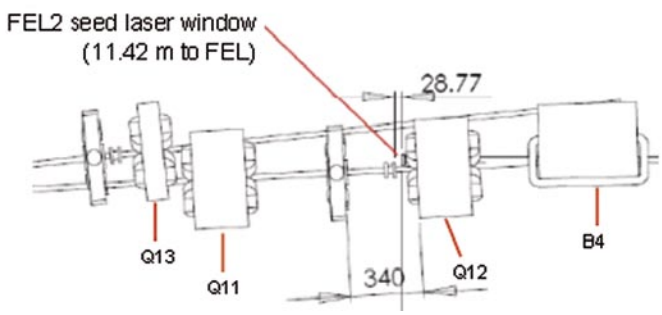

Figure 6.2.13:
Top view of the seed laser port for FEL-2 and surrounding apparatus.

Figure 6.2.14 shows the fine details of the laser port, such as flange, window sizes and window separation from the electron beam axis. Like for the quadrupole Q9, the quadrupole Q12 accommodates the vacuum chamber that allows two beams, the electron beam and the laser beam, both heading towards the FEL-2.

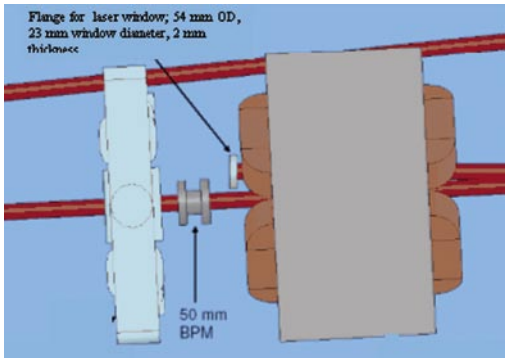

Figure 6.2.14:
Details of the seed laser port.

The design of the seed laser port for FEL-1 is exactly the same as the one just described for FEL-2. This port is located upstream of the bending magnet B6 and the quadrupole Q18 (not in figures).

6.3 Tracking Study

This paragraph shows the results of particle tracking for the nominal set of operation of the FERMI Linac. Simulations with several codes [30, 40] show rather an accurate agreement in their results. They confirm also the original estimate that CSR and LSC wake potentials contribute only weakly to the formation of the electron bunch on a scale large compared to the bunch length.

6.3.1 Medium Length Bunch Mode

The electron beam parameters of the medium length bunch mode (MLB) are given in the Table 6.3.1.

Table 6.3.1: Electron beam parameters for the MLB mode.

Bunch charge	0.8	nC
Beam energy	1.140	GeV
Peak current (beam core)	800	A
Bunch duration (full width, beam core)	700	fs
Slice energy spread (rms, beam core)	150	keV
Slice emittance (rms, beam core)	1.5	μm
Laser heater (energy spread rms)	12	keV
Compression factor in BC1 / BC2	4.5 / 2.5	
Flatness	0.8	MeV/ps^2

Figure 6.3.1 shows the electron distribution in the longitudinal phase space and a histogram of the peak current. Figure 6.3.2 shows the plot of the slice emittance and slice energy spread at the end of the accelerator for the MLB.

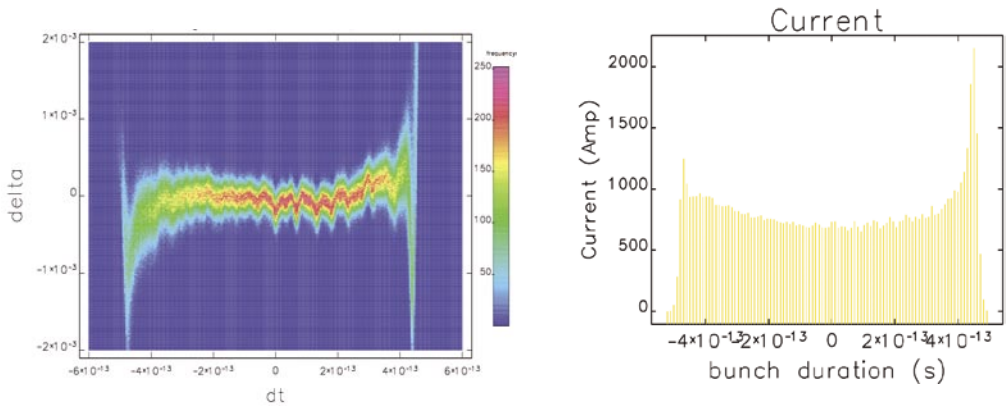

Figure 6.3.1:
MLB mode: density plot showing the distribution of the electron relative energy spread versus time and the histogram of the peak current.

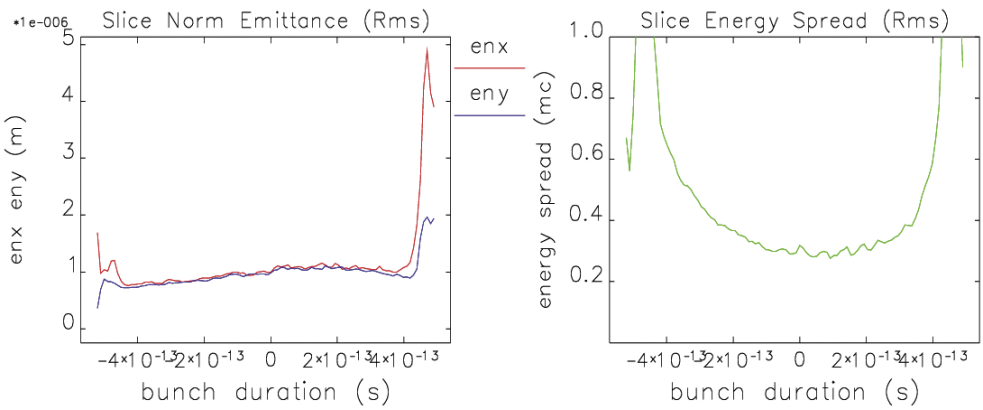

Figure 6.3.2:
MLB mode: slice normalized emittance (left) and slice energy spread (right) at the end of the accelerator.

According to this plot, there is no growth of slice emittance during acceleration and compression. The variation of the slice emittance seen in Figure 6.3.2 is due to the ramped peak current in the injector. We note that the smallest emittance is at the head of the electron bunch. This may have a useful implication because head-electrons radiate in the final stage of the harmonic cascade FEL with the most demanding specification for the electron beam emittance.

6.3.2 Long Bunch Mode

The electron beam parameters for the long bunch mode are given in the Table 6.3.2.

Table 6.3.2: Electron beam parameters for the LB mode.

Bunch charge	1.0	nC
Beam energy	1.170	GeV
Peak current (beam core)	500	A
Bunch duration (full width, beam core)	1400	fs
Slice energy spread (rms, beam core)	150	keV
Slice emittance (rms, beam core)	1.5	μm
Laser heater (energy spread rms)	15	keV
Compression factor in BC1 / BC2	2.5 / 3.5	
Flatness	0.2	MeV/ps^2

Figure 6.3.3 shows the electron distribution in the longitudinal phase space and a histogram of the peak current obtained with Elegant for the LB. Figure 6.3.4 shows the plot of the slice emittance and slice energy spread at the end of the accelerator.

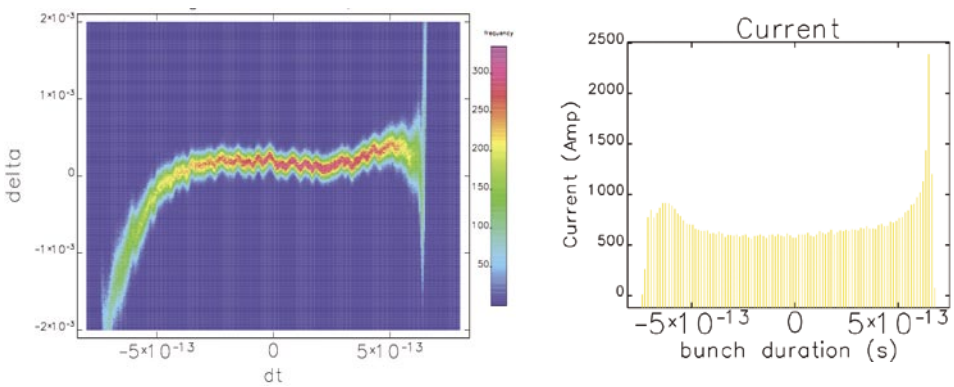

Figure 6.3.3:
LB mode: density plot showing the distribution of the electron relative energy spread versus time and the histogram of the peak current.

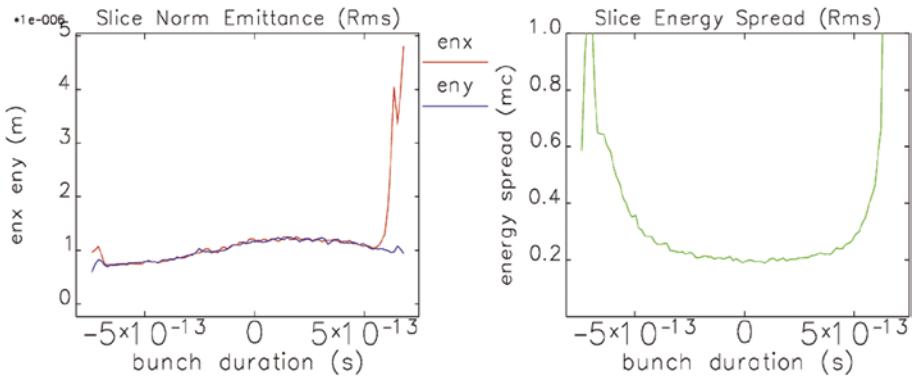

Figure 6.3.4:
LB mode: slice normalized emittance (left) and slice energy spread (right) at the end of the accelerator.

6.4 The Linear Accelerator

In order to raise the operating energy to 1.2 GeV, necessary to satisfy the specifications of the FERMI project, seven additional sections will be installed in addition to the present linac. These sections were obtained from CERN after the decommissioning of the LEP Injector Linac (LIL). These sections will also allow to maintain an adequate margin over the maximum operating energy, providing a more flexible and reliable operation, which is particularly important in a user facility such as FERMI. In addition to the energy upgrade, the linac will also be modified in several other ways:

- the installation of a new high brilliance source, made of a last generation photoinjector of the SLAC-UCLA-BNL type. This gun, operating like the rest of the linac at 2998 MHz, is described in mode details in Chapter 5 of this document;
- a laser heater section;
- the installation of an accelerating section in 4th harmonic (in the X-band region, 11.4 GHz) to linearize the longitudinal compression;
- the installation of two bunch compressors based upon magnetic chicanes, which allow to increase the peak power of the beam and to simultaneously reduce the pulse length;
- the performance improvement of the existing RF plants, and the optimization of such systems in terms of amplitude and phase stability, using advanced digital feedback techniques;
- the improvement of the beam diagnostic system along the entire linac, including the installation of new devices such as deflecting cavities to measure bunch length.

6.4.1 Existing Linac and Future Upgrade

The present Linac is composed of eight high power RF plants, each of them equipped with a 45 MW S-band klystron modulator Thales TH 2132A; two 3.2 m long accelerating sections (SØA, SØB), powered from the same klystron; seven 6.1 m long accelerating structures (S1 to S7), each one equipped with an RF compression system (SLED) and powered with its own 45 MW klystron. All these components are housed in two adjacent areas: the klystron gallery, at ground level, where all the RF generators are located and the accelerator tunnel (112 m long), situated 5 m below the ground level to ease the specifications of radiation safety.

The two areas are connected by means of a suitable number of apertures, placed near each RF plant, that allow the passage of waveguides, signal cables, piping, etc. In order to accommodate the energy upgrade and the conversion to injection into the FEL, the klystron building and injector tunnels will be expanded by about 85 m. The new building will house the new front end up to the first bunch compressor (see, Figure 6.4.1).

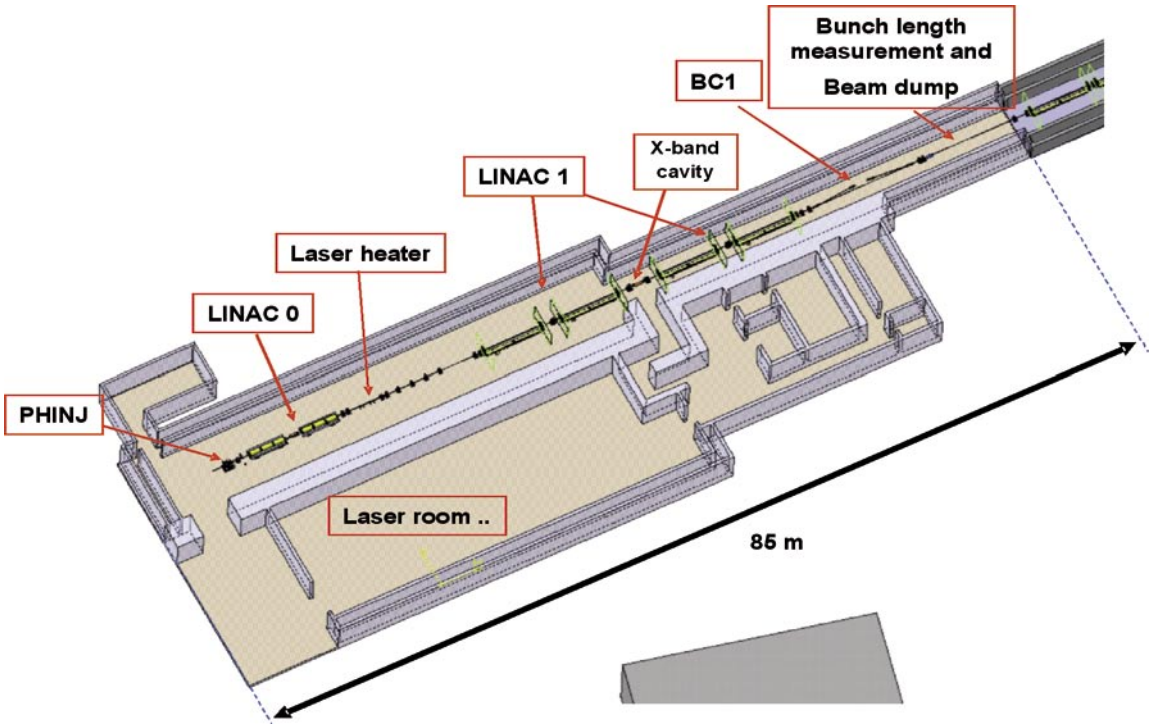

Figure 6.4.1:
The new machine Front-end.

6.4.2 Accelerating Structures

The accelerator uses three types of sections [10]. The S0A and S0B sections follow the electron gun and are used for the initial acceleration and the emittance compensation scheme. A detailed description of the injector and its parameters can be found in Chapter 5. Seven CERN-type sections (C1-C7) are divided

between L1 (four sections) and L2 (three sections) and are used upstream and downstream BC1. S0A, S0B and the CERN sections are traveling wave (TW) structures operating in the 2/3 π mode and coupled on axis. Seven ELETTRA-sections (S1-S7) make up L3 (two sections) and L4 (five sections) and are used upstream and downstream of BC2. They are backward traveling wave (BTW) structures operating in the 3/4 π mode and magnetically coupled. The inner geometries of the accelerating structures are shown schematically in Figure 6.4.2.

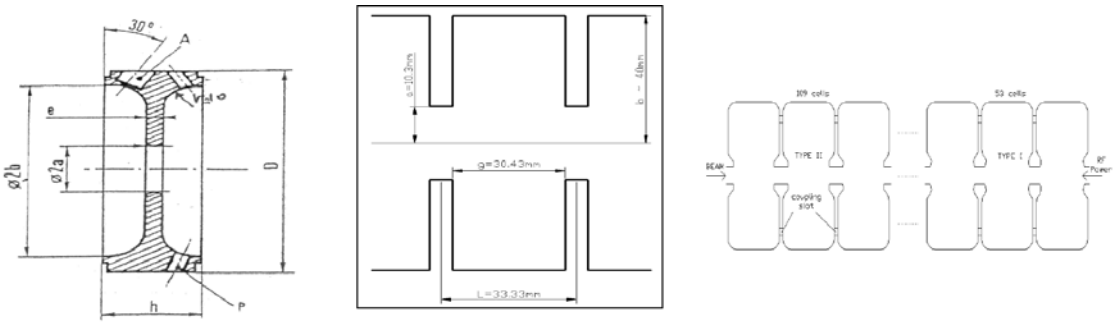

Figure 6.4.2:
FERMI accelerating structures. a) S0A-S0B geometry. b) C-type geometry (CERN). c) S-type geometry.

The first two geometries, shown in Figure 4a and 4b, are SLAC-type sections configured in traveling forward wave (TFW) mode with on-axis coupling and operated to a relatively modest gradient of 18 MV/m. The geometry shown in Figure 4c corresponds to a nose-cone type section with magnetic coupling; they operate in Backward Traveling Wave mode (BTW) and at high gradient (up to 25 MV/m). Unlike the previous two types, these have an iris radius of only 5 mm. The S-sections are supplied by an RF pulse compression system of the Sled type and by a TH 2132° klystron. The same type of klystron supplies two structures of the others.

Table 6.3.1 summarizes the main operational parameters of each of the three section types. An operating margin of up to 15% is available on top of the nominal energy gain.

Table 6.4.1: Linac energy budget.

Linac energy budget					
Type of structure	**Quantity**	**ΔE (MeV)**	**Maximum energy gain on crest (MeV)**	**Operating margin (%)**	**Operating energy gain on crest (MeV)**
Gun	1	5	5		5
S0A-S0B	2	50	100	10	90
C1-C7	7	55	385	15	329
S1-S7	7	140	980	14	840
X-band	1	-20	-20	0	-20
With X-band		**Total**	**1450**		**1244**
Without X-band		**Total**	**1414**		**1264**
FERMI energy 1200 MeV					

Figure 6.4.3 shows the new FERMI layout including the necessary building expansion, the planned distribution of the various section types in the new linac and the relative RF plants. For comparison, the existing buildings are shown below this drawing.

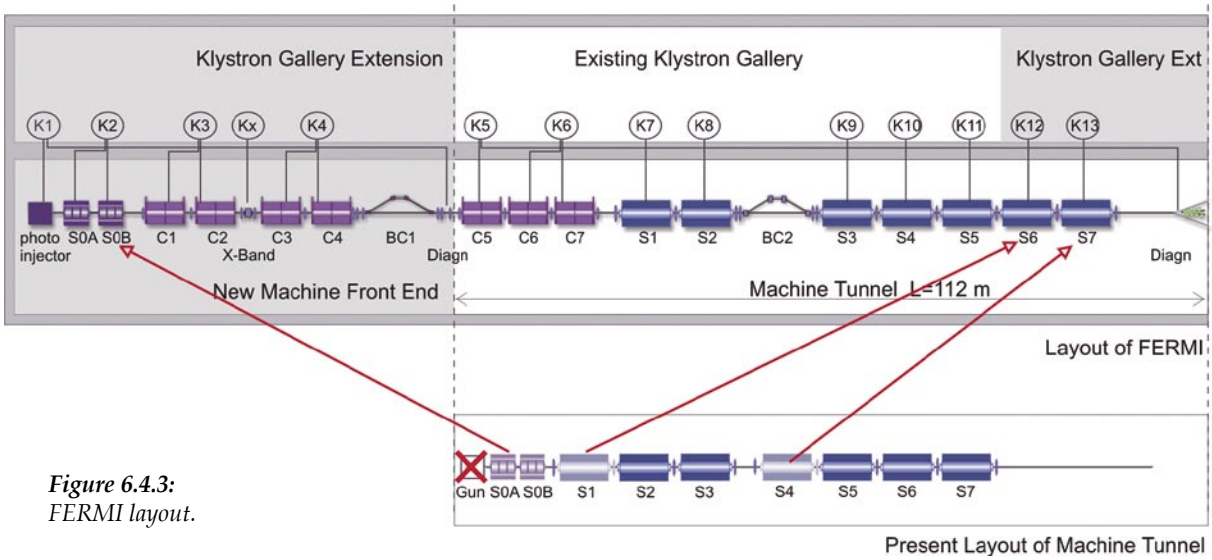

Figure 6.4.3:
FERMI layout.

The building expansion for the new front end is visible in the front of the existing structure. The figure also shows the RF systems and sections that will be relocated: S0A and S0B will be installed right after the photoinjector; S1 and S4 will be moved to the high energy end of the linac. A length of 10.5 m is kept available downstream of the S2 accelerating section. The proposed layout would leave the position of S2-S7 accelerating sections unchanged, thus reducing the impact of the machine upgrade.

6.4.3 HV Modulators

The present RF system is based on eight high power modulators, capable of 102 MW peak power and operating at 10 Hz, with their own klystrons (Thales TH 2132A, 3 GHz, 45 MW peak power, 4.5 μsec pulse width). The configuration adopted for each power station is based on an 18-cell PFN (Guillemin type E Pulse Forming Network), resonant charged with a constant current HV power supply (FUG-HCK 6750M-30000) and discharged with a double gap thyratron (EEV CX 1536X). The use of a coupled inductance PFN optimizes the rectangular pulse shape at the output compared to a conventional L-C network with the same number of elements.

The need to supply seven supplementary accelerating sections C1-C7 and the new Photocathode RF Gun will bring the total number of FERMI RF systems from eight to thirteen (MDK1-MDK13); the two deflecting structures that will be used for diagnostic purposes will keep the RF power from MDK1 and MDK6 respectively. Only the section S1-S7 will be fed through the existing SLED system.

In order to evaluate the energy gain of the linac, the plan is to operate each plant with a 10-15% margin on the maximum available klystron power, with an RF pulse width less than 3.5 μsec. Even if in the initial phase the system will be operated at 10 Hz, the upgrade of all system is planned to include the capability of operating at 50 Hz at a later phase. Particular care will be given to the stability of each station in terms of amplitude and phase of the fields with each section. This results in the very demanding tolerances required on the RF sections by the FERMI specifications. This challenging task starts from the optimization of the performance of the modulators. It is therefore planning to design and build new modulators for all of the stations in the system and to compare two prototypes: one based upon conventional technology, thyratron and an extremely low ripple PFN, in combination with a HV pulse transformer. A second based on a hybrid technology combining a solid state switch (an inductive adder) with a HV pulse transformer. Test both PFN and solid state allows the evaluation of performance, cost and risk. This R&D plan is intended to verify system performance especially in terms of stability and reliability, extremely important for a user facility like FERMI. This will lead the final design for the upgrade of the whole system.

6.4.3.1 Modulators Upgrade Plans

The klystron pulse specifications for the FERMI project are given in Table 6.4.2.

Table 6.4.2: Klystron modulator pulse specifications.

Parameter	*Value*	*Units*
Klystron	TH2132	Thales
Micro Perveance	1.9 to 2.1	$\mu A/V^{3/2}$
Peak Cathode Voltage	314	kV
Peak Cathode Current	350	A
Pulse Width	4.5	μs
Pulse Repetition Frequency	10-50	Hz
Rise/Fall Time	<2	μs

The present systems will meet all of the above specifications with the exception of the pulse repetition frequency. A prototype modulator based on the same technology, with an additional improvement on the pulse flatness (≤ 0.1%) and capable of operating at 50 Hz is being assembled. It will be installed and tested on the photoinjector. At the same time, a solid state design is proposed which we expect should result in reduced capital cost, improved efficiency, reliability and maintainability. The solid state design should also eliminate most single point failures of the modulator by employing redundancy. A simplified schematic of the proposed modulator is shown in Figure 6.4.4.

The proposed solid state modulator is an inductive adder, similar to those proposed by SLAC for the NLC and operating at SLAC for ORION, and for the SPEAR III injection kickers. The design in Figure 6.4.4 uses a minimum of six steel cores, each driven by two 6.5 kV, 800 A IGBT switches. In this design the adder circuit would drive the existing ELETTRA pulse transformer in the existing high voltage tank for the klystron. The modulator would easily fit in the present electronics enclosures.

The operation of the modulator is as follows. Each core is driven by two parallel IGBT drivers. The IGBTs switch 4 kV through a single turn primary. A single turn is passed through the aperture of each of the cores, inductively adding the primary voltages in series. The output pulse is then feed to the primary of the existing pulse transformer to drive the klystron cathode. Pulse shaping will be required because of a resonant condition caused by the modulator stack leakage inductance and primary to secondary capacitance, the leakage inductance and winding capacitance of the pulse transformer, and the klystron capacitance. This will cause an overshoot and oscillations on the flat top if all the IGBTs are quickly switched on at the same time. A solution is to slow down the rise time from the inductive adder. This is best accomplished by delaying turn on of some of the cells, as has been demonstrated with the 8-pack modulator at SLAC. Further shaping of the output pulse is required because of voltage droop during the pulse flat top caused by a finite capacitance, and transformer magnetizing inductance. The droop can be corrected by a bouncer circuit composed of an SCR switch and a resonant RC circuit where a sinusoidal voltage is subtracted from the main output pulse. The modulator parameters for this circuit are given in Table 6.4.3.

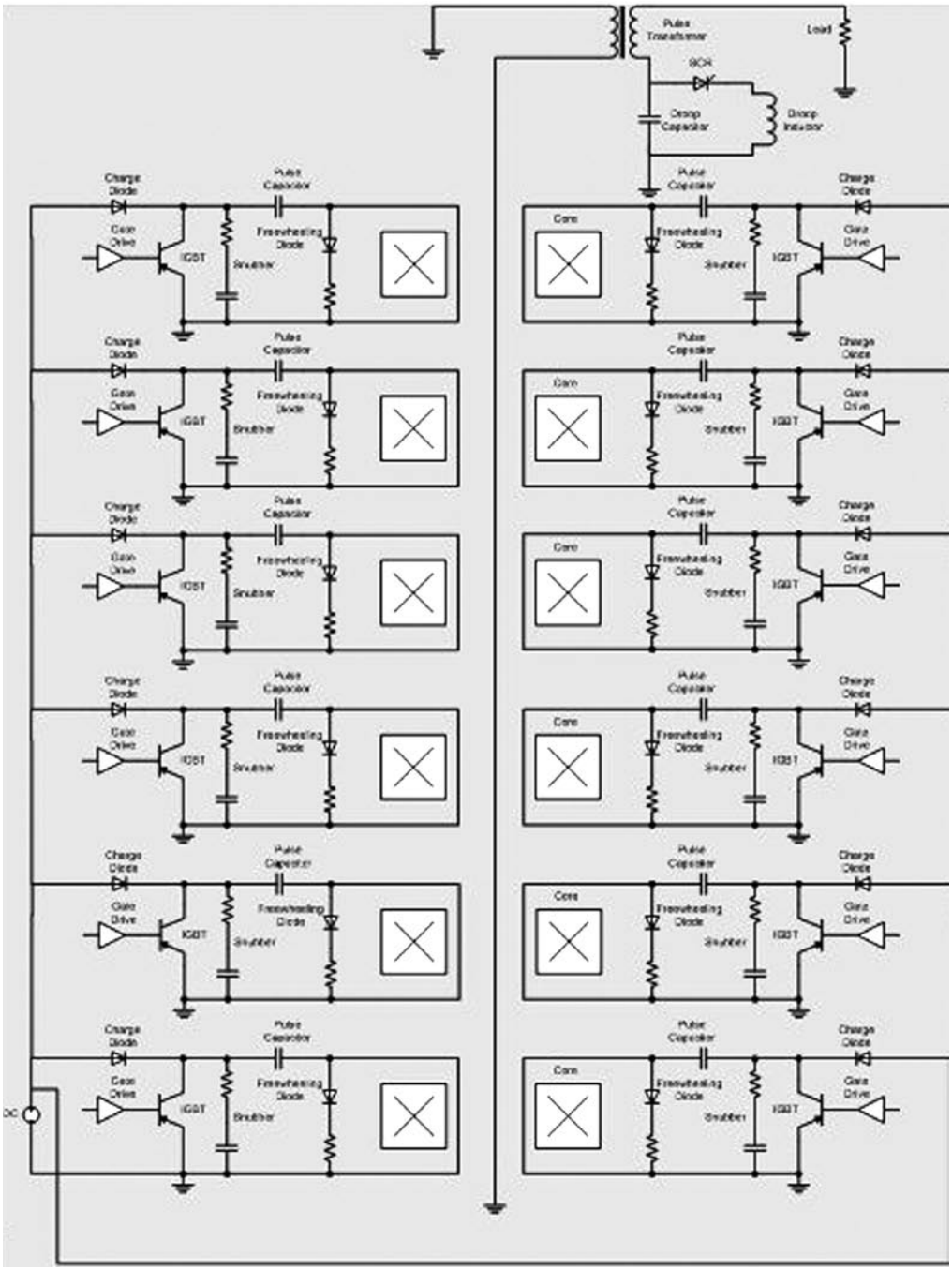

Figure 6.4.4:
Simplified schematic of a proposed solid state klystron modulator.

Table 6.4.3: List of modulator parameters.

Parameter	*Value*	*Units*
Number of Modulators	15	
Maximum Output Voltage	335	kV
Maximum Output Current	425	A
Maximum Repetition Frequency	60	Hz
Maximum Pulse Width	4.5	μs
Minimum Pulse Width	<100	ns
Rise Time	<2	μs
Fall Time	<1	μs
Pulse Flatness	<±1	%
Minimum # of Cells	6	
Minimum # of IGBTs	8	
Maximum IGBT Voltage	4000	V
Maximum IGBT Current	3000	A
Timing Jitter (rms)	<50	ns
Primary Power Supply	10	kW

6.4.4 LLRF System

The specifications of the RF control and timing systems are extremely demanding and require adopting state of the art technologies. One additional complication is the use of the X-band cavity, which is likely to be at an integer harmonic of the USA S-band frequency (2856 MHz) and therefore not an exact multiple of the existing linac operating at the European S-band frequency (2998 MHz). Local phase locked loops are planned to ensure the stability of each station.

The conceptual design of the LLRF system is made of three major components: the RF reference distribution system, the RF controller hardware, firmware, software and the interface with the timing and synchronization system. Each of these three components has been developed to a level of details sufficient to provide a reference design.

6.4.4.1 RF Reference Distribution System

This system was chosen to operate at 491 MHz, which is the frequency distributed throughout FERMI. It will be used locally to develop all the intermediate frequencies and in combination with local oscillators. This choice eliminates asynchronous events, since the same RF reference is used for the creation of all frequencies and phases.

The RF controller will make use of an FPGA-based digital processor [11] which takes advantage of the high dynamic range available in modern ADCs and DACs by down-converting the S and X bands to 48.2 and 47.6 MHz respectively. The RF and timing system distributes an RF reference signal at 491.64 MHz to all the RF stations. The digital controllers then process this frequency and synthesize the IF locally. The resulting IF is then used to lock each station to a phase reference provided by the synchronization system. This provides frequency references across the facility and eliminates asynchronous events.

Coherence between S and X bands is established by their common subharmonic of 15.779 MHz, which generates the S-band frequency when multiplied by 190, and the X-band driver when multiplied by 724. The reference signal of 491.64 MHz is 8 x 74/19 of the 15.779 MHz subharmonic. It is divided by 8 to get a 61.45 MHz digital clock for the ADC, DAC, and FPGA. A combination of DDS techniques and frequency multiplier chains are used to generate the S band (multiply by 6 + 87/111/8) and X band outputs (multiply by 24 - 2/3 - 86/111/8). Each station will be individually controlled by a single FPGA system that works off the 491 MHz reference frequency and the laser distributed timing pulses, as shown in Figure 6.4.5. In this approach the most critical components are the dividers and amplifier, as they can add noise to the system. These components are part of the proposed R&D plan for the RF controller upgrades.

6.4.4.2 Single Station Controllers

Each station requires a dedicated controller to ensure that the cavity fields are indeed synchronized to each individual bunch to the specified level of amplitude and phase. A block diagram of the system is shown in Figure 6.4.5. To accomplish this, each section will have a dedicated temperature stable reference, which will be used to calibrate each read-back point in between pulses. This will reset all errors in real time and will minimize the effects of slow drifts.

A Field Programmable Gate Array (FPGA) based digital controller will then take the reference phase provided by the laser distribution system and lock to it the local RF phase. After down conversion to the IF, the signals are digitized by 14 bit ADCs and all signal processing is then implemented in the FPGA. The firmware that programs the FPGA is the heart of the system and performs a multitude of tasks, from the actual feedback control, (although it is unlikely to have a closed feedback loop with such a short pulse due to the internal delay of the system), to adaptive feed forward compensation, to interlocks and protection. The firmware also contains the interface with local networks and the code to interact with the control system.

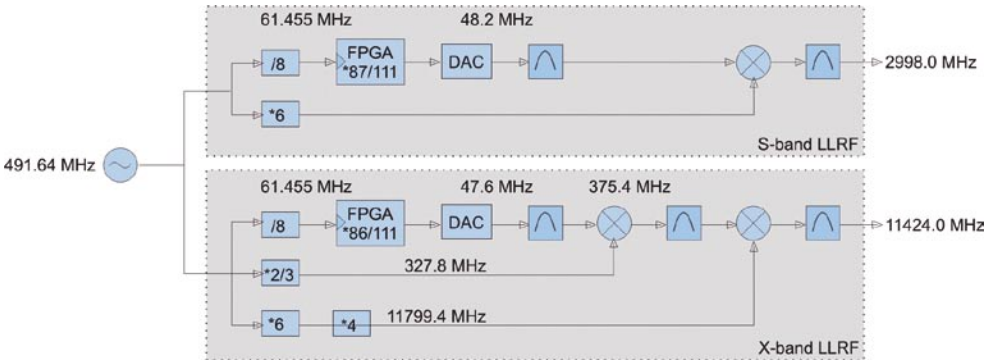

Figure 6.4.5:
Single station RF controller block diagram.

6.4.4.3 Synchronization System

The synchronization system will distribute phase references to each station. The specifications correspond to maintaining a sub 100 fs synchronicity across the 300 m of the facility. Integration of the synchronization system with the local RF controllers is essential. Such system is described in detail in Chapter 10. Figure 6.4.6 shows the block diagram of the system and its integration with the RF controllers.

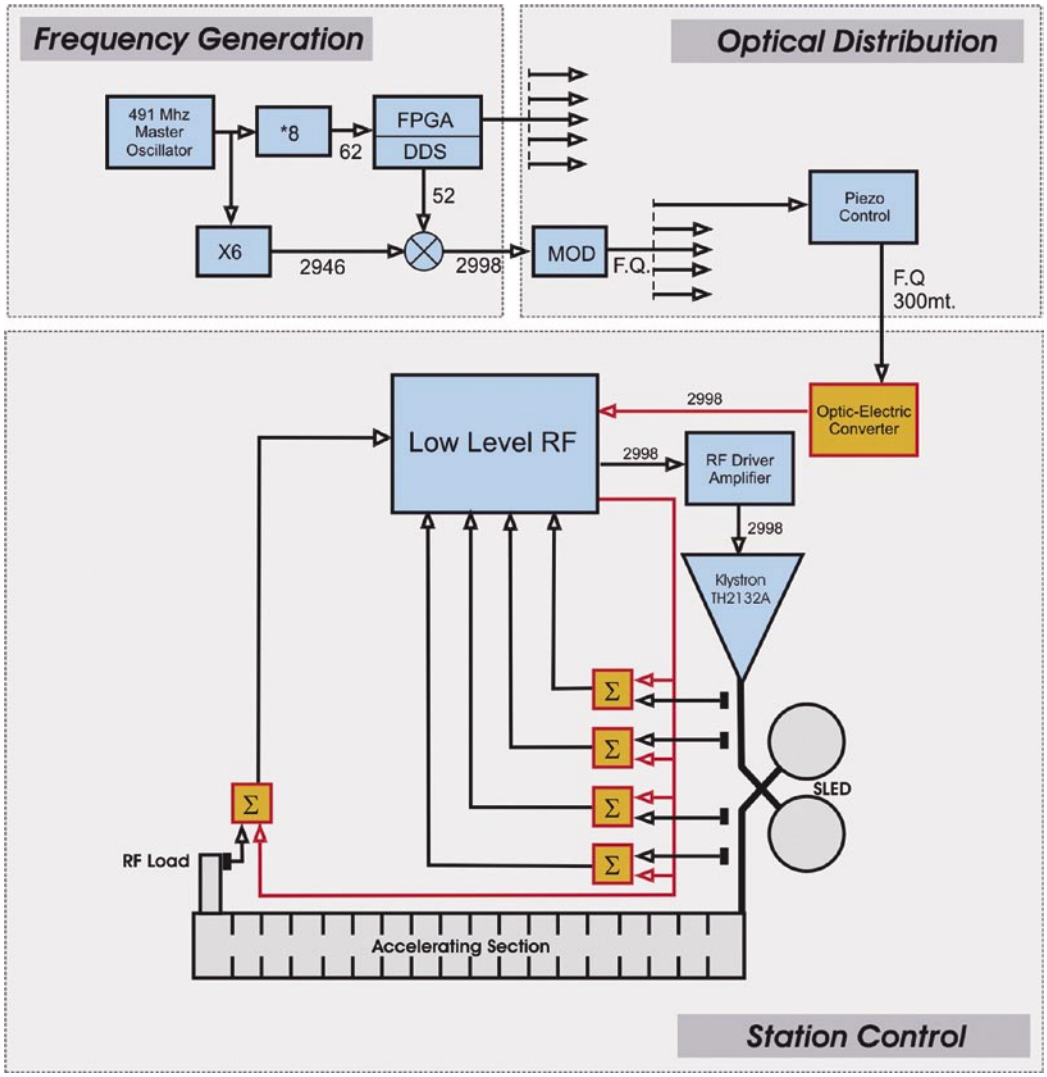

Figure 6.4.6:
Block diagram of the integration of synchronization and RF control systems.

6.4.4.4 Auxiliary Systems

The linac upgrade will require both the construction of new systems as well as the upgrade of several auxiliary systems that are part of the existing linac. In addition to the systems already described here, such systems include:

- Control system
- Feedback systems
- Vacuum system
- Beam instrumentation and feedback systems
- Conventional facilities (buildings, utilities)

In addition to the extension of the linac building and klystron gallery, the linac upgrade will require the installation of new AC power and water cooling capacity to be able to energize and cool the additional sections that will be installed. This corresponds to 1.5 MW of AC total power (whose 0.5 MW of the existing accelerator) at 50 Hz and to 300 kW of heat load on the existing systems, excluding the auxiliary systems.

Several of the existing systems will be upgraded. Some of them, like the controls and vacuum systems, benefit from the ongoing booster construction, where the new hardware is already being deployed and therefore the linac upgrade will be an extension of the existing construction. Others, like feedbacks and beam instrumentation, need significant upgrades to meet more demanding specifications.

6.4.5 Linac Stability

Sensitivity studies have been performed to determine the variation of the Linac output parameters with respect to the phase and amplitude jitters of the accelerating fields, electron bunch charge and electron emission time at the cathode (see, Chapter 5). The obtained sensitivities have been used to form a tolerance budget for each segment of the Linac (L1-L4 and the X-band structure). They provide a collection of tolerances that need to be met.

The results indicate that the most stringent phase specifications concern the first Linac segment (L1), while the tightest amplitude control is required on L4. In this process a tolerance budget among the various elements of the Linac was allocated, trading off amplitude and time jitter in the RF gun with those of each accelerating section. The corresponding specifications in amplitude and phase result in the tightest phase control in L1 (0.09 ^{o}S) and amplitude control in L4 (0.05%). While the present RF systems have not yet achieved these demanding goals, some preliminary measurements were performed on the existing systems. So far, stability of the order of 0.1% amplitude and 0.1 ^{o}S can be achieved, not including potential benefits from the noise correlation among different stations in the Linac [12]. With the above conditions, the error tracking analysis showed a satisfactory result in the final slice energy and peak current as a function of the time defined by the master clock. In order to be able to assess the stability of the existing systems, preliminary phase jitter measurements were performed on some of the present RF transmitter in operation at ELETTRA. While operating at 10 Hz, four of the existing systems (MK3, MK4, MK5 and MK7) were tested by observing the pulse to pulse variation of the mean (integrated) phase in the range from 1 sec. up to 10 min. (10 to 6000 pulses). The measurement setup is shown in Figure 6.4.7.

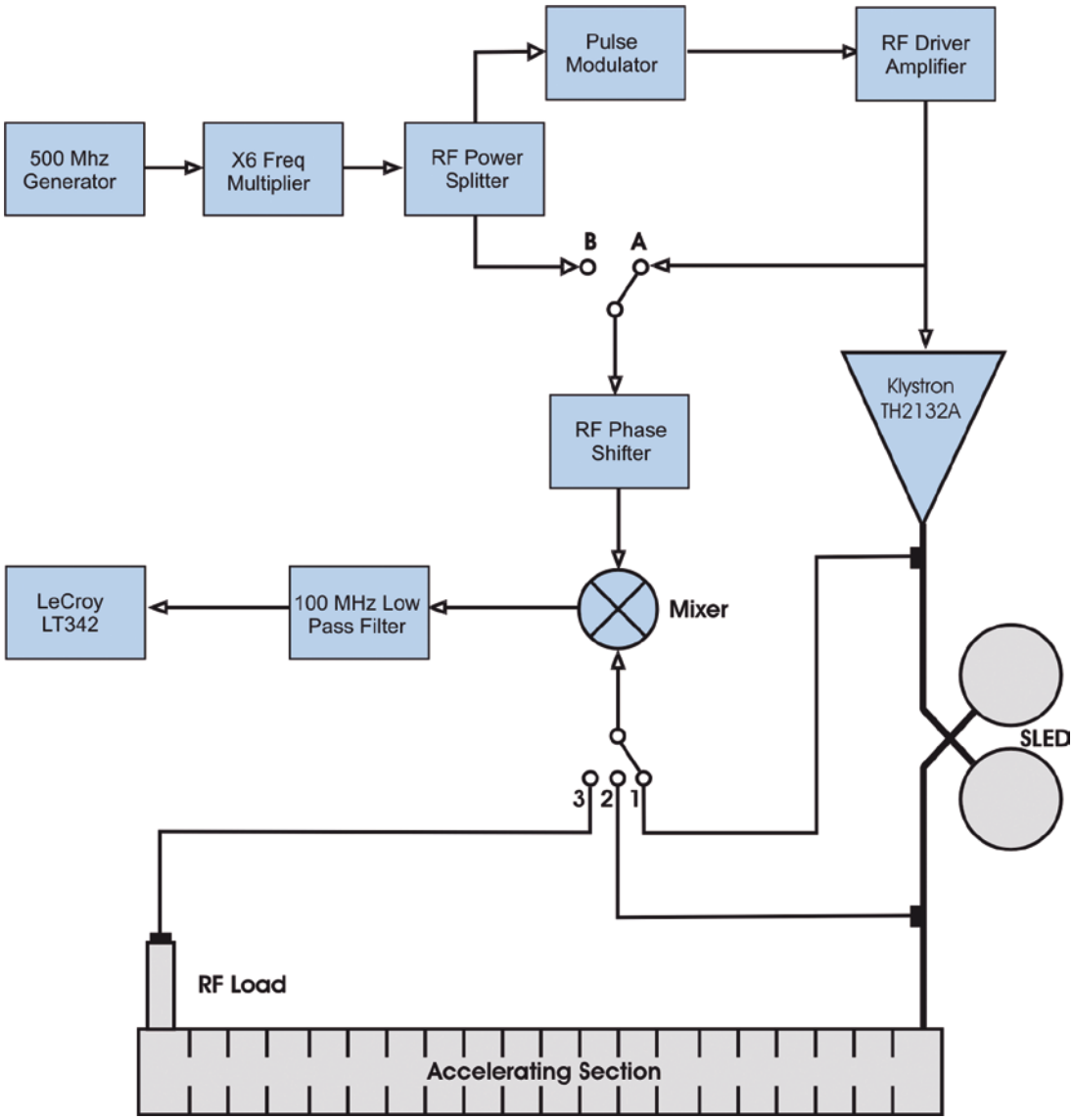

Figure 6.4.7:
Phase jitter measurement layout.

As one can see from the scheme, the measurements tried to characterize all the system's components, from the klystron up to the RF water load of the accelerating section. The phase noise was measured over 1 μsec of the 3.0 μsec total RF pulse length. Table 6.4.4 reports the results of the measurements.

Table 6.4.4: Pulse to pulse main phase variation (^{0}S rms).

	MK3	MK4	MK5	MK7	AVG
			Klystron (pos: A-1)		
1 sec	0.031	0.048	0.034	0.019	0.033
5 sec	0.036	0.048	0.034	0.030	0.037
10 sec	0.036	0.037	0.034	0.034	0.035
30 sec	0.036	0.070	0.038	0.030	0.043
1 min	0.041	0.092	0.041	0.030	0.051
5 min	0.056	0.088	0.038	0.049	0.058
10 min	-	-	-	-	-
			Driver-Klystron (pos: B-1)		
1 sec	0.056	0.038	0.049	0.034	0.044
5 sec	0.067	0.038	0.053	0.060	0.055
10 sec	0.056	0.042	0.057	0.053	0.052
30 sec	0.078	0.069	0.057	0.060	0.066
1 min	0.111	0.046	0.064	0.056	0.069
Time	0.108	0.080	0.200	0.060	0.112
10 min	0.130	0.096	0.230	0.120	0.144
			Driver-Klystron-SLED detuned (pos: B-2)		
1 sec	0.045	0.069	0.071	0.069	0.064
5 sec	0.068	0.061	0.056	0.084	0.067
10 sec	0.057	0.058	0.060	0.065	0.060
30 sec	0.079	0.061	0.060	0.084	0.071
1 min	0.090	0.088	0.056	0.126	0.090
5 min	0.188	0.104	0.075	0.168	0.134
10 min	0.354	0.561	0.188	0.172	0.319
			Driver-Klystron-SLED detuned-Section (pos: B-3)		
1 sec	0.153	0.169	0.177	0.098	0.149
5 sec	0.138	0.184	0.162	0.184	0.167
10 sec	0.181	0.157	0.181	0.162	0.170
30 sec	0.169	0.184	0.211	0.218	0.196
1 min	0.173	0.184	0.238	0.169	0.191
5 min	0.358	0.338	1.076	0.237	0.502
10 min	0.634	0.441	1.027	0.335	0.609

The last column shows the average values over the four stations. Acquisition problems resulted in the missing data klystron (A-1), 10 min. period. A preliminary analysis shows that the pulse to pulse variation of the mean phase remains within acceptable levels; for example, the klystron (A-1) stays within 0.04 ^{0}S over 1 sec. (10 pulses), reaching 0.06 ^{0}S in 5 min. (3000 pulses). The same parameters vary between 0.15 ^{0}S and 0.6 ^{0}S over the whole system, thus is required a feedback system capable of keeping the transmitters within the specifications.

Figure 6.4.8 shows the oscilloscope trace relative to the acquisition of 3000 pulses from the klystron in the MK5 section: over 5 min. of statistics, the pulse to pulse integrated phase variation is below 0.06 ^{0}S.

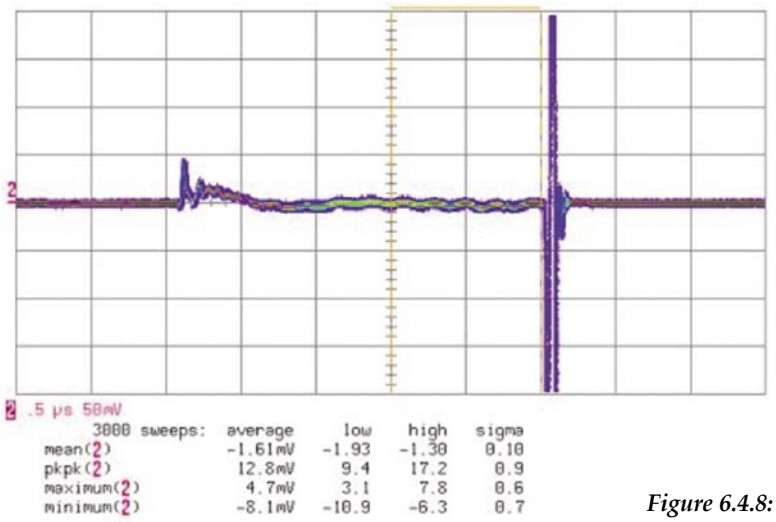

Figure 6.4.8:
MDK5 Klystron 1 µsec averaged phase noise (3000 pulses, 5 min).

6.5 The Geometric Wake Functions of the Accelerating Structures

The geometric wake functions of the accelerating structures in the FERMI Linac plays an important role in the formation of the final electron beam [13]. Particular care was taken in the management of the wakefields in the BTW structures, which have the highest impedances, as shown in Figure 6.5.1.

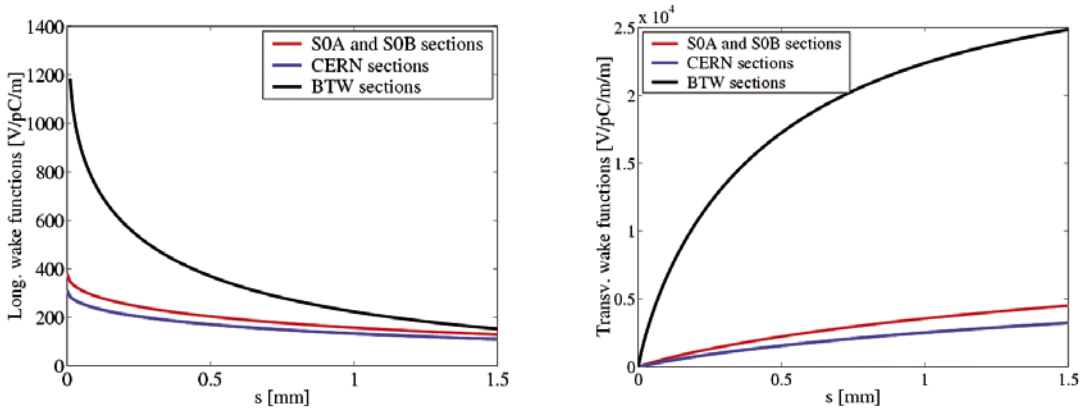

Figure 6.5.1:
Longitudinal (left) and transverse (right) wake functions of the accelerating structures used in the FERMI Linac.

The longitudinal wake field introduces second and third order energy chirps, thus reducing the compression efficiency and leading to current spikes at the bunch edges. The wake field in L4 increases the final correlated energy spread, with an impact on the HC FEL bandwidth [14]. The transverse wake field, driven by trajectory distortion caused by field errors and elements misalignment, induces the BBU instability, that is, a correlation in the transverse-longitudinal particle positions. The instability increases the projected emittance by causing a launching error and an optical mismatch of the bunch-trailing electrons. An in-depth study of the wake functions was performed and techniques are proposed to minimize the phase space dilutions. The wake functions of the three types of accelerating sections have been calculated in [15,16] using analytical approximation for the S0A, S0B and CERN sections and a time domain code for the BTW sections [17].

6.5.1 Longitudinal Wake Potentials

For a longitudinal charge distribution λ_z, the voltage gain of a test electron due to the electromagnetic wakes of the electrons behind of it is given by the wake potential [18]:

$$W(s) = -\int_s^{\infty} w(s-s')\lambda_z(s')ds' \qquad 6.5.1$$

It was found that by computing the short-range wake numerically and fitting it with a simple function, one can obtain a result that is valid over a large range of s (position along the bunch) and over a useful range of parameters [19]; this consideration applies to the steady state situation, which is reached in an approximate distance $a^2/2\sigma_z$ (where a is the section aperture and σ_z the rms bunch length) from the entrance of the accelerating section, by fitting generally short with respect to the section length (about 0.5 m for a 200 fs bunch and 5 mm aperture). In what follows, the steady state wake functions [18] will be used.

For S0A and S0B accelerating structures one obtains:

$$w(s) = 380\exp\left(-\sqrt{s(mm)/1.28}\right) \quad \left[\frac{V}{pC\,m}\right] \qquad 6.5.2$$

For the CERN accelerating structures:

$$w(s) = 311\exp\left(-\sqrt{s(mm)/1.38}\right) \quad \left[\frac{V}{pC\,m}\right] \qquad 6.5.3$$

For the ELETTRA accelerating structures:

$$w(s) = 1345\exp\left(-\sqrt{s(mm)/0.3}\right) \quad \left[\frac{V}{pC\,m}\right] \quad \text{for } s<1 \text{ mm} \qquad 6.5.4$$

The wake potential in the BTW structures is stronger than in TW structures because of the magnetic coupling that requires a smaller iris radius. However, the former provides a higher energy gain.

It has been shown [13] that, for 1 nC charge distributed over 12 ps bunch length traveling through the S0A, S0B and L1 sections (for a total length of ~ 24 m), the cubic energy chirp is dominated by the longitudinal wake potential contribution.

The cubic energy chirp is responsible for the appearance of the bifurcation in phase space after the bunch compressors; this phase space distortion in turn leads to spikes in the peak current at the edges of the electron bunch [13]. It is therefore desirable to minimize it. One way to achieve this is to use a density distribution with the linearly ramped peak current shown with the bold line in Figure 6.5.2a. It gives a wake potential with a significantly reduced cubic chirp a_3=890 MV/nC (see also the bold line in Figure 6.5.2b). The part under the bold line in Figure 6.5.2 contains approximately 40% of the total charge.

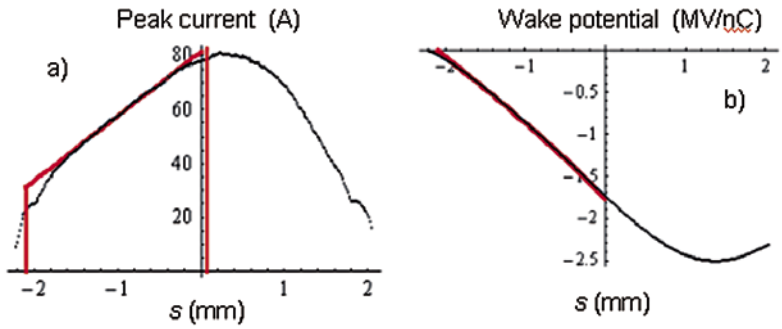

Figure 6.5.2:
Density distribution with a linear ramped peak current (a) and its corresponding wake potential (b). The bold line shows the ideal distribution and its associated wake potential, while the black line shows the actual distribution and wake potentials obtained in simulations.

6.5.2 Transverse Wake Potentials

As suggested in [15,16], an analytical approximation to the wake function for the TW structure (SØA, SØB and CERN sections) may be used for the transverse case. With the geometric parameters in [20] the transverse wake function up to 5 mm bunch length (s in meters) is:

$$w_{\perp}^{1}(s) = 9623 \cdot \left[1 - \left(1 + \sqrt{\frac{s}{0.60 \cdot 10^{-3}}} \right) \cdot e^{-\sqrt{s/0.60 \cdot 10^{-3}}} \right] \left[\frac{V}{pC \cdot m \cdot m} \right] \qquad 6.5.5$$

$$w_{\perp}^{1}(s) = 7524 \cdot \left[1 - \left(1 + \sqrt{\frac{s}{0.70 \cdot 10^{-3}}}\right) \cdot e^{-\sqrt{s/0.70 \cdot 10^{-3}}}\right] \left[\frac{V}{pC \cdot m \cdot m}\right] \qquad 6.5.6$$

For the BTW accelerating structure an analytical model was chosen which is a combination of periodic and one-cell structure solutions. The transverse wake function up to 2 mm bunch length is (s in meters) [17]:

$$w_{\perp}^{1}(s) = 27984 \cdot \left[1 - \left(1 + \sqrt{\frac{s}{0.12 \cdot 10^{-3}}}\right) \cdot e^{-\sqrt{s/0.12 \cdot 10^{-3}}}\right] + 13992 \cdot \sqrt{s} \left[\frac{V}{pC \cdot m \cdot m}\right] \qquad 6.5.7$$

The SØA, SØB and CERN sections are characterized by relatively weak wake fields compared with the S-sections.

6.6 Compression and Longitudinal Dynamics

In order to achieve high peak current and small energy spread the electron beam must be manipulated in longitudinal phase space. This is normally achieved by using a series of RF accelerating structures and magnetic chicanes (bunch compression system). It is desirable that this process remains linear in order to avoid bifurcation in longitudinal phase space and high peak current spikes at the edges of the electron bunch. A distribution as uniform as possible is also aimed for, as it provides the maximum peak current in the main body of the bunch and narrows the bandwidth of the FEL output.

6.6.1 Magnetic Compression

The rms bunch length after the BC1 is [21,22,23]:

$$\sigma_z = \left\langle s^2 - \langle s \rangle^2 \right\rangle = \sqrt{(1 + hR_{56})^2 \sigma_{z0}^2 + (R_{56}\sigma_{\delta 0})^2} \approx |1 + hR_{56}| \sigma_{z0} \qquad 6.6.1$$

where σ_{z0} and σ_{d0} are the rms bunch length and uncorrelated energy spread before BC1. The compression factor is:

$$C = \frac{\sigma_{z0}}{\sigma_z} \approx \frac{1}{1 + hR_{56}} \qquad 6.6.2$$

The uncorrelated energy spread after the compression is $C\sigma_{\delta 0}$.

A 4-th harmonic cavity, called the "linearizer" in Figure 6.1.1, helps to linearize the energy chirp before BC1 [21,22,23]. The quadratic energy chirp is zero if the following condition is imposed [8]:

$$U_4 = -\frac{U_0 + U_1 \cos(\phi_1)}{16 \cos(\phi_4)} \qquad 6.6.3$$

where U_0 is the acceleration amplitude of the two accelerating sections preceding the laser heater (see, Figure 6.1.1) where acceleration is on-crest; U_1 is the acceleration amplitude of the four accelerating sections placed between the laser heater and BC1, with off-crest acceleration at phase ϕ_1 (referred to the crest of the rf wave). U_4 and ϕ_4 are the amplitude and phase of the 4-th harmonic X-band cavity.

Similar considerations can be drawn for the second stage of bunch compression using L2, L3 and BC2.

6.6.2 Coherent Synchrotron Radiation

Coherent synchrotron radiation (CSR) in the bending magnets of the two bunch compressors plays a major role in the micro-fragmentation of the electron bunch. This CSR causes variation of the electron energy along the electron bunch. In the case of the long magnet with bending angle [24]:

$$\varphi_M \geq \left(24 \frac{\ell_b}{R}\right)^{1/3} \qquad 6.6.4$$

one can write for the rate of the electron bunch energy loss per unit length z of the magnet (see, refs in 4):

$$\frac{dE}{dz} = -\int_{-\infty}^{\infty} ds\, \lambda_z(s) F_{\parallel}(s) = -3^{2/3} \frac{N^2 e^2}{R^{2/3} \ell_b^{4/3}} \qquad 6.6.5$$

where N is the number of particles per bunch and λ_z the density distribution.

The electron bunch moves inside the vacuum chamber that acts as a waveguide for the radiation. Not all spectral components of the CSR propagate in the waveguide and therefore the actual radiated energy is smaller than in a free space environment (see, Figure 6.6.1).

Because of shielding [25 and refs in 4], CSR is suppressed in BC1 where the electron bunch length exceeds 2-3 ps and is only important in the 4-th magnet of BC2 where the bunch length shrinks below 1-1.5 ps. This magnet is 0.5 m long and has a 9.35 m bending radius. The calculated average energy loss per electron due to CSR in free space (i.e. without shielding) is 340 keV for a 0.7 ps long electron bunch but the steady state formula slightly overestimates the effect. Therefore, this study concludes that the CSR effects are less important than the wakefields perturbations of the linac discussed in the previous paragraphs.

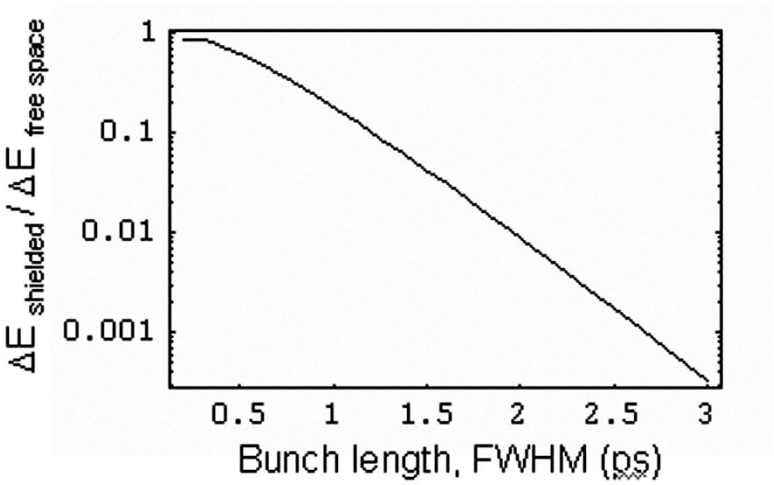

Figure 6.6.1:
Suppression of CSR by the vacuum chamber shielding.

6.6.3 Reverse Tracking

One of the problems faced by the accelerator optimization study was how to obtain, at the end of the accelerator, a distribution with as constant peak current and energy as possible along the electron bunch. Chapter 4 describes why this is a necessary performance aspect for the electron beam in order to optimize both the output power and bandwidth of the FEL radiation. This problem is considerably simplified by using the backward tracking technique justified and demonstrated in [13]. The technique consists in setting up a desirable "flat-flat" (in peak current and energy) distribution at the end of the linac. Starting with this distribution and tracking it backward, a nearly linear ramped peak current was obtained at the start of the linac. This is the reasoning that led to the ramped peak current distribution mentioned in paragraph 6.5.1 and used in start-to-end simulations.

6.6.4 Microbunching Instability

At a scale much smaller than the bunch length other additional effects gain significance. At this scale shielding is not effective and any microstructure in the charge distribution along the bunch will emit CSR as in free space. Such microstructures induce LSC forces which modulate the energy of electrons in the bunch. Together, the LSC and the CSR effects give rise to the so-called microbunching instability (μBI) that can be triggered even by the initial shot noise in the charge distribution [5 and refs in 4] at the cathode of the photoinjector. The end result of this perturbation is an increase of the slice momentum spread which, if it is too large, reduces the gain and increases the bandwidth of the FEL.

Simulations show that the entire machine acts as gigantic amplifier of the initial noise through a mechanism similar to self-amplification of spontaneous emission (SASE) in FELs. A reliable estimate of the growth of the momentum spread is at present fraught with uncertainty, as the simulations of the microbunching instability with particle tracking codes require a very large number of macroparticles; for example, a computation simulating the behaviour of a 6 ps long electron bunch (FWHM) using 10^6 macroparticles still generates a numerical noise approximately 50 times larger than the real shot

noise. The predictions are particularly uncertain in the second bunch compression where the instability gain is large, leading to a nonlinear evolution of its growth. Appendix A of this Chapter discusses the development of a Vlasov solver to overcome this problem.

The results presented in the next paragraph rely therefore on the linear theory [4 and refs. therein] and they assume an uncorrelated energy spread of the final beam of 150 keV rms.

6.6.4.1 Gain Function and Energy Landau Damping

The spectral dependence of the gain of the microbunching instability was calculated for the set of machine and electron bunch parameters listed in Table 6.6.1. The results are presented in Figure 6.6.2.

Table 6.6.1: Parameters relevant to the microbunching instability and used to calculate its gain.

Parameter	*Value*	*Units*
Uncorr. energy spread	2	keV
Beam energy	100	MeV
Compr. Factor BC1	4	
Beam energy BC1	220	MeV
Linac length up to BC1	30	m
Compr. Factor BC2	2.5	
Beam energy BC2	600	MeV
Linac length up to BC2	50	m
Linac length after BC2	70	m

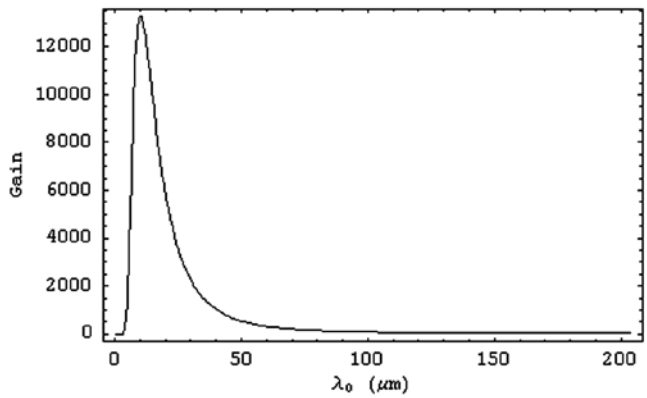

Figure 6.6.2:
Spectral gain function of the microbunching instability at the end of the linac in the linear approximation.

Because most of the microbunching instability gain occurs after BC2, one can effectively suppress it by using only BC1 for bunch compression [26]. Although this is a potentially attractive option, it is not yet sufficiently demonstrated because difficulties were encountered in obtaining "flat-flat" distribution at the end of the linac due to strong longitudinal wakefields in L3 and L4. This is an option that requires further studies and will be pursued in the future.

The slice energy spread in the electron bunch after the second bunch compressor was calculated by assuming that the energy spread induced by microbunching instability will eventually become incoherent energy spread. This approach results in an unacceptably large number for the momentum spread at the undulator entrance: σ_E= 4.3 MeV. To overcome this problem, a laser heater was proposed in [5]. It consists of a laser beam which, by interacting with the electron beam, increases its uncorrelated energy spread so that the μBI (see, Figure 6.6.2) is Landau damped.

At first, it is simply assumed that the laser heater provides additional energy spread which adds in quadrature to the existing, uncorrelated one generated by the photoinjector. Figure 6.6.3 shows the uncorrelated energy spread at the end of the linac as a function of the one induced by the laser heater alone for both the MLB and LB modes. The calculation is simplified by the fact that the interaction between the laser and the electron beam is weak because the required energy spread needed is small. In this case the changes in laser and electron dimensions along the interaction region can be neglected. Even the slippage effect is negligible because the slippage length is small with respect to the electron and to the laser pulse length. The heating process is therefore well described by the small gain theory with a single mode [27].

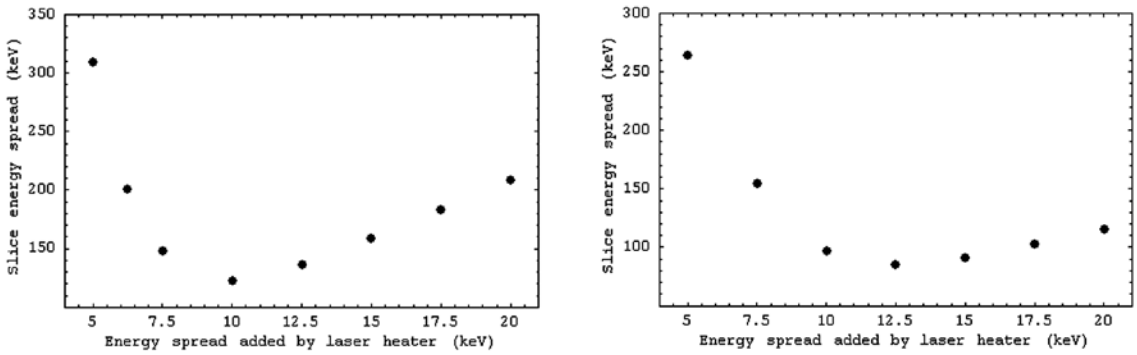

Figure 6.6.3:
Medium bunch (left) and long bunchs modes (right). Uncorrelated slice energy spread after the second bunch compressor as a function of the one added by the laser heater.

The gain in density modulation in a linear compressor due to an upstream energy modulation for a Gaussian energy distribution is [29]:

$$G(\lambda) = \left|\frac{b_f(\lambda_f)}{b_o(\lambda_0)}\right| = k_f R_{56} \frac{\Delta\gamma}{\gamma} e^{-\frac{1}{2}(R_{56} k_f \delta_0)^2} \qquad 6.6.6$$

where k_f is the compressed modulation wave number characterizing the instability, R_{56} is the momentum compaction of the magnetic chicane and δ_0 is average uncorrelated energy spread just before the compression. The Landau damping of the instability is proportional to the damping coefficient $e^{-\frac{1}{2}(R_{56} k_f \delta_0)^2}$.

Figure 6.6.4 shows the damping coefficient for a Gaussian energy distribution as function of the compressed modulation wavelength: the solid curve corresponds to 10 keV of rms uncorrelated energy spread boosted by the laser heater; the dashed curve reproduces the Landau damping provided at BC1 by the natural 2 keV rms energy spread of the beam without laser heater.

Eq. 6.6.7 describes the instability gain in 1-D approximation. If the transverse spatial distribution of the electron bunch is taken into account, then the energy distribution after heating is given by [28]:

$$v(\delta_0) = \frac{1}{\pi\sigma_x^2 \sqrt{2\pi}\sigma_\gamma} \int r dr \cdot e^{-\left(\frac{r^2}{2\sigma_x^2}\right)} \int \frac{d\xi}{\sqrt{(\Delta\gamma_L(r))^2 - (\delta_0 - \xi)^2}} e^{-\frac{\xi^2}{2\sigma_l^2}} \qquad 6.6.7$$

where *r* is the coordinate running over the transverse profile of the beam, σ_x is the rms transverse electron beam size, σ_y is the standard deviation of the Gaussian electron energy distribution before the interaction, ξ is the particle energy coordinate, δ_0 the mean energy spread of the beam $\Delta\gamma_L(0)$, the maximum energy modulation amplitude induced by the heater. In such a case, the instability gain assumes the form [29]:

$$G(\lambda) = \left|\frac{b_f(\lambda_f)}{b_o(\lambda_0)}\right| = k_f R_{56} \frac{\Delta\gamma}{\gamma} \int v(\delta_o) e^{-\delta_0} d\delta_0 \qquad 6.6.8$$

Eq. 6.6.9 reduces to eq. 6.6.7 in the 1-D approximation and for a Gaussian energy distribution.

In Figure 6.6.5 the damping coefficient is plotted as a function of k_f for different values of the ratio between the transverse dimension of the laser and of the electron beam, $B=\sigma_r/\sigma_x$, and assuming a total energy spread of 10 keV rms. For comparison, the outer line refers to the damping coefficient in the 1-D approximation and for a Gaussian energy distribution, as in eq. 6.6.7.

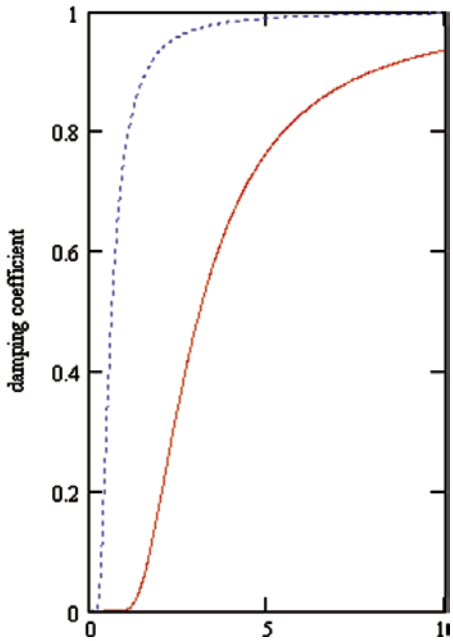

Figure 6.6.4:
Damping coefficient for 10 keV rms (solid line) and 2 keV rms (dotted line) of induced energy spread as function of the compressed modulation wavelength in microns.

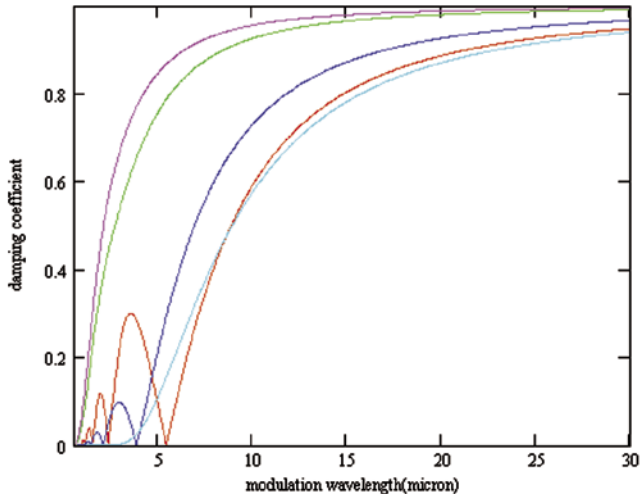

Figure 6.6.5:
Damping coefficient for different values of $B=\sigma_r/\sigma_x$ in the range 0.3 – 2.0. The modulation wavelengths are compressed.

The instability gain after BC1 was also calculated analytically including the energy modulation from the geometric wake field and from longitudinal space charge in L1 and including CSR in BC1. Figure 6.6.6 shows the instability gain as function of the compressed modulation wavelength, for three cases of the ratio $B=\sigma_r/\sigma_x$. An uncorrelated energy spread of 10 keV rms is assumed in the calculation.

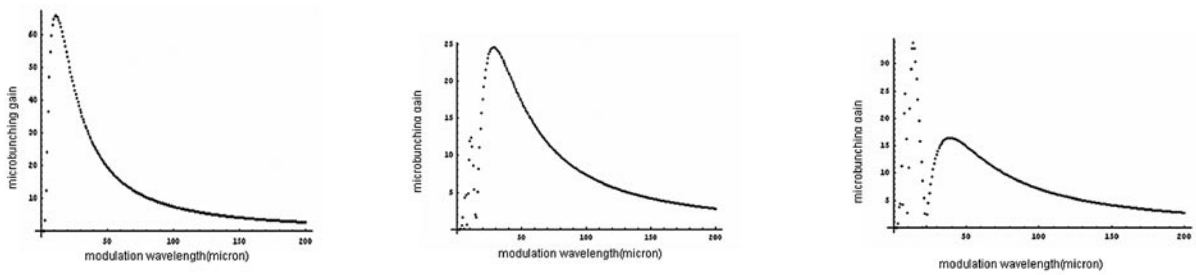

Figure 6.6.6:
From left to right, microbunching gain at BC1 for B=0.3, 1, 3. 10 keV rms uncorrelated energy spread. The modulation wavelengths are those of the compressed beam.

6.6.4.2 The Laser Heater

The laser heater consists of an undulator located in a magnetic chicane where a laser interacts with the electron beam, causing an energy modulation within the bunch on the scale of the optical wavelength (see, Figure 6.6.7). The corresponding density modulation is negligible and the coherent energy–position correlation is smeared by the chicane [8].

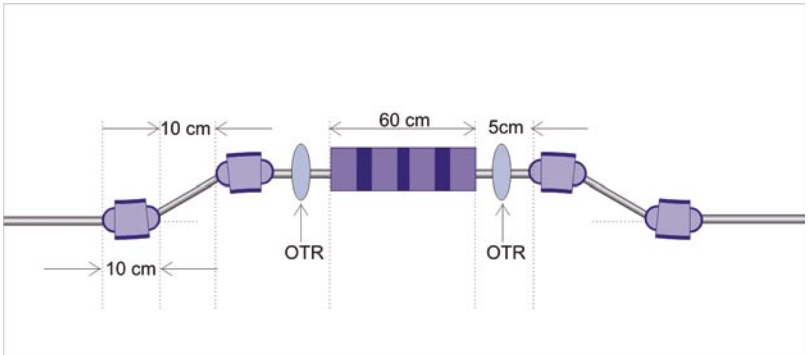

Figure 6.6.7:
Laser heater scheme.

According to [8], the induced energy spread should be in the range 10 – 17 keV. For a required energy spread, the needed laser power decreases quadratically with the electron beam transverse dimensions; at the same time, a too low a value of the transverse beam size makes the efficiency of the heating process more sensitive to the laser-beam transverse alignment. The specification for the accuracy of the alignment of both the external laser and the electron beam with the undulator axis is less then 0.1 mm.

A laser power of 1.6 MW is required to induce 10 keV rms energy spread for the MLB mode for a laser heater undulator with a Ti:Sa cathode laser operating at 780 nm. As for the LB mode, an uncorrelated energy spread of 12.5 keV asks for a laser power of 2.33 MW.

Since the slice parameters of the electron bunch, such as average energy, Twiss parameters, etc…, are not constant along the bunch, there is a different heating of the various longitudinal slices. In particular, a strong dependence of the induced energy spread has been found on the variation of the transverse beam size along the bunch (see, Figure 6.6.8). In order to achieve B>1 that is a bunch length at the laser heater longer than the transverse beam size, the laser is matched to the maximum slice transverse dimension.

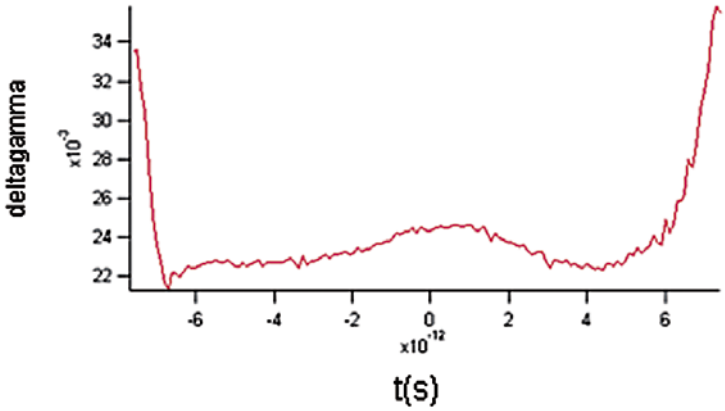

Figure 6.6.8:
Uncorrelated energy spread after heating.

The interaction of laser heater and electron bunch was studied through Elegant [30] for the MLB mode using the parameters reported in Table 6.6.2. The particle tracking includes an exact expression of the magnetic field of the undulator (without errors), a fundamental Gaussian mode laser and CSR in the chicane of the heater. The resulting slice energy spread is within 11.1 keV and 12.6 keV in the bunch core. The CSR effect on transverse emittance and energy spread is negligible.

Table 6.6.2: Parameters of laser heater for the MLB mode.

Number of undulator periods	12
Undulator periods	5 cm
Undulator k	0.487 (0.104 Tesla peak magnetic field)
Laser peak power	1.3 MW
Laser wavelength	780 nm
Laser waist	912.2 μm
Chicane bending angle	7.05 degrees
Chicane bending magnets length	10 cm
Chicane drift between bending magnets	10 cm
Chicane undulator's drift	80 cm
β_x before chicane	11.89 m
α_x before chicane	0.03
β_y before chicane	10.49 m
α_y before chicane	-3.332

As anticipated, the energy-position correlation induced by the heater decoheres by the small chicane because electrons with different divergences follow different paths independently of their longitudinal position if $\sigma_{x'} \times |R_{52}| > 780$ nm$/2\pi$. For the MLB mode, where $\sigma_{x'} = 26 \times 10^{-6}$, $|R_{52}| = 25$ mm. the condition for decoherence is $\sigma_{x'} \times |R_{52}| = 650$ nm.

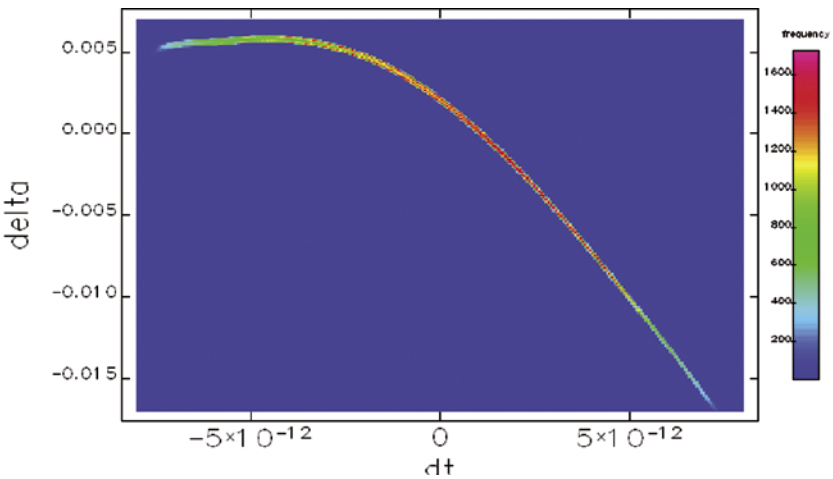

Figure 6.6.9:
Longitudinal phase space just after the laser heater. The interaction is described by the parameters listed in Table 6.6.2.

6.7 Transverse Dynamics

The main goal of the study of the transverse beam dynamics is the preservation of a small normalized emittance during acceleration and transport to the undulator. The factors contributing to emittance degradation may be caused by single particle dynamics and collective effects [4]. The single particle dynamics evaluates the consequences of geometric and chromatic aberrations of the lattice and of quantum fluctuations in the dispersive regions. The collective motion is described in terms of the beam break up (BBU) instability, since the CSR contribution has already discussed in Section 6.5. Trajectory distortions and their correction are also presented in this paragraph, together with specifications for the transverse acceptance.

6.7.1 Chromatic Aberrations

The emittance blow up caused by chromatic aberrations defines the tolerances on the dipoles and quadrupoles components of the field. The tolerances are evaluated below.

6.7.1.1 Dipoles

A quadrupolar and sextupolar field component in a dipole with horizontal dispersion D_x and horizontal beta function β_x dilutes the horizontal emittance through the generation of first and second order horizontal dispersion. The tolerances for the quadrupolar (b1) and the sextupolar (b2) components at a radius R from the magnetic axis with respect to the main field component (b0) are given by [31]:

$$\left|\frac{b_1}{b_0}\right| < \frac{1}{|\theta_b|}\frac{R}{\eta_x\sigma_\delta}\sqrt{\frac{2\varepsilon_{x0}}{\beta_x}\frac{\Delta\varepsilon_x}{\varepsilon_{x0}}} \qquad 6.7.1$$

$$\left|\frac{b_2}{b_0}\right| < \frac{1}{|\theta_b|}\left(\frac{R}{\eta_x\sigma_\delta}\right)^2\sqrt{\frac{\varepsilon_{x0}}{\beta_x}\frac{\Delta\varepsilon_x}{\varepsilon_{x0}}} \qquad 6.7.2$$

If the multipolar component is calculated at R = 20 mm, then an emittance growth of less than 1% is guaranteed by the following tolerances on all the dipoles: $|b_1/b_0| < 0.6\times10^{-4}$ at BC1 and $|b_1/b_0| < 1.5\times10^{-4}$ at BC2 for the quadrupolar component; $|b_2/b_0| < 1.2\times10^{-4}$ at BC1 and $|b_2/b_0| < 10\times10^{-4}$ at BC2 for the sextupolar component. Because of the very small energy spread at the Spreader ($\sigma_\delta < 0.1\%$), the tolerances about the multipolar components in those dipoles are more relaxed.

6.7.1.2 Quadrupoles

The chromatic aberration in a quadrupole is a 2nd order effect in the particle coordinates; it depends on the integrated quadrupole strength (*kl*), on the β-function at the quadrupole and on the relative energy spread of the particle (σ_δ):

$$\frac{\Delta\varepsilon}{\varepsilon} \cong \frac{1}{2}\beta^2\sigma_\delta^2(kl)^2 \qquad 6.7.3$$

The most critical point of the lattice from the point of view of chromatic aberrations is expected to be in proximity of BC1, where the rms correlated energy spread may reach a maximum value of about 3%.Eq. 6.6.3 has been evaluated and summed over all the linac sections, giving a total contribution to the emittance blow up of less than 6%.

6.7.2 Geometric Aberrations

The emittance blow up by geometric aberrations is evaluated for the sextupolar component in the dipoles only. The multipolar components in the quadrupole magnets have been found to be much smaller.

6.7.2.1 Dipoles

The second order geometric aberrations describe the quadratic dependence of the focusing strength on the transverse position of a particle. The systematic sextupolar component of the dipole field has been recognized to be the main source of geometric aberrations. Their effect on the emittance increase is [32]:

$$\frac{\Delta\varepsilon}{\varepsilon} \cong \frac{1}{2}(k_2 l)^2 x_0^4 \left(\beta + \alpha l + \frac{1}{4}\gamma l^2\right) \approx \frac{1}{2}(k_2 l)^2 \beta^3 \varepsilon \qquad 6.7.4$$

According to eq. 6.7.4, a sextupolar component of 4×10^{-4} at 20 mm leads to an emittance increase of less than 1%.

6.7.3 Quantum Fluctuations (ISR)

High energy electrons passing through a curved beam transport system emit Incoherent Synchrotron Radiation (ISR) and suffer from quantum excitations that increase the transverse emittance. The emittance blow up for a symmetric chicane of identical rectangular magnets is calculated with the following formula [32]:

$$\Delta\varepsilon_x \approx 8\cdot10^{-8}\cdot E^5[GeV]\cdot\frac{\theta^5}{l_b^2}\left[(L+l_b)+\left(\frac{\hat{\beta}+\check{\beta}}{3}\right)\right] \qquad 6.7.5$$

where E is the beam energy, L and θ are the dipole length and bending angle respectively, l_b the bunch length, β the Twiss function in the chicane.

This blow up becomes only significant for very high beam energies; thus, the largest effect is expected to be in BC2 at 600 MeV and in the Spreader at 1.2 GeV. The evaluation of eq. 6.7.5 for BC1, BC2 and the simulation result for the Spreader are summarized in Table 6.7.1.

Table 6.7.1: Emittance blow up due to the ISR emitted in the dipoles of BC1, of BC2 and of the Spreader (the unperturbed normalized emittance is 1.5 μm).

	$\Delta\varepsilon_x$ *[μm]*	$\Delta\varepsilon_x/\varepsilon\ [\%]_x$
BC1	4×10^{-4}	0.03
BC2	2×10^{-2}	1.33
SPREADER	4×10^{-2}	2.66

6.7.4 Trajectory Distortions

Alignment and field errors cause trajectory distortions which are corrected by means of a properly arranged scheme of steerers and Beam Position Monitors (BPMs). These errors are also sources of mismatch between the beam phase space ellipse and the Twiss ellipse of the transport line. The chromatic dependence of the betatron phase advance may cause filamentation of phase space with consequent emittance dilution. It may also diminish the effectiveness of the compensation of the transverse wakes by the orbit bump method described earlier (6.4.2). Misalignment studies have been performed under the assumption of independent mechanical supports of each of the magnetic elements and accelerating structures. Ground motion and vibrations have been assumed to be much smaller than the static errors.

6.7.4.1 Misalignment and Field Errors

Skew field components in dipoles and quadrupoles may lead to emittance blow up. The specifications for the elements alignment and field quality are listed below.

6.7.4.1.1 Dipoles

A roll angle ϕ_b of the dipoles generates a residual vertical dispersion which in turn leads to a vertical emittance dilution. The tolerance for the dipole roll angle is given by [31]:

$$\phi_b < \frac{1}{\theta_b \sigma_\delta}\sqrt{\frac{2\varepsilon_{y0}}{\beta_y}\frac{\Delta\varepsilon_y}{\varepsilon_{y0}}} \qquad 6.7.6$$

For a blow up $\frac{\Delta\varepsilon_y}{\varepsilon_{y,0}} \le 1\%$, the stronger constraint comes from the maximum bending angle at BC1 (θ_b = 0.085 rad) in presence of the maximum relative energy spread (σ_δ = 3%), giving a tolerance $\phi_b \le 830$ μm (rms value).

A dipole field error induces emittance blow up through parasitic dispersion according to [33]:

$$\frac{\Delta\varepsilon}{\varepsilon}(s) \cong \frac{1}{2} N_M \beta^2 \frac{\sigma_{err}^{'2}}{\sigma_\beta^2} \qquad 6.7.7$$

where N_M is the number of magnets affected by the error $\sigma'_{err} = \left(\frac{\Delta B \cdot l}{B\rho}\right)_{rms}$. A relative dipole field error of 5×10^{-5} contributes to an emittance blow up of less than 1%.

6.7.4.1.2 Quadrupoles

A roll angle $\phi_{q,1}$ of a quadrupole in a dispersion free region induces geometric coupling. The tolerance for the quadrupole roll angle is given by [31]:

$$\phi_{q,1} < \frac{1}{|kl|}\sqrt{\frac{2}{\beta_x\beta_y}\frac{\varepsilon_{y0}}{\varepsilon_{x0}}\frac{\Delta\varepsilon_y}{\varepsilon_{y0}}} \qquad 6.7.8$$

For $\frac{\Delta\varepsilon_y}{\varepsilon_{y,0}} \leq 1\%$, one obtains a relaxed constraint of $\phi_{q,1} \leq 20$ mrad (rms value) for an average focusing length f = 1/kl = 5 m and average betas of 20 m.

The skew field component in a dispersive region leads to a residual vertical dispersion and consequently to a vertical emittance dilution. In this case, the tolerance for the quadrupole roll angle becomes [31]:

$$\phi_{q,2} < \frac{1}{|kl|}\frac{1}{\eta_x\sigma_\delta}\sqrt{\frac{2\varepsilon_{y0}}{\beta_y}\frac{\Delta\varepsilon_y}{\varepsilon_{y0}}} \qquad 6.7.9$$

The condition $\frac{\Delta\varepsilon_y}{\varepsilon_{y,0}} \leq 1\%$ is satisfied by $\phi_{q,2} \leq 10$ mrad (rms value) for an uncorrected horizontal dispersion of 1 cm and an rms relative energy spread of 3%.

A lateral misalignment of the quadrupole also generates residual dispersion in both planes; for a given maximum allowed emittance growth the transverse alignment of the magnet should be [31]:

$$\Delta x, \Delta y < \frac{1}{|kl|}\frac{1}{\sigma_\delta}\sqrt{\frac{2\varepsilon_0}{\beta}\frac{\Delta\varepsilon}{\varepsilon_0}} \qquad 6.7.10$$

$\frac{\Delta\varepsilon}{\varepsilon_0} \leq 1\%$ is obtained by $\Delta x, \Delta y \leq 110$ μm (rms value) for the maximum conceivable energy spread $\sigma\delta = 3\%$.

Finally, field errors in both the normal and skew components of the quadrupole gradient generate emittance dilution according to [33]:

$$\frac{\Delta\varepsilon}{\varepsilon} \cong \frac{1}{2}N_M\beta^2k^2l^2\left(\sigma_\alpha^2 + \sigma_k^2\right) \qquad 6.7.11$$

where $\alpha = k\phi_{q,1}$ and N_M is the number of quadrupoles in the line. An rms gradient error $\sigma_k = 0.1\%$ and an rms roll angle $\phi_{q,1} = 300$ μm limit the emittance blow up to the order of 0.1%.

6.7.4.2 Launching Error

An optical mismatch of the beam phase space ellipse from the Injector into the start of the linac may cause emittance blow up through chromatic filamentation. In the pessimistic hypothesis of complete filamentation, a β-mismatch and a D-mismatch at the beginning lead to, respectively:

$$\alpha_i = 0 \Rightarrow \frac{\Delta\varepsilon}{\varepsilon} \cong \frac{1}{2}\left(\frac{\Delta\beta}{\beta}\right)^2 \qquad \frac{\Delta\varepsilon}{\varepsilon_\beta}(s) \cong \frac{1}{2}\sigma_\delta^2\left(\frac{\tilde{\eta}^2 + \left(\alpha\tilde{\eta} + \beta\tilde{\eta}'\right)^2}{2\varepsilon_0\beta}\right) \qquad 6.7.12$$

A β-mismatch of 5% causes an emittance blow up of 13%, while a residual dispersion D = 5×10^{-3} m with divergence D′ = 5×10^{-4} generates a blow up of up to 15%.

6.7.4.3 Trajectory Correction

A satisfactory trajectory correction can be obtained in the 120 m long FERMI Linac by using 40 pairs of correctors and 40 BPMs, active on both transverse planes. Each drift between two consecutive accelerating structures includes one BPM and one steerer, separated by a quadrupole magnet. This scheme allows both local and global methods of correction.

Particle tracking simulations have been performed with Elegant in a realistic operational scenario that includes reading the beam position at the BPM locations and correcting the trajectory in presence of transverse wakes.

Figure 6.7.1 shows an ensemble of trajectories, including field errors, elements misalignment and trajectory correction consistent with the tolerance errors budget shown in Table 6.7.2, Table 6.7.3 and Table 6.7.4. The trajectory correction requires an average kick per steerer of 1.5 mrad.

Figure 6.7.1shows that the rms off axis-trajectory is within 700 μm peak-to-peak in both planes.

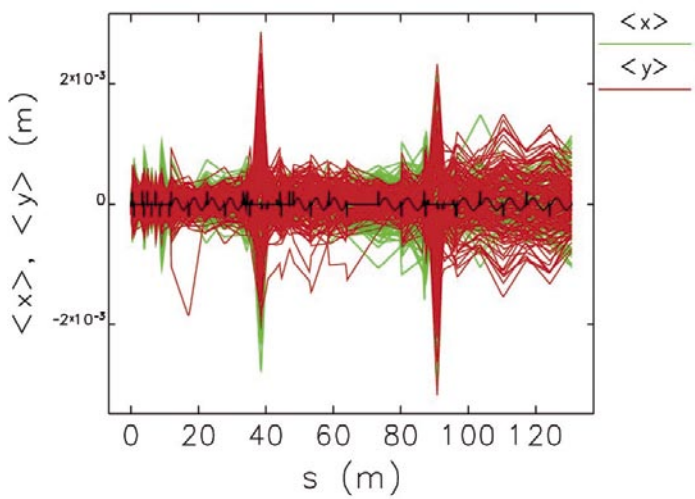

Figure 6.7.1:
Ensemble of 120 trajectories along the FERMI Linac after correction (Elegant simulations). It includes field errors and elements misalignment shown in the errors budget in Tables 6.6.2 - 6.6.4. The large excursion take place in the compression chicanes.

Table 6.7.2: Elements misalignment (rms values).

	Δx, Δy [μm]	*Δz [μm]*	*Δθ [μrad]*
Dipole	-	-	300
Quadrupole	150	200	300
BPM (30 μm RMS resolution)	150	200	-
Acc. Structure	300	-	-

Table 6.7.3: Field quality (rms values).

	Main field component [%]
Dipole	$\Delta B/B = 0.01$
Quadrupole	$\Delta K1/K1 = 0.1$

Table 6.7.4: Launching error.

	Nominal Set	*Jitter [p-t-p]*
$\lvert\Delta x\rvert$, $\lvert\Delta y\rvert$	100 μm	< 100 μm
$\lvert\Delta x'\rvert$, $\lvert\Delta y'\rvert$	100 μrad	-

6.7.5 The Beam Break-Up Instability

The wakefields in the S1-S7 Linac sections, with an impedance which is higher than of the rest of the linac, make this part of the layout particularly sensitive to the BBU instability. Possible solutions have been considered, inspired by the research of a similar effect in linear colliders. At the end, the local trajectory bump method was adopted. This method consists in an empirical search of a "golden" trajectory which makes the wake induced kicks compensating each other. By applying this scheme, the residual "banana shape" distortion of the transverse profile of the bunch corrected along its length can be reduced to be no greater than the nominal unperturbed rms beam size.

6.7.5.1 Theoretical Model

An analytical study based on a continuous model which describes the transverse motion of a single bunch in presence of transverse wake fields was performed in [37]. Such a study predicts the emittance growth under the combined influence of the short-range transverse wakefields, injection offsets, finite emittance and misaligned accelerating sections. It was found to be in good agreement with the numerical simulation results using Elegant, as Figure 6.7.2 shows. The comparison was repeated with different initial offsets and the results are listed in Table 6.7.5. The beam shape with the tailing particles traveling off-axis w.r.t. the head axis is here named "banana shape".

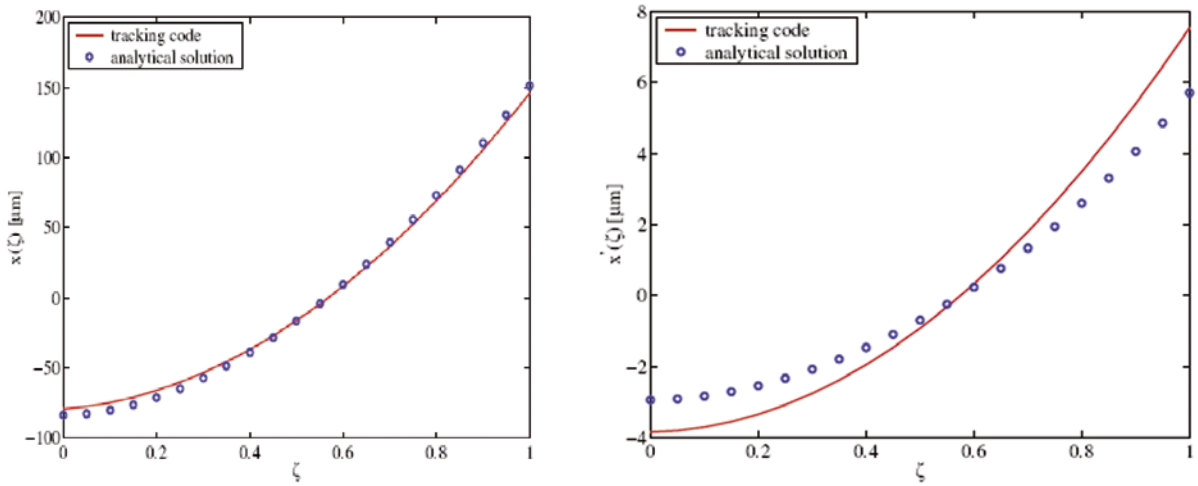

Figure 6.7.2:
Analytical (blue circles) and tracking (red line) results for the lateral displacement (a) and angular divergence (b) at the L4 end for an initial offset of 200 μm of a 0.33 nC, 200 fs long bunch.

Table 6.7.5: Analytical solution and ELEGANT tracking with FW bunch length of 200 μm and different initial offset X_0.

	ELEGANT	*Analytical*
X_0[μm]	$\varepsilon_{n,rms}$ [μm]	$\varepsilon_{n,rms}$ [μm]
50	0.08 × 10-2	0.08 × 10-2
100	0.33 × 10-2	0.34 × 10-2
150	0.75 × 10-2	0.76 × 10-2
200	1.32 × 10-2	1.34 × 10-2
250	2.07 × 10-2	2.10 × 10-2
300	2.97 × 10-2	3.02 × 10-2
500	8.24 × 10-2	8.40 × 10-2

6.7.5.2 Control of the Instability

The ensemble of trajectories subject to field errors, elements misalignment and steering corrections is plotted in

Figure 6.7.1. The corresponding banana shape distortions induced by the BBU instability at the Linac end are shown in Figure 6.7.3.

A parameter called Ratio was associated with each banana shape and is defined as the transverse deviation of the bunch tail with respect to the head in units of the beam size of a perfect, linear machine (nominal beam size). The banana shape obtained after a simple trajectory correction, hence without any particular attempt to preserve the emittance, increases the beam size by about 6.5 times over the 600 fs bunch duration; its maximum excursion is 2 mm with respect the bunch head. This numbers is unacceptable as it would compromise the FEL process [38].

For this reason a local bump was applied at the beginning of the Linac region where the transverse wakefields are strongest. Figure 6.7.3 shows that the change of sign of the horizontal trajectory after the bump reduces the final banana shape distortion to the level of one standard deviation of the nominal beam size. This is acceptable and gives confidence that this instability will not compromise the quality of the electron beam.

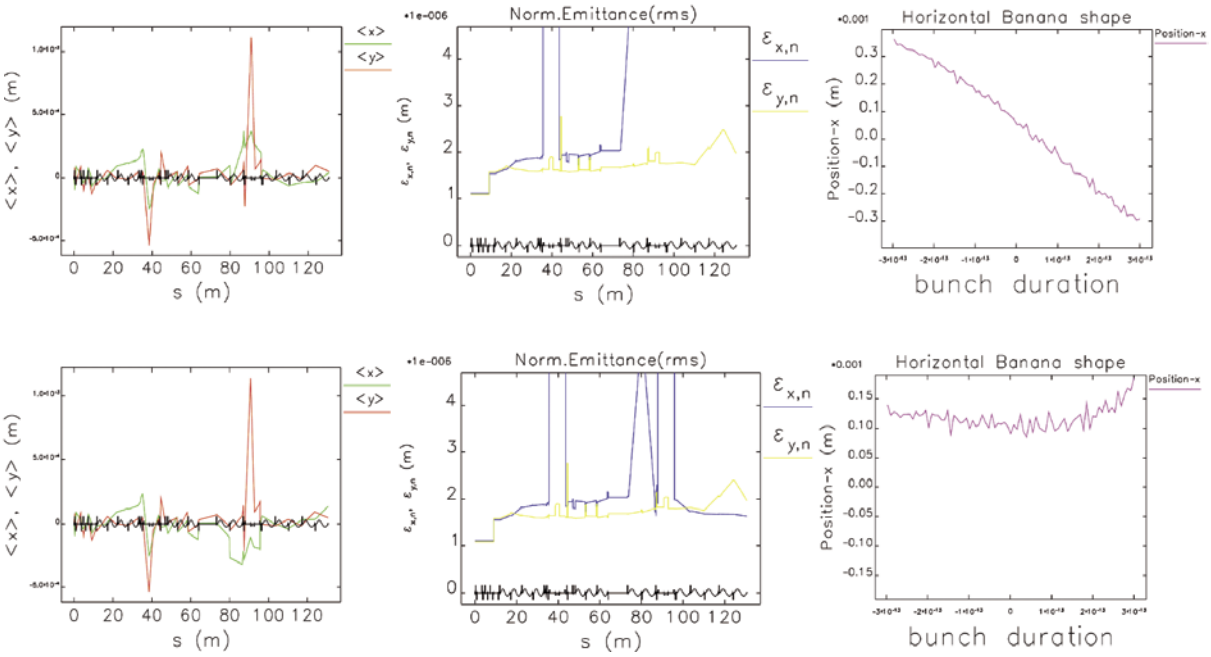

Figure 6.7.3:
Evidence of BBU instability in the horizontal plane, before the local trajectory bump (top plots) and after the bump (bottom plots). From left to right: electron bunch trajectory, evolution of the normalized transverse emittance along the Linac and banana shape in the horizontal plane at the Linac end.

6.7.5.3 Effect of Trajectory Jitter

Local methods of correction like the one used in the above example have the disadvantage of being dependent on the particular conditions of operation and jitters in some beam parameters. For this reason, a trajectory jitter – generated by varying the beam launching error – was simulated and the resulting in the banana shape was computed. Figure 6.7.4 demonstrates that a properly corrected banana shape is not appreciably affected by this jitter, since it remains below the 1-σ level.

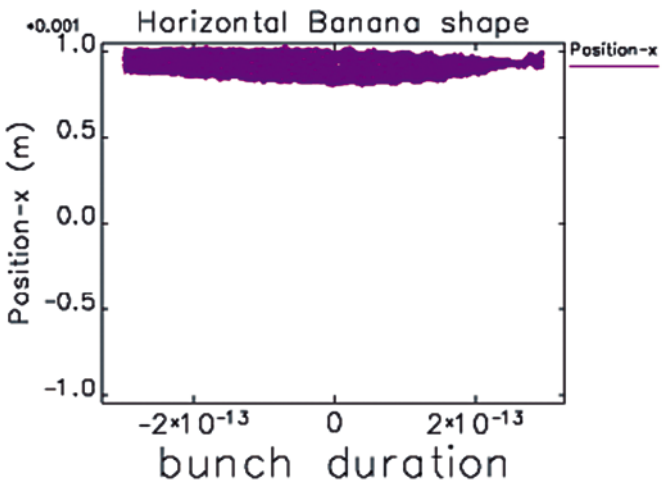

Figure 6.7.4:
Effect of the launching error jitter on the banana shape at the end of the Linac.

6.7.6 Transverse Acceptance and Error Tolerances

The "beam stay clear" region, i.e. the transverse aperture needed to comfortably accommodate the electron beam, including trajectory distortions, is calculated along the whole accelerator and spreader. The width of the vacuum chamber is also fixed according to the specification of the vacuum pressure in the linac.

6.7.6.1 Beam Size and Aperture

The optics from the Injector end to the Spreader end is shown in Figure 6.7.5. The horizontal dispersion in the two chicanes corresponds to the bending angles for the compression of the medium length bunch.

Table 6.7.6 shows that the chromatic contribution to the horizontal beam size is the only important difference between the different machine setups and it is always much bigger than the one due to betatron oscillations.

Table 6.7.6: Chromatic and geometric contributions to the horizontal emittance in the dispersive regions of the FERMI Linac.

Location	*Beam Size*	*SHORT*	*MEDIUM*	*LONG*
BC1	$\eta_x\sigma_\delta$ [mm]	3.1	5.7	4.0
	σ_β [mm]	0.20		
BC2	$\eta_x\sigma_\delta$ [mm]	0.7	1.9	2.6
	σ_β [mm]	0.150		
SPREADER	$\eta_x\sigma_\delta$ [mm]	0.130		
	σ_β [mm]	0.050		

The formula for the calculation of the "beam stay clear" includes the geometric ($\varepsilon_x\beta$) and the chromatic ($D_x\sigma_\delta$) contributions, as well as the off-axis displacement of the bunch centroid (after trajectory correction):

$$h.bsc = 1.2 \cdot \left(3\sqrt{\varepsilon_g \beta + (\eta_x \sigma_\delta)^2} + u_{oa}\right) \qquad 6.7.13$$

A margin of error of 20% is added to specify the minimum half -width of the vacuum chamber that is able to accommodate the beam along the Linac. Figure 6.7.6 and Figure 6.7.7 show, respectively, the behaviour along the Linac of the rms geometric emittances and of the rms correlated energy spread (MLB mode). In dispersion free regions, h.bsc (6.6.14) assumes its maximum value in the horizontal plane at the beginning of the Linac, where h.bsc = 3.1 mm. An rms normalized emittance ε_n = 1.5 μm and an off-trajectory error u_{oa} = 1 mm are assumed. Because of the symmetry of optics in the two planes and of the round beam injected into the Linac, the same upper limit also applies in the vertical plane.

For a detailed evaluation of the width of the vacuum chamber in the chicanes the reader is referred to [7].

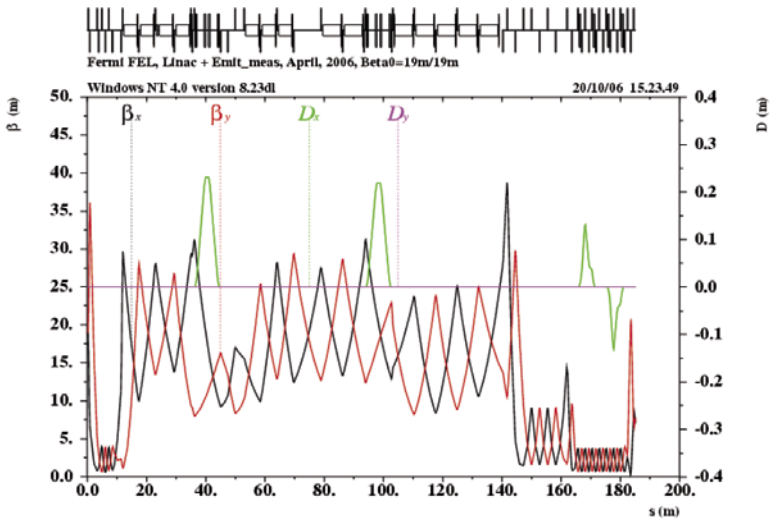

Figure 6.7.5:
FERMI Linac optics from the Injector end (where the beam average energy is 95 MeV) to the Spreader end (where the beam average energy is 1180 MeV).

The vacuum chamber aperture along the Linac and the Spreader is dictated by several constraints that include the vacuum pressure, the magnet design and the beam acceptance discussed above. Preliminary estimates indicate that a vacuum pressure lower than 10^{-7} mbar can be guaranteed in the Linac drifts with a vacuum chamber radius of 30 mm.

Table 6.7.7 summarizes some of the vacuum specifications in various regions of the electron beam.. The vacuum chamber apertures in the chicanes and in the Spreader are shown in Table 6.7.8.

Table 6.7.7: FERMI vacuum system. Main parameters.

Section	*Int. diameter [mm]*	*Material*	*Pressure [mbar]*	*Main pump [l/s]*	*# of pumps*
GUN	---	---	$<5\times10^{-9}$	---	---
LINAC	30	Stainless steel	$<1\times10^{-7}$	300	2 per module
UNDULATOR	30 (h) / 6 (v)	Aluminum	$<5\times10^{-6}$	40	1 per module

Table 6.7.8: Total width of the vacuum chamber in regions including dipoles.

Location	*Total width*	*Units*
BC1	450	mm
BC2	240	mm
Spreader $D_x=0$	4.0	mm
Spreader $D_x\neq0$	4.4	mm

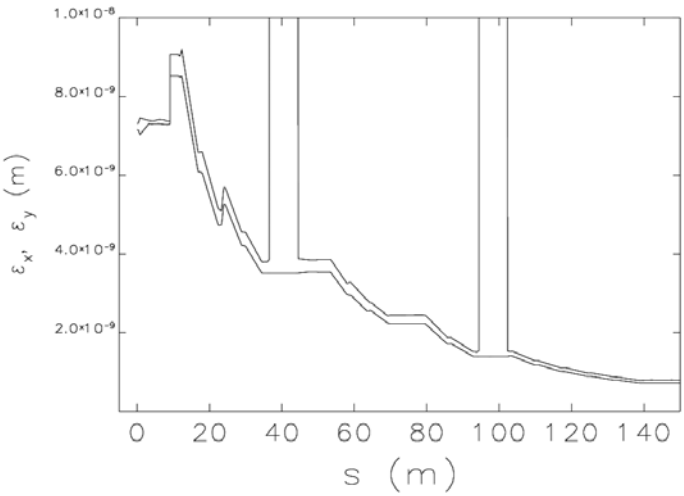

Figure 6.7.6:
Rms geometric emittances along the FERMI Linac for the MLB mode. The chromatic contribution to the emittance is included, as indicated by the fast reversible growth in the dispersive regions of the chicanes.

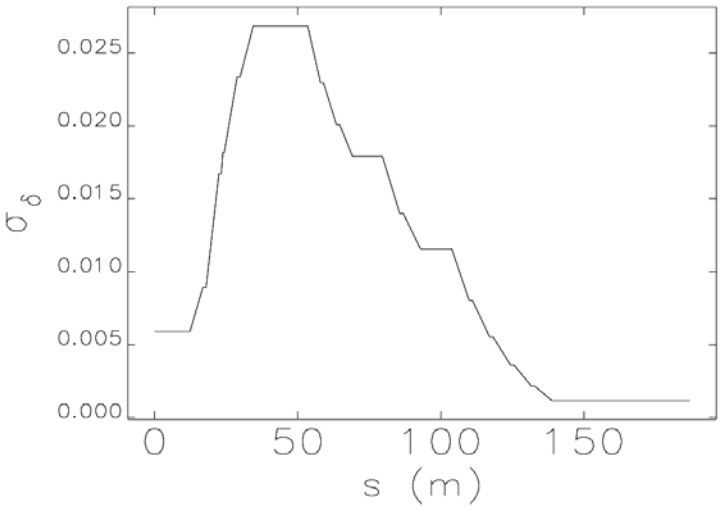

Figure 6.7.7:
Correlated rms energy spread along the FERMI Linac for the MLB mode.

6.7.6.2 Elements Misalignment

Analytical calculations and simulations are in agreement in predicting the tolerances on the alignment of the magnetic elements and of the accelerating structures required in order to avoid emittance blow up; they are summarized in Table 6.7.9. These tolerances are not sufficient to avoid the BBU instability, even though, in general, the suppression of BBU is made easier end more efficient as the misalignment of the elements in the lattice is reduced.

Table 6.7.9: Tolerances for elements misalignment, rms values. BPMs resolutions of 30 μm rms and maximum correction strength of 2 mrad have been assumed.

	Δx, Δy [μm]	*Δz [μm]*	*Δϕ Roll [mrad]*
DIPOLE	-	-	0.8
QUADRUPOLE	100	150	1.0
BPM	100	150	-
ACC. STRUCT.	150	-	-

The tolerances on the launching error at the beginning of the Linac are given below; they include the following contributions from the jitter of the bunch centroid position and divergence:

$$|\Delta x|,\ |\Delta y| < 100\ \mu m$$

$$|\Delta x'|,\ |\Delta y'| < 100\ \mu rad \qquad 6.7.14$$

6.7.6.3 Field Quality

The tolerances listed in Table 6.7.10 – Table 6.7.13 have been chosen to reduce the emittance blow up due to filamentation below the 1% level. The definition of the multipolar components is in [39].

Table 6.7.10: Tolerances for the quadrupole magnets of the Main Linac (LS – L4). LS includes Q_L1.1 and Q_L1.2. L1 and L2 include the quadrupoles near bunch compressor BC1 and BC2, respectively.

	LS	*L1*	*L2*	*L3*	*L4*	*Units*
# of Quads	8	13	6	3	6	
Integrated Gradient Range	0.04 – 1.06	0.01 – 0.58	0.06 – 0.56	0.01 – 0.77	0.09 – 2.17	T
Gradient Homogeneity in ± 10 mm	0.09	0.17	0.26	0.24	0.11	%
Sext. comp.: $\lvert b_2/b_1 \rvert$ at R=20 mm	4.7	8.6	13.2	12.2	5.6	%
Expected Total Length	150					mm
PS Stability (rms)	0.01					%

Table 6.7.11: Tolerances for the dipole magnets of the first bunch compressor (BC1).

# of Dipoles	4			
Magnetic Length [mm]	500			
Curvature Angle [rad]	0.055 – 0.085			
B_0 Range [T]	0.068 – 0.169			
Total Gap [mm]	30			
Magnets Type	Rectangular			
Expected Total Length [mm]	550			
Magnet Name	**B11**	**B12**	**B13**	**B14**
Field Homogeneity: $\lvert \Delta b_0 / b_0 \rvert$ at x=±25 mm [%]	0.075	0.008	0.009	0.138
Quadrupolar component: $\lvert b_1 / b_0 \rvert$ at R=20 mm [%]	0.06	0.006	0.007	0.11
Sextupolar component: $\lvert b_2 / b_0 \rvert$ at R=20 mm [%]	1.5	0.012	0.014	2.8
Decupolar component: $\lvert b_4 / b_0 \rvert$ at R=20 mm [%]	100	0.05	0.06	100
PS Stability (rms)	0.01 %			

Table 6.7.12: Tolerances for the dipole magnets of the second bunch compressor (BC2).

# of Dipoles	4			
Magnetic Length [mm]	500			
Curvature Angle [rad]	0.052 – 0.080			
B_0 Range [T]	0.168 – 0.386			
Total Gap [mm]	30			
Magnets Type	Rectangular			
Expected Total Length [mm]	550			
Magnet Name	**B21**	**B22**	**B23**	**B24**
Field Homogeneity: $\lvert \Delta b_0 / b_0 \rvert$ at x=±25 mm [%]	0.188	0.019	0.023	0.250
Quadrupolar component: $\lvert b_1 / b_0 \rvert$ at R=20 mm [%]	0.15	0.015	0.018	0.20
Sextupolar component: $\lvert b_2 / b_0 \rvert$ at R=20 mm [%]	10.6	0.10	0.11	14.1
Decupolar component: $\lvert b_4 / b_0 \rvert$ at R=20 mm [%]	100	0.5	0.5	100
PS Stability (rms)	0.01 %			

Table 6.7.13: Tolerances for the quadrupole magnets of the Spreader. SPRD2 quadrupoles include also Q_SPRD.5, Q_SPRD.6 with g < 14.3 T/m and L_m=0.1 m.

	DIAGN.-COLL.	*MATCH*	*SPRD2**	*SP2 FEL-2*	*SPRD1*	*SP2 FEL-1*	*Units*
# of Quads	7	4	10 + 2	4	12	4	
Integrated Gradient Range	0.20 – 4.07	0.80 – 7.31	1.12 – 7.25	1.35 – 10.25	1.12 – 7.25	1.35 – 10.25	T/m
Gradient Homogen. in ± 10 mm	0.024		0.09	0.09	0.014	0.09	%
Sext. comp.: $\lvert b_2/b_1 \rvert$ at R=20 mm	1.2		4.6	4.6	0.7	4.6	%
Expected Total Length	200	200	250	250	250	250	mm
PS Stability (rms)	0.01						%

Table 6.7.14: Tolerances for the dipole magnets of the Spreader.

	SPREADER FEL-1 + FEL-2
# of Dipoles	6
Magnetic Length [mm]	500
Curvature Angle [rad]	0.0523598
B_0 Range [T]	0 – 0.592
Total Gap [mm]	30
Magnets Type	Rectangular
Expected Total Length [mm]	550
Field Homogeneity: $\lvert \Delta b_0 / b_0 \rvert$ at x=±25 mm [%]	0.029
Quadrupolar component: $\lvert b_1 / b_0 \rvert$ at R=20 mm [%]	0.023
Sextupolar component: $\lvert b_2 / b_0 \rvert$ at R=20 mm [%]	2.16
Decupolar component: $\lvert b_4 / b_0 \rvert$ at R=20 mm [%]	10.0
PS Stability (rms)	0.01 %

6.7.6.4 Optical Mismatch at the Injection

Analytical calculations and preliminary results from jitter studies in time-dependent simulations provide indications on the tolerances of the optical mismatch of two electron beam Twiss parameters at the beginning of the Linac. They are listed below for an emittance dilution no larger than 10%

$$\begin{cases} D_i < 1 \ mm \\ D_i^{'} < 0.5 \ mrad \end{cases} \text{ and } \left(\frac{\Delta\beta}{\beta_0}\right)_i < 3\% \qquad 6.7.15$$

6.8 Beam Jitters Sensitivities and Effects of Errors

This paragraph addresses the problem of the unwanted variation of the accelerator settings during operation. The FEL operation requires stringent specifications for the stability of the linac output parameters: electron bunch arrival time, relative peak current and relative mean energy. In order to understand the sensitivity of these parameters to jitters of various error sources along the linac, an elaborate study using the tracking codes LiTrack [40] and Elegant [30] was performed and is reported in this section.

In section 6.8.1 the effect of errors on the longitudinal dynamics are described; the results were used to create a tolerance budget for some linac parameters. A slice-by-slice jitter analysis of the flatness of the longitudinal phase space is also presented, since this is a critical parameter in the FEL process.

In paragraph 6.8.2 the results of tracking studies that include realistic errors in the relevant accelerator parameters are presented. The Elegant code was used to generate a set of beam coordinates at the end of the linac. These coordinates were then picked up as inputs for the FEL simulations described in Chapter 4.

6.8.1 Longitudinal Dynamics

The LiTrack code was used for the sensitivity studies [8] of the FERMI linac, sketched in Figure 6.8.1. The simulation technique is described in [8]. It is to be noted that the medium length and Long bunch configurations requires different particle distributions, both with ramped peak currents from the photoinjector.

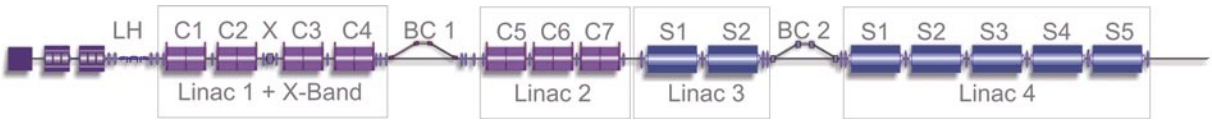

Figure 6.8.1:
Layout of the FERMI linac used in the sensitivities study with LiTrack.

The basic parameters of the linac and of the compressors used in the 1-D tracking simulations (LiTrack) and of the sensitivity studies can be found in Table 6.1.1, of Section 6.1.1.

6.8.1.1 Medium Length Bunch Mode

Table 6.8.1 lists the sensitivities of some electron beam parameters to RF phase, RF voltage and compressor chicane bend power supplies variations. Each sensitivity number quoted in the table independently causes a 10% peak current increase, a 0.1% relative mean energy increase and 150 fs final timing increase.

The sensitivities reported in Table 6.8.1 are used to generate a tolerance budget based on summing random, uncorrelated effects:

$$\sqrt{\sum_{i=1}^{14}\left(\frac{p_{tol}}{p_{sen}}\right)_i^2} < 1 \qquad 6.8.1$$

The sensitivities in Table 6.8.1 are weighting values for the summation in eq. 6.7.1. The overall tolerance budget is obtained by choosing the individual tolerances such that $p_{tol} < p_{sen}$ for all the indexes *i*. Table 6.8.1 lists the sensitivities for the MLB mode.

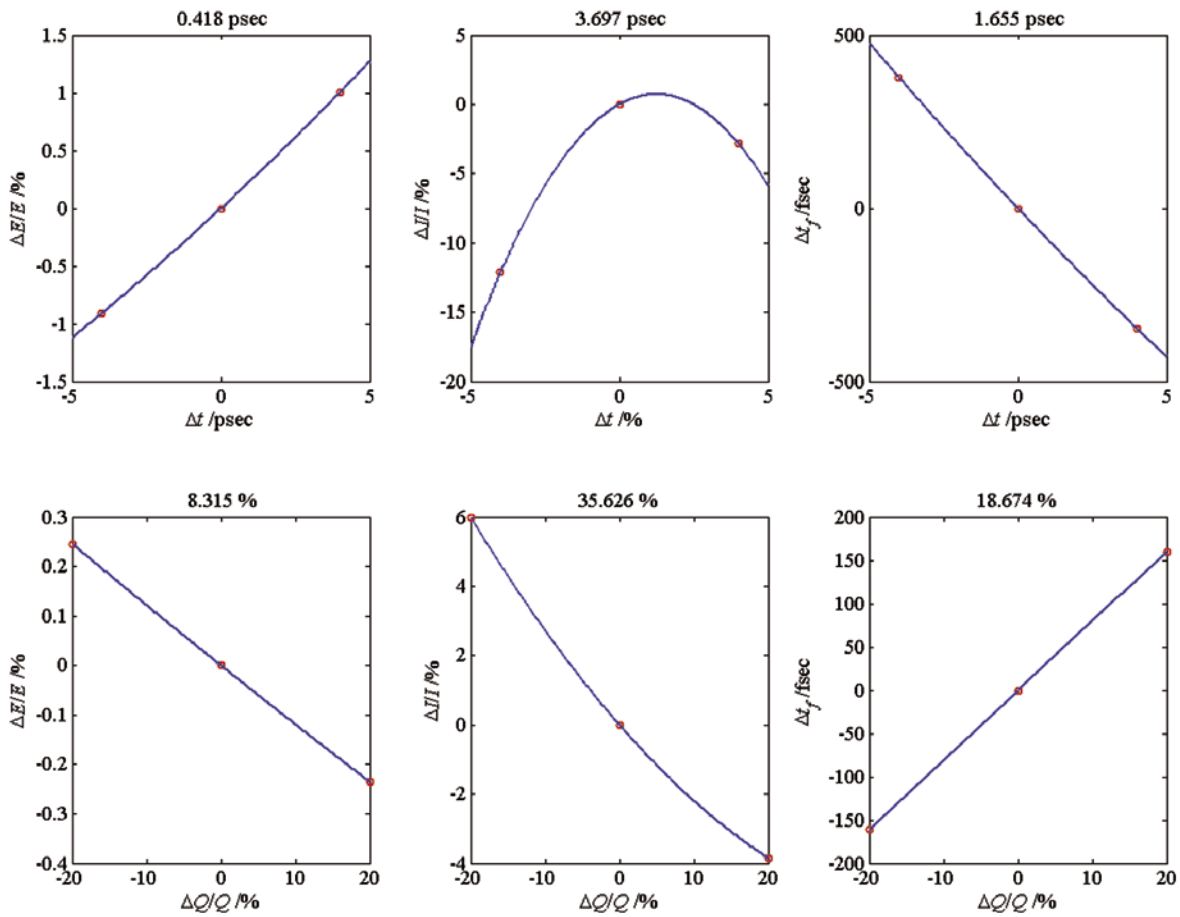

Figure 6.8.2:
Rms final relative mean energy ΔE/E, relative peak current ΔI/I and final timing jitter Δt_f as a function of gun timing jitter Δt_0 (upper plots) and relative initial bunch charge variations ΔQ/Q (lower plots).

Table 6.8.1: Individual rms sensitivities for the MLB mode. Each parameter variation causes a $\Delta I/I_0$=+10% peak current change or a $\Delta E/E_0$=+0.1% relative energy change and Δt = 150 fs timing change at the end of acceleration.

Parameters	S_{ee}.	*Unit*	*ΔI/I0=+10%*	*ΔE/E0=+0.1%*	Δt_f*=+150fsec*
L1 RF phase	ϕ1	S-band deg	-0.26	0.27	-0.18
LX RF phase	ϕx	X-band deg	0.85	-3.35	**9.81**
L2 RF phase	ϕ2	S-band deg	-4.24	0.96	-1.87
L3 RF phase	ϕ3	S-band deg	-2.48	0.56	-1.10
L4 RF phase	ϕ4	S-band deg	>10	-0.33	>10
L1 RF voltage	ΔV1/V1	%	**13.42**	0.48	-0.24
LXRF voltage	$\Delta V_x/V_x$	%	11.05	-3.85	2.06
L2 RF voltage	ΔV2/V2	%	-7.91	0.63	-1.19
L3 RF voltage	ΔV3/V3	%	-4.60	0.37	-0.70
L4 RF voltage	ΔV4/V4	%	>20	0.20	>20
Gun timing	Δt0	ps	**3.70**	0.42	-1.66
Initial charge	ΔQ/Q	%	-35.63	-8.32	18.67
BC1 chicane	ΔB1/B1	%	-1.56	1.59	-0.20
BC2 chicane	ΔB2/B2	%	-2.22	0.52	-0.27

Table 6.8.2 lists three possible tolerance budgets. If the first budget (fourth column in Table 6.7.3) is used, the relative peak current fluctuations at the linac end will be held to <10% rms. If the smaller tolerance from each column is applied (bold text), all three performance specifications ($|\Delta I/I|$<10%, $|\Delta E/E|$<0.1% and $|\Delta t_f|$<150 fsec) will simultaneously be met. We can see from Table 6.8.2 that the relative mean energy jitter is the leading output parameter that determines the tolerance on the photoinjector and linacs. It is worth pointing out that the tolerances on the voltage and phase of the accelerating section as well as of photoinjector parameters are exchangeable, i.e. the photoinjector parameters could be relaxed if the rf voltage is tightened and vice versa.

Table 6.8.2: MLB mode tolerance budget for <0.1% rms final relative mean energy, <10% rms peak current jitter or <150 fs final timing jitter. All the specifications are satisfied if the tighter tolerance is applied.

Parameters	S_y.	Unit	$\lvert\Delta I/I0\rvert$<10%	$\lvert\Delta E/E0\rvert$<0.1%	$\lvert\Delta t_f\rvert$<150 fsec
L1 RF phase	$\phi 1$	S-band deg	0.20	**0.10**	**0.10**
LX RF phase	ϕx	X-band deg	0.50	**0.30**	0.70
L2 RF phase	$\phi 2$	S-band deg	0.50	**0.10**	0.40
L3 RF phase	$\phi 3$	S-band deg	0.20	**0.10**	0.20
L4 RF phase	$\phi 4$	S-band deg	0.70	**0.10**	1.00
L1 RF volt.	$\Delta V1/V1$	%	1.00	**0.10**	0.15
LXRF volt.	$\Delta V_x/V_x$	%	0.80	**0.50**	**0.50**
L2 RF volt.	$\Delta V2/V2$	%	0.80	**0.10**	0.20
L3 RF volt.	$\Delta V3/V3$	%	0.50	**0.10**	0.15
L4 RF volt.	$\Delta V4/V4$	%	1.50	**0.05**	1.00
Gun timing	$\Delta t0$	ps	0.35	**0.25**	0.35
Initial charge	$\Delta Q/Q$	%	5.00	**3.00**	4.00
BC1 chicane	$\Delta B1/B1$	%	0.15	0.10	**0.02**
BC2 chicane	$\Delta B2/B2$	%	0.25	0.03	**0.02**

6.8.1.2 Long Bunch Mode

Table 6.8.3 shows the sensitivities in the LB mode.

Table 6.8.3: Individual rms sensitivities for the LB mode. Each causes ΔI/I0=+10% peak current change, ΔE/E0=+0.1% final relative energy change and Δt = 150 fs final timing change.

Parameters	S_y.	*Unit*	*ΔI/I0=+10%*	*ΔE/E0=+0.1%*	*Δt_f=+150 fsec*
L1 RF phase	ϕ1	S-band deg	-0.60	0.43	-0.23
LX RF phase	ϕx	X-band deg	1.53	-4.77	**10.05**
L2 RF phase	ϕ2	S-band deg	-2.66	0.92	-1.15
L3 RF phase	ϕ3	S-band deg	-1.55	0.54	-0.67
L4 RF phase	ϕ4	S-band deg	>10	-0.43	>10
L1 RF voltage	ΔV1/V1	%	1.81	0.55	-0.22
LXRF voltage	$\Delta V_x/V_x$	%	-45.95	-5.01	2.13
L2 RF voltage	ΔV2/V2	%	-8.14	0.57	-0.65
L3 RF voltage	ΔV3/V3	%	-4.74	0.33	-0.38
L4 RF voltage	ΔV4/V4	%	>20	0.20	>20
Gun timing	Δt0	ps	**8.01**	0.45	-3.16
Initial charge	ΔQ/Q	%	>40	-7.96	12.97
BC1 chicane	ΔB1/B1	%	1.67	-1.88	-0.26
BC2 chicane	ΔB2/B2	%	-1.93	0.36	-0.14

Table 6.8.4 shows that the relative mean energy jitter and the final timing jitter are the leading output parameter to influence the tolerance on photoinjector and linacs.

Table 6.8.4: LB mode tolerance budget required for <0.1% rms final relative mean energy, <10% rms peak current jitter and <150 fs final timing jitter.

Parameters	S_y.	*Unit*	$\lvert\Delta I/I0\rvert$=10%	$\lvert\Delta E/E0\rvert$=0.1%	$\lvert\Delta t_f\rvert$=150 fsec
L1 RF phase	$\phi 1$	S-band deg	0.30	**0.10**	**0.10**
LX RF phase	ϕx	X-band deg	0.70	**0.50**	0.90
L2 RF phase	$\phi 2$	S-band deg	0.60	**0.15**	0.25
L3 RF phase	$\phi 3$	S-band deg	0.50	**0.10**	0.15
L4 RF phase	$\phi 4$	S-band deg	1.50	**0.10**	1.00
L1 RF volt.	$\Delta V1/V1$	%	0.50	**0.10**	**0.10**
LXRF volt.	$\Delta V_x/V_x$	%	5.00	**0.50**	0.60
L2 RF volt.	$\Delta V2/V2$	%	2.00	**0.15**	**0.15**
L3 RF volt.	$\Delta V3/V3$	%	1.10	**0.10**	**0.10**
L4 RF volt.	$\Delta V4/V4$	%	2.00	**0.08**	1.50
Gun timing	Δt_0	ps	1.20	**0.25**	0.60
Initial charge	$\Delta Q/Q$	%	7.00	**3.00**	6.00
BC1 chicane	$\Delta B_1/B_1$	%	0.20	0.04	**0.02**
BC2 chicane	$\Delta B_2/B_2$	%	0.20	0.02	**0.02**

6.8.2 Global Jitter Study

The tolerances derived in the previous section for the phases and voltages of the accelerators and for the R56 compression parameters of the chicanes were applied to a statistical study that uses the technique of Latin Hypercube Sampling (LHS) [41]. A number of configurations having randomly picked RF voltages, phases and compression parameter within the specified tolerances were the input to LiTrack. A statistical analysis of global output parameters like mean energy, peak current and timing confirmed the tolerance budget. Further statistical analyses were done on a number of slices inside the bunch with a fixed slice length of 10 fs. The results of the medium and long bunch are shown in the following sections.

6.8.2.1 Medium Length Bunch Mode

Figure 6.8.3 shows the statistical results over 400 different configurations of the accelerations, compressions and photoinjector parameters.

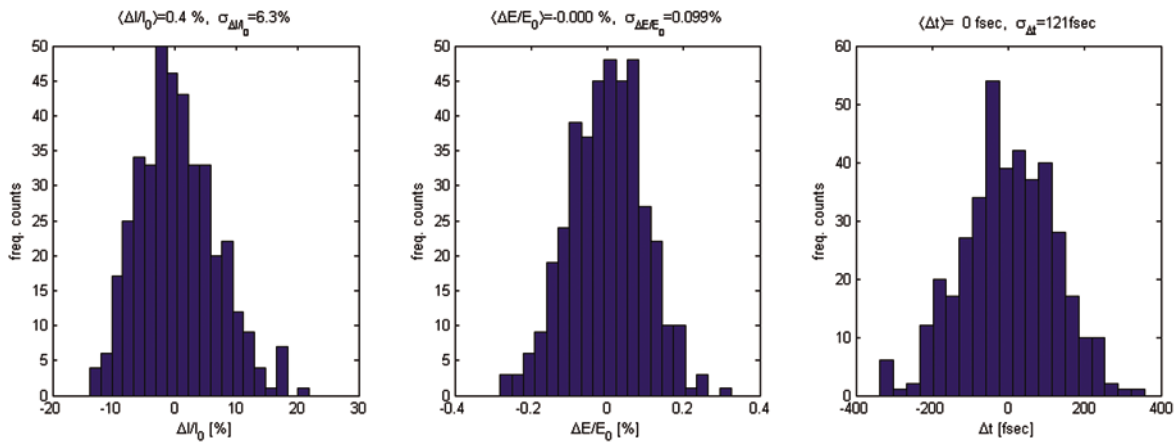

Figure 6.8.3:
Histograms for MLB mode of the relative peak current $\Delta I/I_0$ (left), final relative mean energy $\Delta E/E_0$ (center) and final timing jitter Δt_f (right). I_0 is the nominal peak current and E_0 is the nominal mean energy.

6.8.2.2 Long Bunch Mode

Figure 6.8.4 shows statistical results obtained in the same way as in the previous case (see, above)

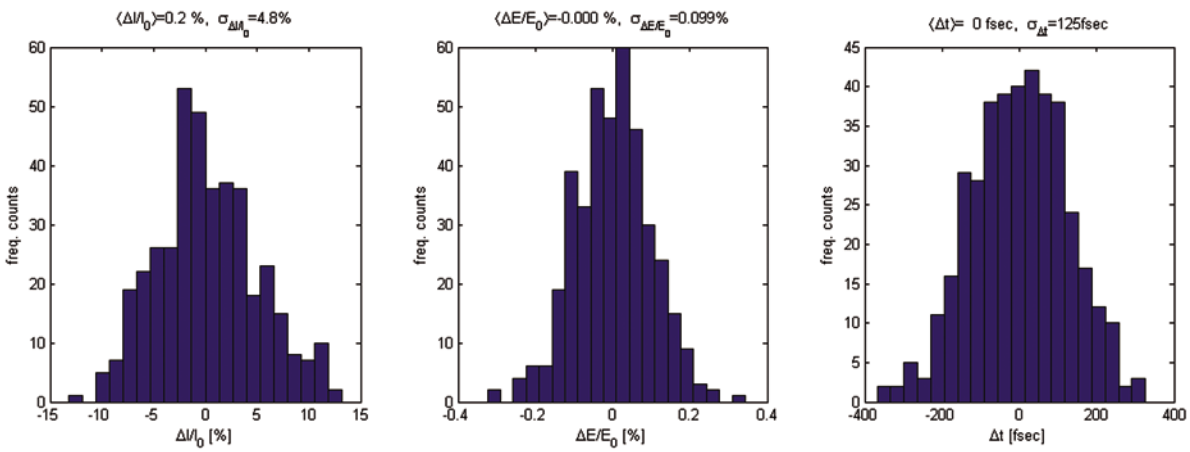

Figure 6.8.4:
Histograms for LB mode (lower plots) of the relative peak current $\Delta I/I_0$ (left), final relative mean energy $\Delta E/E_0$ (center) and final timing jitter Δt_f (right). I_0 is the nominal peak current and E_0 is the nominal mean energy.

6.8.3 Slice Jitter Analysis

An additional requirement is the need to have a longitudinal phase space as uniform as possible in the useful part of the bunch. Slice jitter studies have been conducted with 400 seeds for each linac configuration. For each seed the energy variation in the central part of the bunch is described by the following function:

$$E(t) = a_0\left(1 \pm \frac{\sigma_{a_0}}{a_0}\right) + a_1\left(1 \pm \frac{\sigma_{a_1}}{a_1}\right)\cdot t + a_2\left(1 \pm \frac{\sigma_{a_2}}{a_2}\right)\cdot t^2 \qquad 6.8.2$$

The flatness of the longitudinal phase space is defined as the average quadratic component in the energy chirp ($\hat{a}_2$) and its rms fluctuation (σ_{a_2}).

6.8.3.1 Medium Length Bunch Mode

Table 6.8.5 collects statistical parameters of the polynomial coefficients of eq. 6.7.2 that fit the E-t data in a least squares sense. The case reported here refers to the MLB mode.

Table 6.8.5: Statistical parameters of the polynomial coefficients for the MLB mode.

Medium bunch case M6				
	Unit	mean	rms	rms/mean %
a0	MeV	1140.86	1.140	0.10
a1	MeV/ps	0.0138	1.410	10220.94
a2	MeV/ps^2	3.570	1.030	28.95

Figure 6.8.5 shows a set of 10 randomly chosen seeds of the energy versus time along the bunch (left plots) together with the first derivative of the relative energy (central plots). The figure on the right shows the pattern of the first derivative when the quadratic chirp is removed.

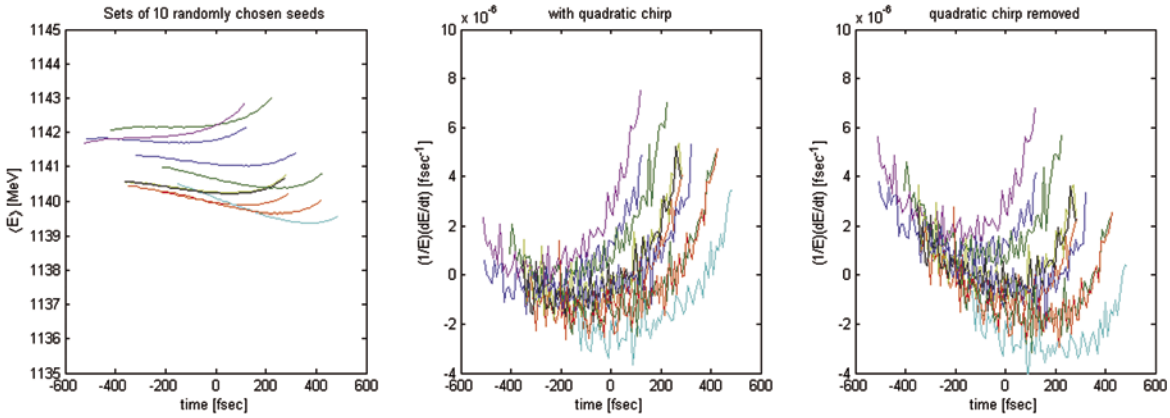

Figure 6.8.5:
Set of 10 randomly chosen seeds for MLB mode (b) (left plots) together with relative first derivative of the energy with respect to time inside the bunch with quadratic chirp (central plots) and with quadratic chirp removed (right plots).

6.8.3.2 Long Bunch Mode

The same statistical study applied to the long bunch gave the results shown in Table 6.8.6.

Table 6.8.6: Statistical parameters of the polynomial coefficients for the LB mode.

Long bunch case L4				
	Unit	mean	rms	rms/mean %
a0	MeV	1170.69	1.21	0.10
a1	MeV/ps	0.662	0.468	70.69
a2	MeV/ps^2	0.140	0.086	61.43

Figure 6.8.6 shows set of 10 randomly chosen seeds for the LB mode (left plots) together with first derivative of the energy deviation with respect to time inside the bunch with quadratic chirp (central plots) and with quadratic chirp removed (right plots).

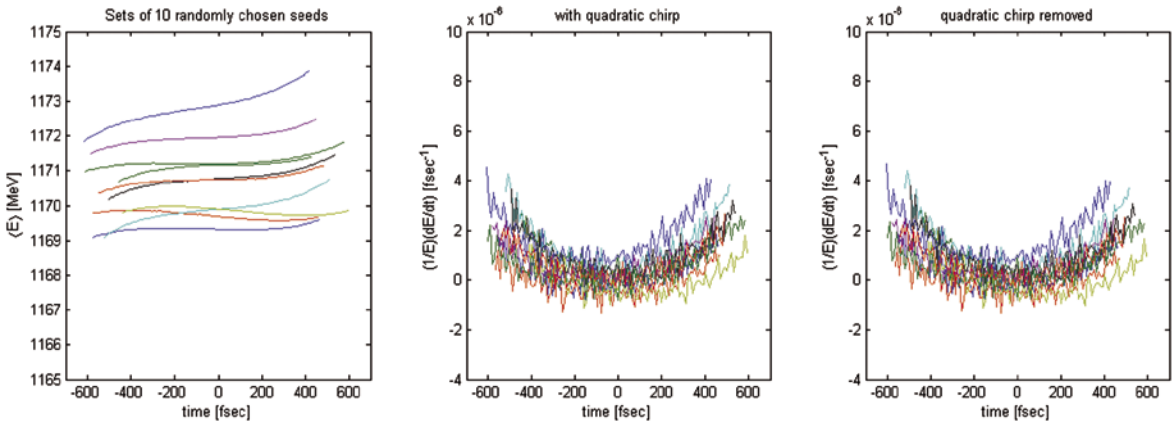

Figure 6.8.6:
Set of 10 randomly chosen seeds for long bunch case (b) (left plots) together with relative first derivative of the energy with respect to time inside the bunch with quadratic chirp (central plots) and with quadratic chirp removed (right plots).

6.8.4 Tracking Studies with Errors

A study was conducted to investigate the effect of a realistic acceleration environment that includes predicted errors in the photoinjector and in the linac. The simulation ("start-to-end") applied to the MLB configuration, follows the electron beam from the photo-cathode to the end of the acceleration.

Two codes were used for the tracking studies: GPT [42] for the photoinjector and Elegant for the linac. Eighty-four different particle distributions in the 6D phase space were randomly generated and converted into an Elegant input format. The particle distribution was tracked under the combined influences of the linac errors with rms values taken from Table 6.8.2. The 84 output particle distributions at the linac end were used as inputs for the FEL simulations. The statistical analysis on 84 different particle distributions obtained from Elegant gave jitters at the end of acceleration that are in good agreement with the 2-D LiTrack results:

$$\Delta I/I < 9.2\% \text{ rms}, \ \Delta E/E < 0.092\% \text{ and } \Delta t_f < 93\text{fs}$$

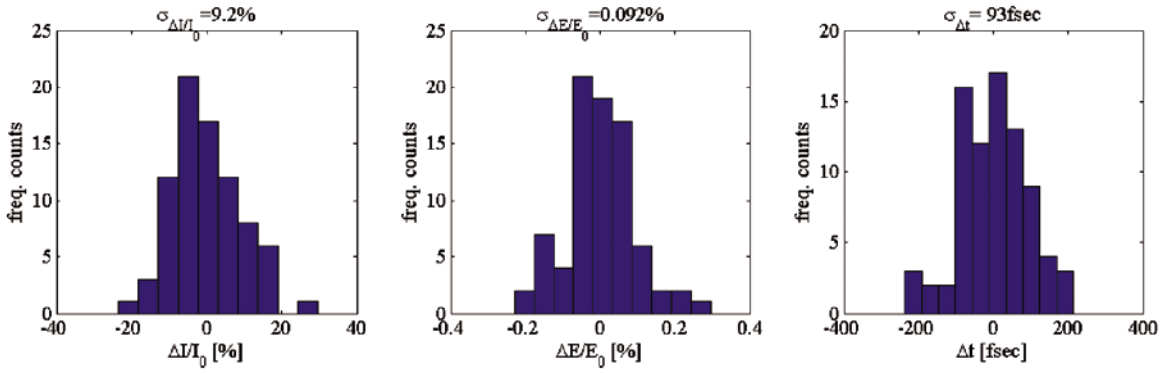

Figure 6.8.7:
Histograms for the MLB mode of the relative peak current $\Delta I/I_0$ (left), relative mean energy $\Delta E/E_0$ (center) and timing jitter Δt (right) obtained by means of Elegant simulations. I_0 is the nominal peak current and E0 is the nominal mean energy.

6.9 Collimation and Beam Dump

A 1.2 GeV electron beam loss can damage the permanent magnet modules of the insertion devices. To avoid this, beam collimation is essential for the protection of the undulator modules. In addition to collimators, beam stops and beam dump systems are needed for the machine and personnel protection systems. The specifications of these systems depend on the beam energy and power. These are estimated below.

6.9.1 Power Specifications

The following assumptions were made in the calculation of the electron beam power:

- maximum electron energy 1.5 GeV,
- maximum charge per pulse 1 nC,
- maximum repetition rate 50 Hz.

These assumptions are based on the projected operational specifications and possible future developments, like the energy upgrade to 1.5 GeV and the repetition rate of 50 Hz. The potential also exist for multi-bunch operation in a single pulse, with up to 100 bunches accelerated in a linac macropulses. This mode of operation is not part of the baseline design, but it cannot be excluded in a future development. A similar consideration applies to an upgrade of the linac repetition rate to 100 Hz.

Table 6.9.1: Average power and energy of the electron beam.

Mode	*Repetition rate [Hz]*	*Power [W]*	*Energy per pulse [J]*
Single pulse	50	75	1.5
100 macro pulses	50	7500	150
100 macro pulses	100	15000	150

The minimum possible geometric emittances are 0.5 nm in each plane, the energy spread is 0.1%, the average beta function is 10 m and the dispersion smaller than 0.001 m. Thus, under these conditions of maximum foreseeable electron beam density, the transverse beam dimension is 0.15 mm (rms value) and the beam transverse area, covering 4σ of the charge distribution, 0.4 mm^2.

The maximum peak power involved for a maximum peak current of 1.5 kA and a 0.6 ps long pulse is 1.5 TW. This peak power translated to peak energy density (with the previously found beam dimensions) is listed in Table 6.9.2.

Table 6.9.2: Peak energy density of the electron beam.

Single pulse density	0.42 kJ/cm^2/pulse
Bunch train density	42 kJ/cm^2/macro pulse

Only a small amount of the electron beam energy will be deposited to the chamber. In Figure 6.9.1 the electron energy loss for Steel and Al chambers is shown. For a 2 mm thick steel chamber the electrons will loose approximately 10% of their energy and 5% for Al. For the single pulse operation the maximum deposited energy will be 42 J/cm^2 and for the future macro-pulse mode it will be 4 kJ /cm^2. Note that metal damaging level starts at ~100 Joules/cm^2.

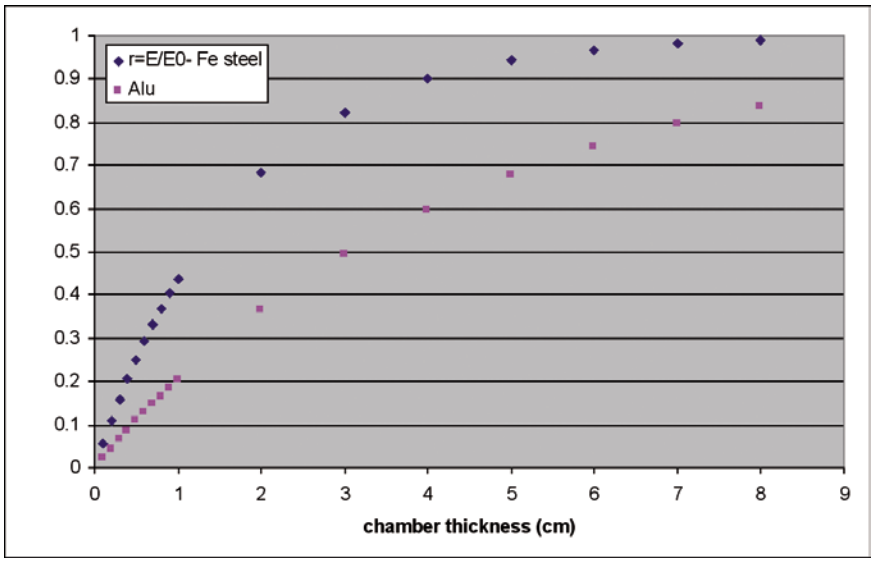

Figure 6.9.1:
Energy deposited vs. chamber thickness.

6.9.2 Beam Collimation

Beam collimation is essential in order to provide protection of the undulator modules from miss-steered beams. In addition, other undesirable effects like halo and dark current created in the gun and bunch compressors, wake field generated tails in the linac, mismatched and miss-steered beam, particles produced by Coulomb Scattering may damage and compromise the beam quality. The collimator section serves as transverse and longitudinal phase space filter. Particles outside this region are blocked and cannot be lost in the undulator modules. In the transverse plane this is achieved by a set of apertures limiting the transverse phase space volume. In the longitudinal plane similar pair of apertures at opposite dispersion regions limits the off-energy particles, dark current electrons and energy tails produced in the bunch compressors.

The collimator section is a key component of the FEL since it will be directly positioned in front of the undulators. Phase space parameters like emittance, length and energy spread can be measured there. The choice of the material and the shape and length of the collimators will be decided after a Monte-Carlo study on material and the secondary particle capturing efficiency. Both transverse and energy collimation are considered.

6.9.2.1 Betatron Collimation

In order to keep the collimation system as compact as possible a scheme with two single absorbers is adopted. This scheme has high efficiency with just two apertures working in parallel for both transverse dimensions. The two absorber blocks are separated by ~$\pi/2$ phase advance difference (see, Figure 6.2.8). Assuming a pipe radius of 8 mm a beam stay clear of 4 mm (26 σ of transverse beam dimensions) and betas at the undulators of the order of 10 m, the collimator acceptance is 0.8 μm. The aperture radius of the absorbers is about 3.5 mm for a 15 m distance between the absorber blocks.

6.9.2.2 Energy Collimation

Energy collimation will be achieved in a closed dispersive region using another pair of absorbers of about the same apertures as in the transverse case. The collimators will be installed at the point of maximum dispersion of the Spreader lattice (see, Figure 6.2.1).

6.9.3 Beam Dump

Beam stoppers, beam dump and the machine protection system are sketched here, together with some considerations on their implementation in the FERMI layout.

6.9.3.1 Linac Beam Stoppers and Beam Dumps

Four beam stoppers will be installed in the Linac for beam commissioning, tuning up and radiation safety. They will be situated after the gun, after each bunch compressor and at the end of the linac. Additionally at the end of the linac a beam dump will also be constructed for energy measurements. It consists of a DC electromagnet able to deflect the beam by 20 deg. followed by a simple short transfer line (in the already existing tunnel of the existing transfer line to the storage ring) at the end of which a small dump will be situated. A general view is shown in Figure 6.9.2.

6.9.3.2 Machine Protection System

Due to the low beam power of the baseline design with single pulse operation no fast beam abort system is needed. In case of problems (e.g. miss-steering, bad transmission, etc…) the linac gun will be inhibited. In a future upgrade a fast beam abort system might be needed.

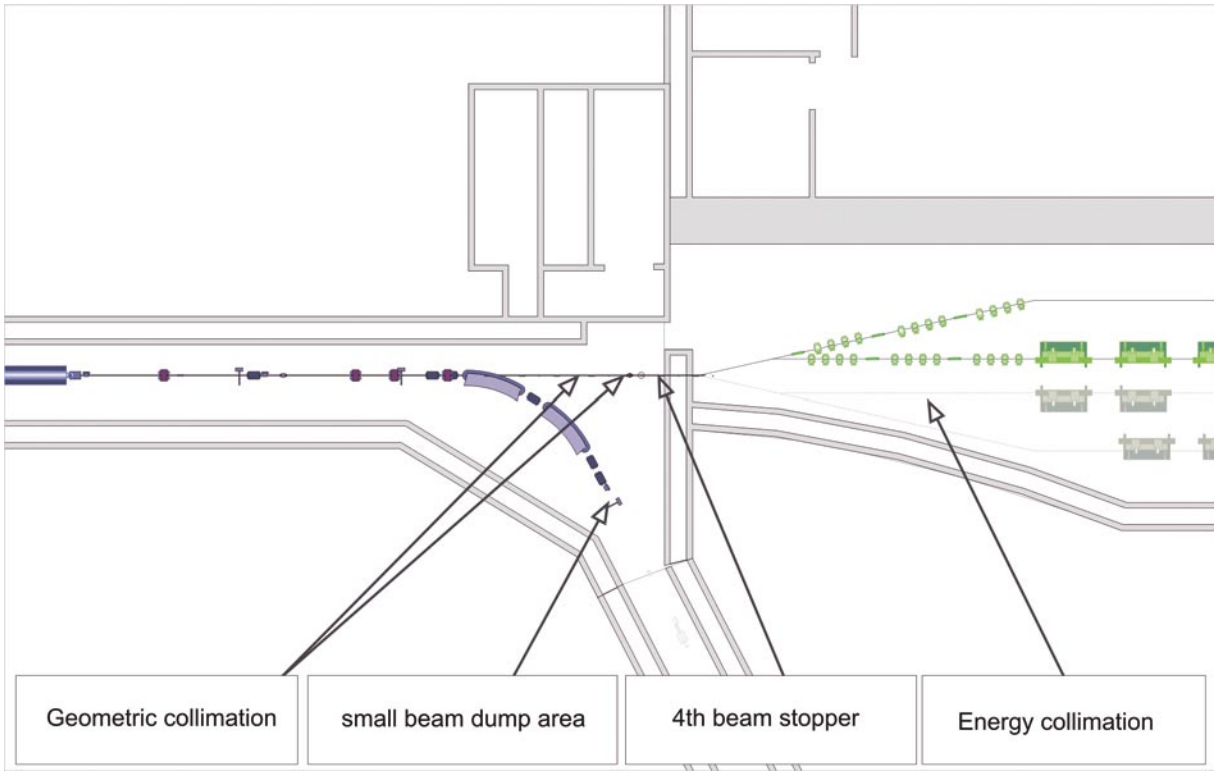

Figure 6.9.2:
End Linac and Spreader.

6.9.3.3 Main Beam Dump

A beam dump transfer line is foreseen in the beam lines at the end of each radiator. In order to be fail safe, and thus to completely eliminate the possibility of electrons propagating into the experimental stations, a permanent magnet will be used for the first deflection of 15 deg. The large angle is meant to keep the critical wavelength low so that the generated synchrotron radiation does not contaminate with the FEL light and keeps the thermal stress low. The layout is shown in Figure 6.9.3.

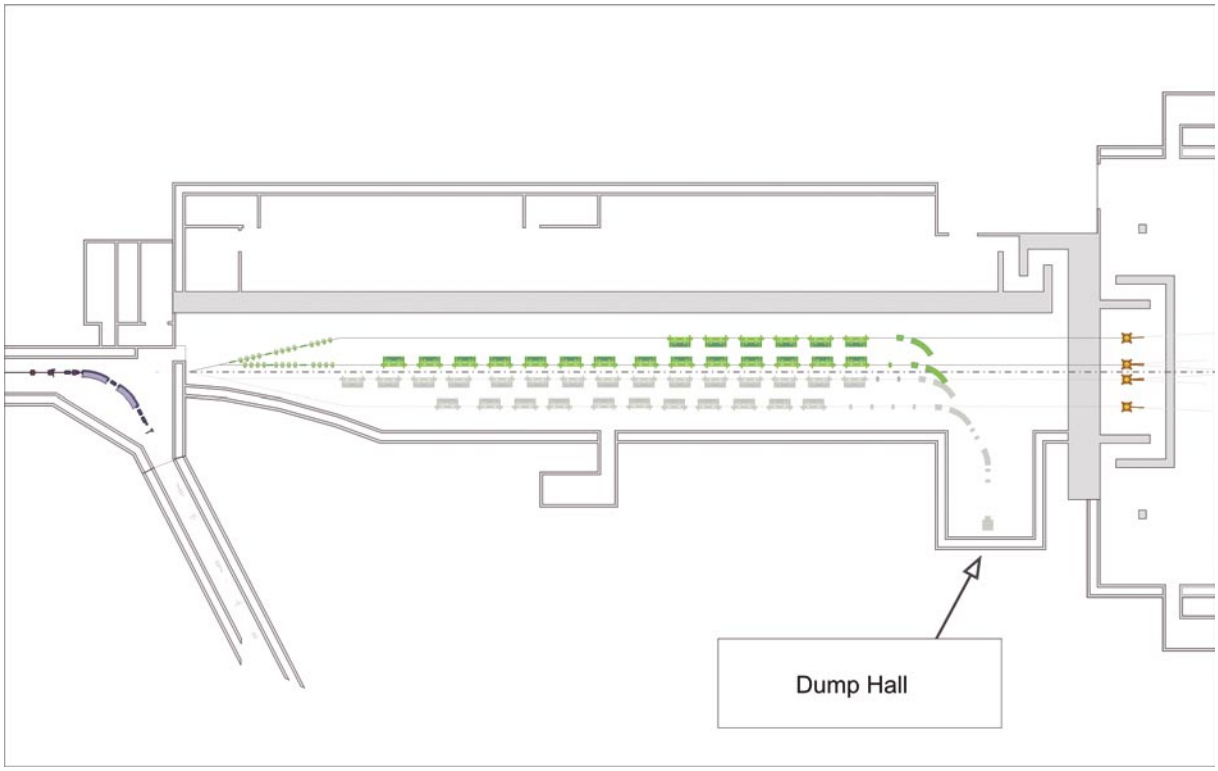

Figure 6.9.3:
A 20 m long TL leads to the dump hall.

The first bending set consists of one permanent and one electromagnetic dipole; it allows a 15+45 deg bending angle. The second bending set consists of an electromagnet of 30 deg bending angle (see, Figure 6.9.3). Using appropriate bypasses the FEL radiator lines can be connected to a unique chamber that eventually will transport the beams to the dump. Beam current toroids and loss monitors will be installed before and after the bends to control any losses (e.g. if beam has the wrong energy) and send a beam inhibiting signal to the photoinjector.

6.9.3.4 Dump Hall

An inadvertent loss of beam towards the ground will be intercepted by the underground rock, acting as dumper. Great care will be used to avoid that the dump be exposed to rain water, with possible contamination of underground waters with radioactive isotopes. A dedicated beam dump hall will be constructed to keep open the possibility of using the electron beam for diagnostics and experiments, and of using the light for micro-lithography and micro-mechanics, and for producing isotopes or neutrons for a future neutron source. This hall will be situated to the right of the FEL in the direction of the beam at the end of the radiator hall and will have an area of at least 50 m^2. Unlike the linac dump (which operates only during linac experiments) this dump will carry the burden of continuously dumping the electron beam.

6.9.3.5 Beam Dump Specifications

Although the single pulse mode involves low beam power, it is advisable to specify the dump with the maximum foreseen average and peak powers since, after years of operation, the dump becomes radioactive and it's preferable not to have to change the dump when the machine is upgraded.

It is foreseen to increase the transverse beam dimensions by at least a factor of 3 before the beam hits the dump. With this additional assumption, the main specifications of the FERMI dump are the following:

a. must absorb up to 4 kJoules/cm^2 / (macro) pulse;

b. must absorb an average beam power of up to 15 kW;

c. energy and radiation absorption efficiency > 99%;

d. natural production of isotopes must be minimized and isotopes must be short lived;

e. must be designed such as no maintenance will be required for a 10 year period for the absorbing core.

A standard graphite-aluminium beam dump that meets the above specifications [43] is described in Figure 6.9.4; electrons enter from left. More detailed calculations will define the details such as the cooling needed, the slow sweep system, etc.

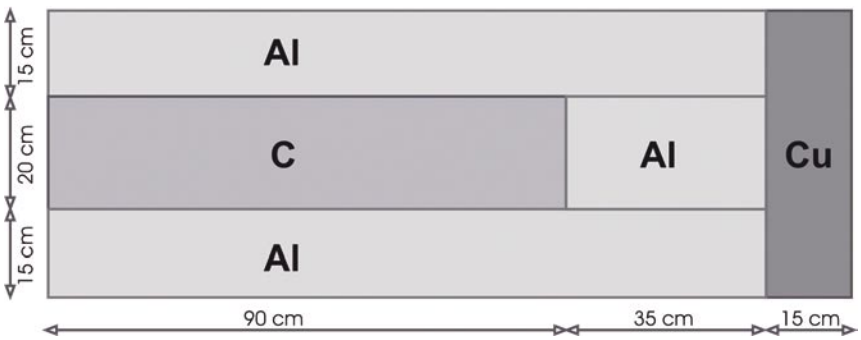

Figure 6.9.4: *Schematic of the graphite-aluminum beam dump.*

6.10 Instrumentation, Diagnostics and Feedback

This paragraph addresses some aspects of the electron beam diagnostics. A more detailed treatment of the instrumentation may be found in Chapter 9. The justification for long-term feedbacks and details about their functionality and interplay with the diagnostics specifications may be found in Chapter 10.

6.10.1 Laser Heater

In addition to being a tool for the control of the microbunching instability, the laser heater is also an excellent diagnostics instrument. To exploit this fact, a FODO channel placed after the laser heater will be used for electron beam size measurements at various phases of the betatron oscillations and also for emittance diagnostics. Removable screens will be employed in the locations indicated on the plot of Figure 6.2.2. The betatron phase advances between first and second screen, second and third screen and third and fourth screen are 24°, 79°, 24° in the horizontal plane, and 72°, 23°, 57° in the vertical plane.

6.10.2 Magnetic Chicanes

The energy dispersion is at its maximum in the middle of the chicane and, therefore, this is a convenient place for collimation and energy monitoring. Since the electron bunch typically has a significant energy chirp while it propagates through the chicanes, the collimator can be used to trim electrons in the head and tail of the electron bunch, thus helping reduce the peak current spikes at the bunch edges.

6.10.3 Spreader

The FODO channel after the L4 linac sections is designed to provide approximately 135° of betatron phase advance in both planes for emittance measurements using the removable screens marked as solid circles on the plot. Downstream of the FODO channel a possible convenient place for a deflecting cavity is indicated. This cavity will be used for slice emittance and energy spread measurements at high dispersion points in the spreader.

As mentioned above the collimation section is ideal for beam measurements: beam position monitors, current transformers, loss monitors and synchrotron radiation detections windows will be installed there. In order to tune the collimators, two Optical Transition Radiation (OTR) stations are needed, one for the transverse section and one in the dispersive section for energy spread tuning.

6.10.4 Feedbacks

The high sensitivity of a seeded machine to short-term fluctuations (jitters) and long-term variations (drifts) of the electron beam quality make the presence of feedbacks a fundamental specification of the machine design. This paragraph addresses some basic thoughts on this subject.

A longitudinal feedback is dedicated to the stability of the bunch length and of the average beam energy in correspondence of each magnetic chicane and of the Spreader, where appropriate diagnostics can be located. Together with a charge feedback in the Injector, it provides information about the long-term stability of the bunch current and of the FEL resonant energy.

A trajectory feedback maintains the trajectory stability in order to minimize the perturbations to the orbit and to the compensation of the "banana" shape induced by the beam break-up instability. This is especially true for the L4 linac section, which is the most sensitive part of the machine to this kind of instability. The undulator entrance is also another critical point for the trajectory stability; in fact, the beam based alignment technique requires tight tolerances on the stability of the beam launching just before the insertion devices.

6.11 Appendix A: Method of Vlasov's Equation

The direct numerical solution of the Vlasov equation represents a complementary approach to the more prevalent method of simulating beam dynamics by macroparticle tracking. In particular, a Vlasov solver offers the advantage of being immune from the statistical fluctuations stemming from using a limited number of macroparticles, which may interfere with a correct interpretation of the results when studying the microbunching instability. Small scale structures are more easily resolved and the unfolding of instabilities more accurately characterized. Moreover, in contrast to semi-analytical studies based on the linearized Vlasov equation, numerical solutions of the full equation can be used to investigate saturation effects, which may be important.

It should be pointed out that the Vlasov solver should not be expected to substitute the macroparticle simulations since at this time only a 2D phase-space solver is available. Moreover, the physics that can be currently investigated with the existing solver is limited in practice to short-scale effects of the collective forces (microbunching).

The existing code allows one to include models of impedance describing space charge, coherent synchrotron radiation (CSR), and RF structure wake fields. CSR is evaluated in free space with the assumption that the bunch follows a trajectory with uniform radius of curvature. This excludes transition effects through the entrance and exit of bending magnets. In the study discussed here the RF structure wake fields were not included.

It was argued that it is possible in 2D to account for the particles smearing due to the transverse emittance in an approximate but meaningful way by introducing an effective low-pass filter in the evaluation of the collective force. Some confidence in the validity of the above model of emittance-induced smearing can be obtained from comparison with predictions from linear theory [24] in the regime where linear theory applies. Incidentally, such comparisons have also been successfully used to provide general validation of the coding.

Figure 6.11.1 shows the gain curves for a beam that travels through approximately 36 m of transport line (including L1) before entering the bunch compressor. The gain curves are evaluated at the exit of BC1. In this case space charge effects are significant and are included in the calculation.

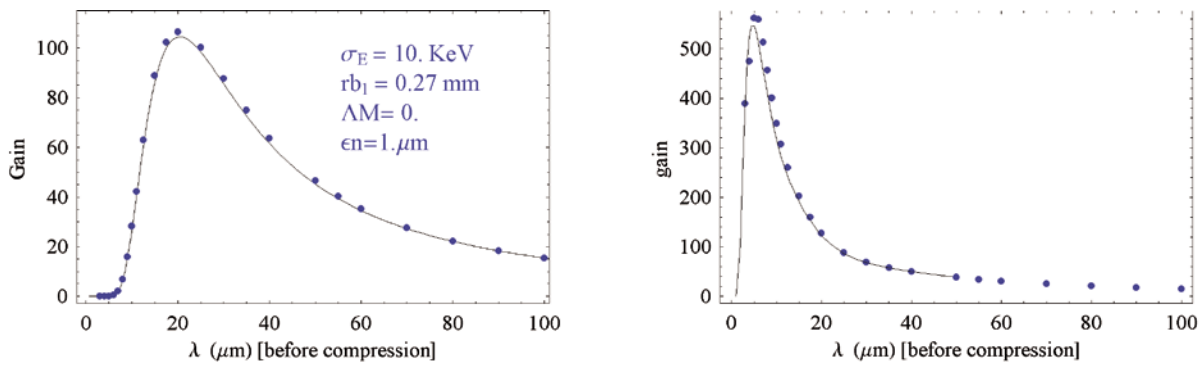

Figure 6.11.1:
Gain curves through for L1+BC1 in the presence of CSR and space charge (with space charge excluded in BC1) as determined by linear theory (solid line) and from the numerical solutions of the Vlasov equation (blue dots). σ_E*=10 KeV; smearing effect of transverse emittance is included in the left but not in the right picture.*

The gain plotted is the ratio between the amplitude of a sinusoidal charge-density modulation for a given frequency at the exit and entry of the bunch compressor. The amplitude is understood to be expressed in units of the peak current (which is different at entrance and exit because of compression). The beam is a flat-top with Gaussian energy spread.

In the Vlasov code the local value of the transverse rms size is used so that the "effective" beam radius appearing in the impedance model is taken as [8] $r_b^2 = [1.3\ (\sigma_\xi^2 + \sigma_\psi^2)]$. For the linear theory calculation a constant in z transverse size is assumed. The parameter r_b for the linear theory was adjusted to fit the gain curve against the Vlasov solver calculation. The same value, r_b =0.27 mm was then used to produce both pictures in Figure 6.11.1. The application of the Vlasov solver was then extended to include the L2 and L3 and the second bunch compressor BC2. The goal was to study the effect of shot noise in the development of the microbunching instability and determine its impact on the uncorrelated rms energy spread on the beam past BC2. Result is shown in Figure 6.11.2.

The initial beam density is a flat-top in charge density and Gaussian in the uncorrelated energy spread. The shot noise was modeled by perturbing the initial, smooth density function in phase space with random noise. The calculation indicates that most of the energy modulation induced by space charge (the dominant collective effect) takes place between BC1 and BC2. By the time the beam reaches BC2 these fluctuations are sufficiently large to cause the instability to reach saturation, as indicated by the two bottom plots. Notice that in this calculation SC and CSR are the only collective effects present.

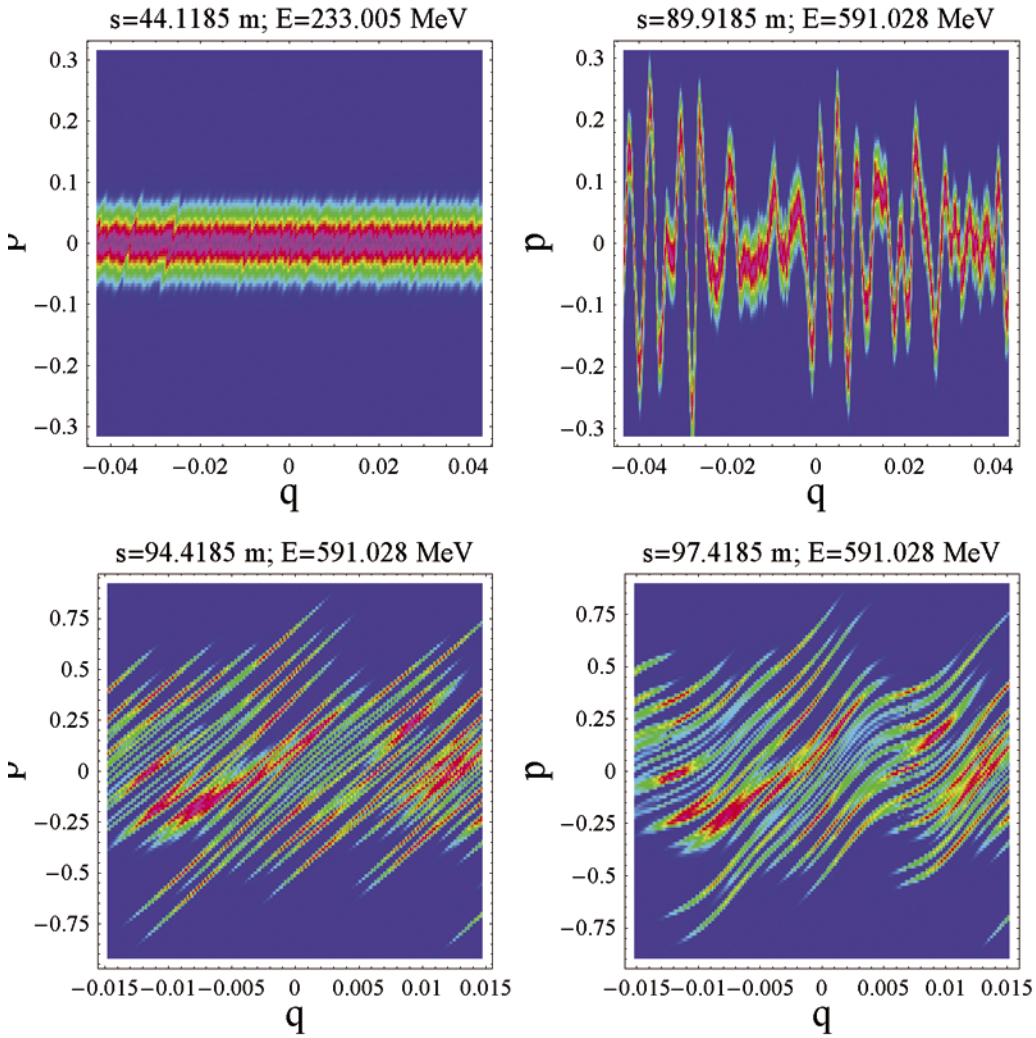

Figure 6.11.2:
Longitudinal phase space at selected locations starting from a noisy flat top bunch with Gaussian rms energy spread; s=0 is at the start of the laser-heater section. The top left pictures is at the exit of BC1; top right picture is at the entrance of BC2 and the remaining two after the BC2 3rd and 4th dipole (q is the z-coordinate in units of 1 mm, p is the uncorrelated energy in MeV).

6.12 Appendix B: 6D Parallel Tracking Code IMPACT

IMPACT is a suite of parallel particle-in-cell codes designed for modeling high intensity, high brightness beams in RF proton linacs, electron linacs and photoinjectors. It consists of two parallel particle-in-cell tracking codes (one is longitudinal position-dependent and one is time-dependent), an RF linac lattice design code, an envelope matching and analysis code, and a number of pre- and post-processing codes. The present version of IMPACT can treat intense beams propagating through drifts, magnetic quadrupoles, magnetic soleniods, magnetic dipole, and RF cavities, using map integrator and nonlinear Lorenz integrator. Recent additions include new capabilities for modeling short range longitudinal and transverse wakefields as well as 1D CSR wakes.

Both parallel particle tracking codes of the IMPACT suite assume a quasi-static model of the beam and calculate space-charge effect self-consistently at each time step together with the external acceleration and focusing fields. Typical IMPACT simulations at NERSC are run with a few millions to a few tens million particles, though smaller and larger runs are possible.

6.13 References

[1] K. Bane, Proc. of EPAC 2004, Lucerne, Switzerland.

[2] P. Tenenbaum, SLAC-TN-04-038 (2004).

[3] Y. Derbenev et al., TESLA-FEL=95-05 (1995).

[4] S. Di Mitri, proc. of FEL 2006, Berlin, Germany.

[5] E.L. Saldin, E.A. Schneidmiller, M. Yurkov, TESLA-FEL-2003-02 (2003).

[6] P. Emma, Proc. of EPAC 2004, Lucerne, Switzerland.

[7] S. Di Mitri, ST/F-TN-06/09 (June 2006).

[8] M. Cornacchia et al. ST/F-TN-06/15 (July 2006).

[9] D. Douglas, JLAB-TN-98-012 (1998).

[10] P. Craievich et al., ST/F-TN-05/01 (March 2005).

[11] G. D'Auria, A. Ratti, ST/F-TN-05/07 (March 2005).

[12] G. D'Auria et al., ST/F-TN-06/10

[13] A. Zholents et al., submitted to PRST-AB, November 2006.

[14] W. Fawley, G. Penn, ST/F-TN-06/07 (2006).

[15] K. Bane et al., SLACPUB-7862 (1998).

[16] K. Bane., SLAC-PUB-9663 (2003).

[17] P. Craievich, T. Weiland, I. Zagorodnov, NIM A, 558, 58 (2006).

[18] K. Bane, SLAC-PUB-11829 (2006).

[19] K. Bane et al., Proc. Of ICAPC, Monterey, SLAC, CA, p.137 (1998)

[20] K. Bane, A. Mosnier, A. Novokhatski, K. Yokoya, in Proc. ICAPC, Monterey, CA (1998) and SLAC-R-580, p. 137 (1998).

[21] 4GLS Conceptual Design Report, http://www.4gls.ac.uk/documents.htm, April (2006).

[22] D. H Dowell, T. D. Hayward, A. M. Vetter, Proc. of PAC 1995, New York.

[23] K. Flotmann, T. Limberg, P. Piot, TESLA-FEL-2001-06.

[24] Y. Derbenev, V. Shiltsev, SLAC-PUB-7181 (1996).

[25] J.J. Bisognano et al., PAC 1997, p.1644.

[26] A. Zholents, ST/F-TN-05/15

[27] G.Dattoli, A.Renieri. Laser handbook, Vol.4 (1985).

[28] Z. Huang et al., Phys. Rev. ST-AB, 7, 074401 (2004).

[29] E. Saldin et al. , NIM A 483 (2002).

[30] M. Borland, APS LS-287 (2000).

[31] P. Emma, TESLA 95-17 (July 1995).

[32] T.O. Raubebenheimer, P. Emma, S. Kheifets, Proc. of PAC 1993.

[33] H. Wiedemann, Particle Accelerator Physics, Vol.I, pgg. 225 – 240, ed. Springer (2003).

[34] P. Craievich, S. Di Mitri, Proc. of EPAC 2006, Edinburgh, Scotland, UK.

[35] J. Delayen, PRST-AB, **6**, 084402 (2003).

[36] J. Delayen, PRST-AB, **7**, 074402 (2004).

[37] P. Craievich and S. Di Mitri, Proc. of the FEL 2005 Conf., SLAC, CA (June 2005).

[38] G. De Ninno, B. Fawley and G. Penn, ST/F-TN-06/01 (CBP Tech Note-356).

[39] $B_y=b_0+b_1(x/R)+b_2(x/R)^2+b_3(x/R)^3+O(x^4)$ with multipolar index n=0,1,2,3 etc… for dipole, quadrupole, sextupole component, etc…

[40] K. Bane, P. Emma, Proc. of PAC 2005, Knoxville. Tennessee.

[41] M. Budiman, Matlab utility: Latin Hypercube Sampling, budiman@acss.usyd.edu.au, 2004.

[42] S. B. van der Geer et al., http://www.pulsar.nl/gpt.

[43] TESLA–FEL 99-06, DESY (December 1999).

[44] A. Zholents et al., LBNL-62345 (January 2007).

[45] F. Parmigiani (Sincrotrone Trieste), private communication.

Table of Contents

6 Accelerator 141
6.1 Introduction and Overview 142
6.1.1 Overview of Design Specifications 143
6.2 Accelerator Lattice and Components 146
6.2.1 Laser Heater 146
6.2.2 First Bunch Compressor 147
6.2.3 Second Bunch Compressor 148
6.2.4 Linac End Section and Spreader 148
6.3 Tracking Study 154
6.3.1 Medium Length Bunch Mode 154
6.3.2 Long Bunch Mode 156
6.4 The Linear Accelerator 157
6.4.1 Existing Linac and Future Upgrade 158
6.4.2 Accelerating Structures 158
6.4.3 HV Modulators 161
6.4.4 LLRF System 164
6.4.5 Linac Stability 167
6.5 The Geometric Wake Functions of the Accelerating Structures 170
6.5.1 Longitudinal Wake Potentials 171
6.5.2 Transverse Wake Potentials 172
6.6 Compression and Longitudinal Dynamics 173
6.6.1 Magnetic Compression 173
6.6.2 Coherent Synchrotron Radiation 174
6.6.3 Reverse Tracking 175
6.6.4 Microbunching Instability 175
6.7 Transverse Dynamics 183
6.7.1 Chromatic Aberrations 183
6.7.2 Geometric Aberrations 184
6.7.3 Quantum Fluctuations (ISR) 184
6.7.4 Trajectory Distortions 185
6.7.5 The Beam Break-Up Instability 188
6.7.6 Transverse Acceptance and Error Tolerances 191
6.8 Beam Jitters Sensitivities and Effects of Errors 200
6.8.1 Longitudinal Dynamics 200
6.8.2 Global Jitter Study 205
6.8.3 Slice Jitter Analysis 207
6.8.4 Tracking Studies with Errors 209
6.9 Collimation and Beam Dump 210
6.9.1 Power Specifications 210
6.9.2 Beam Collimation 212
6.9.3 Beam Dump 212

6.10 Instrumentation, Diagnostics and Feedback 216
6.10.1 Laser Heater 216
6.10.2 Magnetic Chicanes 216
6.10.3 Spreader 216
6.10.4 Feedbacks 216
6.11 Appendix A: Method of Vlasov's Equation 217
6.12 Appendix B: 6D Parallel Tracking Code IMPACT 220
6.13 References 221